Physics-Based Statistical Learning in Thermoacoustics

Francesco Garita

Department of Engineering
University of Cambridge

This dissertation is submitted for the degree of
Doctor of Philosophy

Peterhouse College April 2021

To my grandparents,
wherever they are . . .

Declaration

I hereby declare that except where specific reference is made to the work of others, the contents of this dissertation are original and have not been submitted in whole or in part for consideration for any other degree or qualification in this, or any other university. This dissertation is my own work and contains nothing which is the outcome of work done in collaboration with others, except as specified in the text and Acknowledgements. This dissertation contains fewer than 65,000 words including appendices, bibliography, footnotes, tables and equations and has fewer than 150 figures.

Francesco Garita
April 2021

Acknowledgements

To begin with, I would like to thank my supervisor, Prof. Matthew P. Juniper, for the immeasurable support he has given me on a daily basis in the past three years. His guidance has been essential for me, and without his encouraging and stimulating words I would have likely not reached this stage today. The qualities I appreciate most about him are certainly the physical intuition, the perseverance in demonstrating his research ideas, and the willingness to follow and guide his students with constancy and dedication. I have always felt proud to be part of his research team. To him I wish the best.

I would like to extend my gratitude to my colleague and friend, Ushnish Sengupta, who has devoted a lot of his time to me and my project. I will always thank him for transferring some of his expertise in statistics and machine learning to me. All the very many discussions we have had are simply invaluable and have contributed significantly to my personal growth.

I would like to acknowledge my former colleague and friend, Dr. Hans Yu, for the availability he has always shown to me and to every other member of the research team. It was a real pleasure to meet him, and I feel honoured to be his friend.

I would like to thank my research group and all the awesome people I have had the opportunity to come across in the Hopkinson Lab in the past three years, some of whom have also become good friends of mine. In no particular order: Alberto Racca, Max Croci, Filip Gokstorp, Stefano Falco, Alexandros Kontogiannis, José Aguilar, Petr Kungurtsev, Jack Brewster, Ubaid Qadri, Matthew Yoko, Peter Benie, Pau Farres, Antoine Koen, Roberto Ciardiello, Francesca De Domenico, Joselino Rodrigues, Jenna Foale, Jessie Smith, Dante McGrath, Santi Sukma, Francesco Ciriello, Luca Magri, and Andrea Giusti.

In the Engineering Department, I am also very grateful to the workshop technicians, Roy Slater, Mark Garner, Ken Griggs, Rob Leroy, and John Harvey, who have been extremely helpful whenever there was something new to manufacture for my experiments. A special thanks also to John Hazlewood for allowing me to use the anechoic room in the Acoustics Lab for a whole week during my second year, and to Mark Huntsman, for manufacturing a great phase-shift amplifier for my experiments in a very short time. A final acknowledgement goes to the Division A's administrators, Wendy Raymond and Kate Graham, for the continued support and for arranging tea breaks on a weekly basis for the entire Hopkinson Lab community.

Life in Cambridge has been simply amazing. My time in this lovely city would not have been as great without the Peterhouse College community. I would like to thank particularly two good friends of mine, Alexander Abecina and Kan Gunawardena, for all the fun moments spent together. I truly hope our paths will cross again in the future.

I would like to thank also my funding body, the European Commission, for the generous Marie-Curie grant assigned to me in order to carry out this PhD project. Along with the European Commission, I need to acknowledge all the members of the MAGISTER consortium and particularly the Project Administators, Jorien van Loon and Bridgette Connell, for the great coordination as well as for always being available to answer my queries.

Last but not least, I would like to thank my family, including my aunt, Angela Rosa, and my cousin, Lucio. I am particularly grateful to my parents, Michele and Maria Ida, for the immense support they have always given me, especially in bad moments. I would certainly not be writing this thesis right now if I had not received their support.

Abstract

Thermoacoustic oscillations arise because of the interaction between acoustic waves inside a duct or a combustion chamber, and heat release rate oscillations at the flame or heater location. When certain conditions are met, these oscillations may grow significantly in time and cause severe problems, particularly in gas turbines used for propulsion, i.e. in systems characterized by high powers. Thermoacoustic oscillations are extremely sensitive to small changes in the system geometry, parameters, and boundary conditions. For this reason, it is challenging to build quantitatively-accurate models that are general.

In this thesis, we propose to generate physics-based qualitatively-accurate reduced-order models, which are general, and then tune their parameters so that they become quantitatively accurate to describe the system under investigation. To do this, we use statistical learning techniques in combination with an experimental dataset consisting of $\mathscr{O}(10^6)$ datapoints. The dataset is obtained from more than 210 hours of automated experiments on an electrically-heated vertical Rijke tube. We use the ensemble Kalman filter to infer the parameters of a conjugate heat transfer model driven by natural convection. Then we use the Markov Chain Monte Carlo (MCMC) method to infer the parameters of a linear acoustic model that is driven by the thermoacoustic mechanism and damped by visco-thermal dissipation and by radiation from the ends of the tube. We perform experiments only on the fully-assembled system, rather than on its individual components. We learn model parameters sequentially by using posterior values and uncertainties from early experiments as prior values and uncertainties for later experiments. With access to parameter uncertainties available with the MCMC, we quantitatively compare the marginal likelihood of the data for four tuned heat release rate models, thus finding the best performing model. Because it is physics-based, we find that the best model is quantitatively accurate, with known error bounds, significantly beyond the range of the training set. This process successfully combines physics-based modelling with data-driven methods in order to turn a qualitatively-accurate model into a quantitatively-accurate model, which is a significant challenge in thermoacoustics.

Preface

Peer-reviewed publications

- F. Garita, U. Sengupta, and M. P. Juniper. Statistical Learning of Acoustic and Thermoacoustic Model Parameters of a Rijke Tube Using Bayesian Inference. *Journal of Sound and Vibration*, 2021. [Accepted for publication]

- [1] F. Garita, H. Yu, and M. P. Juniper. Assimilation of Experimental Data to Create a Quantitatively Accurate Reduced-Order Thermoacoustic Model. *Journal of Engineering for Gas Turbines and Power*, 143(2):021008, 2021. https://doi.org/10.1115/1.4048569

- F. Garita, H. Yu, and M. P. Juniper. Assimilation of Experimental Data to Create a Quantitatively-Accurate Reduced Order Thermoacoustic Model. *Proceedings of the ASME Turbo Expo 2020: Turbomachinery Technical Conference and Exposition. Volume 4A: Combustion, Fuels, and Emissions*. https://doi.org/10.1115/GT2020-14929

Conference presentations

- F. Garita, H. Yu, and M. P. Juniper. A Bayesian Approach for Predicting Thermoacoustic Oscillations in an Electrically-Heated Rijke Tube. *Frontiers of Uncertainty Quantification*. Pisa (Italy), September 2019.

- F. Garita, H. Yu, L. Magri, and M. P. Juniper. A Bayesian Approach for Predicting Thermoacoustic Oscillations in an Electrically-Heated Rijke Tube. *American Physical Society: Division of Fluid Dynamics*, Atlanta (US), November 2018.

- H. Yu, T. Jaravel, M. Ihme, F. Garita, M. P. Juniper, L. Magri. Data assimilation and parameter estimation of thermoacoustic instabilities in a ducted premixed flame.

---

[1] This paper was first accepted to the Proceedings of the ASME Turbo Expo 2020 and then selected for publication on the Journal of Engineering for Gas Turbines and Power. Thus, the two publications are identical, despite having a different DOI.

American Physical Society: Division of Fluid Dynamics, Atlanta (US), November 2018.

- F. Garita, H. Yu, L. Magri, and M. P. Juniper. Predicting and Controlling Thermoacoustic Oscillations in a Rijke Tube through Data Assimilation: an Ensemble Kalman Filter Approach. *UK Fluids Conference*, Manchester (UK), September 2018.

Table of contents

List of figures **xv**

List of tables **xvii**

List of algorithms **xix**

Nomenclature **xxi**

1 Introduction **1**

1.1 Thermoacoustics 1

1.2 Statistical learning 6

1.3 Ensemble Kalman filter 10

1.4 Markov Chain Monte Carlo 14

2 Experimental setup **19**

2.1 Apparatus 19

2.2 Data acquisition 20

2.3 Data analysis and results 23

3 Slow time-scale modeling **31**

3.1 Model 31

3.1.1 Summary of the non-dimensional model 34

3.2 Numerical implementation 35

3.3 Data Assimilation 37

3.4 Results 38

4 Fast time-scale modelling without the thermoacoustic mechanism **43**

4.1 Modelling the empty tube 43

4.2 Modelling the thermo-viscous drag from the switched-off heater 50

4.3 Modelling the visco-thermal drag from the thermocouples 58
4.4 Multi-microphone method 61

5 Thermoacoustic modelling 71
5.1 Models description 71
5.2 Qualitative comparison 74
5.3 Quantitative comparison 78

6 Conclusions 83
6.1 Summary 83
6.2 Future work 84

References 87

Appendix A Complex frequency and pressures from experiments (Matlab script) 95

Appendix B Slow time-scale model (Matlab script) 97

Appendix C Performance of model 2 99

Appendix D Performance of model 4 103

List of figures

1.1 Qualitative schematic of the ensemble Kalman filter 13
1.2 Qualitative schematic of the MCMC Metropolis algorithm 16

2.1 Apparatus sketch 21
2.2 Electric heater 22
2.3 Gas temperature measurements 24
2.4 Acoustic ping and decay 27
2.5 Experimental complex frequencies with the heater off 28
2.6 Experimental complex frequencies with the heater on 29

3.1 Tube element sketch 32
3.2 Probability density function of the heat source 37
3.3 Slow time-scale model parameters 40
3.4 Comparison of gas temperature measurements and model predictions 41
3.5 Inlet bulk speed 42

4.1 Sketch of a network model 44
4.2 Feedback sensitivities for the Rijke tube 52
4.3 Cold flow experiments and model predictions using nonlinear regression . . 53
4.4 Evolution of the Markov Chains of the cold flow parameters 57
4.5 Cold flow experiments and model predictions using the MCMC 59
4.6 Posterior distribution in the parameter space for the cold flow 64
4.7 Acoustically-excited tube sketch for the use of the multi-microphone method 65
4.8 Relative calibration coefficients 68

5.1 Comparison between experimental data and predictions of model 1 77
5.2 Comparison between experimental data and predictions of model 3 80
5.3 Two-dimensional parameter distributions of model 3 82

C.1 Comparison between experimental data and predictions of model 2 101

D.1 Comparison between experimental data and predictions of model 4 105

List of tables

2.1 Microphone specifications 25

3.1 Temperature measurements used for data assimilation 42

4.1 Microphone relative calibration coefficients 69

5.1 Average (marginal) log-likelihood per datapoint and RMSE 82

List of algorithms

4.1 Solution to the eigenvalue problem using Jacobi's formula 49
4.2 Forward uncertainty propagation to state s using standard Monte Carlo . . . 58

5.1 Computation of the average log-likelihood per datapoint 81

Nomenclature

Roman Symbols

A	Cross-sectional area
c	Specific heat capacity (at constant pressure if c_{p}) / Speed of sound
cc	Calibration coefficient as provided by the microphone manufacturer
D	Diameter of the tube
d	Observation / Diameter (e.g. of the filament)
det	Determinant of a matrix
eps	Machine epsilon (or machine precision)
F	Laplace transform of the forward travelling wave / Force
f	Frequency / Forward travelling wave
G	Laplace transform of the backward travelling wave
g	Gravitational acceleration constant / Backward travelling wave
i	Imaginary unit ($i^2 = -1$)
Im	Imaginary part
k	Pressure loss coefficient
L	Length of the tube
$\mathscr{L}$	Log-likelihood function
$\mathscr{M}$	Model

n	Interaction index
$\mathscr{N}$	Normal (or Gaussian) distribution
Nu	Nusselt number
$\mathscr{O}$	Order of magnitude
p	Pressure / Probability / Probability density function
Pr	Prandtl number
$\dot{q}$ / $\dot{Q}$	Thermal power (if it is per unit volume it will be specified)
$\tilde{\dot{Q}}$	Thermal power per unit length
r	Thickness of the tube
$\mathscr{R}$	Proposal distribution
ref	Reference
R	Reflection coefficient
Re	Reynolds number / Real part
s	Complex frequency / Entropy
T	Temperature
t	Time
$\mathscr{T}$	Transition distribution
tr	Trace of a matrix
U	Bulk velocity (at a given tube section if with subscript)
u	Velocity
$\mathscr{U}$	Uniform distribution
x	Axial coordinate
z	Relative calibration coefficient

Greek Symbols

γ	Gas heat capacity ratio ($\gamma = 1.4$ for air)
λ	Thermal conductivity
μ	Dynamic viscosity
ν	Kinematic viscosity (or momentum diffisuvity)
π_{i}	Internal perimeter of the tube ($\pi_{\mathrm{i}} = \pi D$)
π_{o}	External perimeter of the tube ($\pi_{\mathrm{o}} = \pi(D+2r)$)
ψ	Model state or parameter
ρ	Density
σ	Standard deviation
$\boldsymbol{\sigma}$	Covariance matrix
τ	Time delay
Θ^{*}	Non-dimensional temperature ($\Theta^{*} = (T-T_{1})/T_{1}$)

Superscripts

$(\cdot)^{\mathrm{a}}$	Analyzed state
$(\cdot)^{\mathrm{e}}$	Ensemble
$(\cdot)^{\mathrm{f}}$	Forecast state
$(\cdot)^{t}$	Timestep t
$(\cdot)^{\mathrm{t}}$	True state
$(\cdot)'$	First-order perturbed quantity
$(\cdot)^{*}$	Non-dimensional quantity (non-dimensionalized with $\{L,\ g,\ T_{1}\}$)

Subscripts

$(\cdot)_{1}$	Inlet
$(\cdot)_{2}$	Outlet
$(\cdot)_{\mathrm{a}}$	Ambient

$(\cdot)_\mathrm{bl}$	Boundary layer
$(\cdot)_\mathrm{d}$	Downstream
$(\cdot)_\mathrm{DR}$	Decay rate
$(\cdot)_\mathrm{eq}$	Equivalent
$(\cdot)_\mathrm{exp}$	Experimental
$(\cdot)_\mathrm{f}$	Frequency / Filament
$(\cdot)_\mathrm{g}$	Gas
$(\cdot)_\mathrm{h}$	Heater
$(\cdot)_i$	Generic network element i
$(\cdot)_\mathrm{i}$	Inner / Inviscid
$(\cdot)_\mathrm{lik}$	Likelihood
$(\cdot)_\mathrm{m}$	Microphone
$(\cdot)_\mathrm{o}$	Outer
$(\cdot)_\mathrm{r}$	Rod
$(\cdot)_\mathrm{s}$	Solid
$(\cdot)_\mathrm{th}$	Thermal
$(\cdot)_\mathrm{t}$	Thermocouple
$(\cdot)_\mathrm{tot}$	Total
$(\cdot)_\mathrm{u}$	Upstream
$(\cdot)_\mathrm{vis}$	Viscous
$(\cdot)_\mathrm{w}$	Wire

Other Symbols

$\oint_{\Delta t}$	Cyclic integral over a time period Δt
$\overline{(\cdot)}$	Ensemble-average / Time- and space-average

$\hat{(\cdot)}$	Laplace-transformed quantity
$\oint_V$	Volume integral

Acronyms / Abbreviations

CFD	Computational Fluid Dynamics
DNS	Direct Numerical Simulation
EnKF	Ensemble Kalman Filter
FDF	Flame Describing Function
FTF	Flame Transfer Function
KF	Kalman Filter
LES	Large Eddy Simulation
MCMC	Markov Chain Monte Carlo
MMM	Multi-Microphone Method
NOx	Nitrogen Oxides
PDE	Partial Differential Equation
PID	Proportional Integral Derivative
RANS	Reynolds-Averaged Navier Stokes
RMSE	Root Mean Square Error
TMM	Two-Microphone Method

Chapter 1

Introduction

In this chapter, we first provide the reader with an overview of ~~what~~ the fundamental problems in thermoacoustics ~~are,~~ and then we build up the theory needed to tackle these problems. In particular, in Sec. 1.1 we provide the motivation for our work, illustrate the state-of-the-art techniques used in the field of thermoacoustics, and describe the system under investigation. In Sec. 1.2 we framework the methodology used throughout this thesis using concepts of probability theory and statistical inference, and cite several works that have been recently published in this research area. In Secs. 1.3 and 1.4 we ~~instead~~ thoroughly describe the statistical learning techniques used in the later chapters. ~~These techniques represent the backbone of this work.~~

1.1 Thermoacoustics

Thermoacoustics is a research area that lies at the boundary between combustion, fluid dynamics, and acoustics. In simple terms, thermoacoustic instabilities occur when heat release rate unsteadiness (for example, but not necessarily, caused by a combustion process) interacts in a constructive way with the acoustic field, amplifying noise. In aircaft and rocket engines, thermoacoustic oscillations grow when heat release rate fluctuations at the flame become sufficiently in phase with acoustic pressure waves inside the combustion chamber. These oscillations can become strong enough to damage the engine through increased heat transfer to the walls, mechanical vibration, and even structural failure [1–4]. They are particularly concerning to aircraft engine manufacturers, who would like to convert engines to lean premixed combustion in order to reduce NOx emissions, but are challenged by the fact that this increases their susceptibility to thermoacoustic oscillations [3]. Engines operating at these conditions are indeed more susceptible to combustion instabilities because of their flames' very high sensitivity to equivalence ratio perturbations, system geometry, boundary conditions, and other factors, as reported by Candel [5, 6] and Juniper and Sujith [7]. This provides numerous research groups around the world with a strong motivation to study such phenomena, which are still far from being completely understood.

The first scientific realization of the existence of a thermoacoustic instability dates back to 1802, when Higgins [8] observed generation of sound upon placing a hydrogen flame into tubes of different materials. Sound was generated at a frequency close to the natural frequency of the singing tube and only when the system parameters were in a particular range. A qualitative explanation of this phenomenon arrived more than seventy years later, when Lord Rayleigh published in 1878 his famous paper [9] in which he stated that

> *If heat be periodically communicated to, and abstracted from, a mass of air vibrating (for example) in a cylinder bounded by a piston, the effect produced will depend upon the phase of the vibration at which the transfer of heat takes place. If heat be given to the air at the moment of greatest condensation, or taken from it at the moment of greatest rarefaction, the vibration is encouraged. On the other hand, if heat be given at the moment of greatest rarefaction, or abstracted at the moment of greatest condensation, the vibration is discouraged.*

Rayleigh [9] was the first person to realize that sound is encouraged when providing heat to a gas during moments of high pressure, and when taking out heat from a gas during moments of low pressure. Indeed, the driving mechanism of a thermoacoustic instability is similar to the one that drives a piston engine [7]. In a piston engine, a gas is first compressed by a piston and then is burned in a combustion chamber. The accumulated energy is then released by the gas upon expansion, thus producing mechanical work. Because the mechanical work done by the gas in the expansion phase is larger than the compression work done to the gas in the compression phase, there is a net conversion of thermal to mechanical energy. In a thermoacoustic analogy, the piston can be seen as an acoustic wave that periodically perturbs the flame,~~ which replaces the hot gas~~. If this perturbation is such that more heat is released during moments of high pressure, as~~ occurs in a piston engine,~~ then there is more available work, which, if not dissipated, contributes to increase the oscillation amplitude,~~ thus leading to instability~~. This criterion, known as the Rayleigh criterion, was mathematically formulated in 1954 by Putnam and Dennis [10] as

$$\oint_{\Delta t}\int_{V} p'(\mathbf{x},t)\,\dot{q}'(\mathbf{x},t)\,d\mathbf{x}\,dt > 0 \tag{1.1}$$

where $p'(\mathbf{x},t)$ and $\dot{q}'(\mathbf{x},t)$ represent the fluctuating parts of pressure and heat release rate per unit volume, respectively, both at a given point in space $\mathbf{x}$ and instant in time t. In Eq. (1.1), the first integral is a cyclic integral to be evaluated over a time period of length Δt, whereas the second integral is a volume integral over the entire domain V. Eq. (1.1) expresses a condition for instability to occur, i.e. that heat must be added sufficiently in phase with the pressure. This equation was then revisited by Chu [11] to include the contributions of viscous dissipation and acoustic radiation from the system boundaries, whose effect is to subtract energy from the system, thus contributing to its stability. Although the qualitative explanation of the sound generated by a flame located inside a tube dates back to 1878, the Rayleigh criterion is still widely used nowadays to explain the physics behind thermoacoustic instabilities [12, 13].

At the industrial scale, thermoacoustic instabilities were first noted during the development of liquid-propellant rocket engines [14]. Aero and space engines are particularly susceptible to thermoacoustic oscillations due to their high powers, which means that even a very inefficient thermoacoustic mechanism can sustain large amplitude oscillations. For example, during the development of the Saturn V Rocket F-1 engine, pressure oscillations as large as the mean pressure of the combustion chamber were observed [15]. Typically, manufacturers test engine components individually and use the results to model the thermoacoustic behaviour of the full engine [16]. Based on these models, they design the engines to be thermoacoustically stable. Nevertheless, these models are not always accurate and thermoacoustic oscillations sometimes recur in the later stages of engine testing [17], leading to expensive redesign. Oefelein and Yang [2] report that a stable design of the Saturn V Rocket F-1 engine required approximately 2000 full-scale tests to eliminate thermoacoustic instabilities.

These observations have provided the motivation for research on how to reliably predict these phenomena. Alternative methods to trial-and-error experimental testing rely on a wide variety of computational methods. Direct Numerical Simulations (DNS) fully resolve the governing equations numerically, including acoustics, chemistry and turbulence, on a computational grid representing the physical domain. ~~This means that this type of simulation is as trustworthy as a laboratory experiment and additionally provides details that a real experiment is often not able to provide.~~ The downside of this is the still prohibitive computational cost [18], which makes DNS useless for industrial applications. Feasible approaches used in industry based on Computational Fluid Dynamics (CFD) rely on filtering the governing equations in time or space, thus resolving the large scales while modelling the small ones. Although this makes the problem computationally cheaper, many problems remain still challenging to solve due to the interaction of several physical mechanisms occurring at the same time, such as turbulence, combustion, aeroacoustics, thermoacoustics, etc. [19–24]. The simulations currently adopted in industry are based on the Reynolds-Averaged Navier Stokes (RANS) equations [25, 26]. These are obtained by averaging the governing equations in time. When doing so, a new term correponding to the time average of the product of the velocity fluctuations appears in the equations. This is referred to as the Reynolds stress tensor and requires a closure relationship. RANS simulations are ~~extremely~~ cheap to solve, but require good turbulence closures in order to be accurate. A valid alternative to RANS, but less accurate than DNS, is represented by Large Eddy Simulations (LES). LES filter the equations in space, aiming to resolve only the large-scale turbulent structures while modelling the subgrid-scale ones by means of an appropriate turbulence model. This approach allows to solve transient problems and provides a more detailed description than RANS. In fact, LES is an excellent tool at predicting both the flow field and the main unstable modes, even on very complex geometries [27, 28]. Nonetheless, it is typically used in academic contexts because its significant computational time prevents it to be adopted in industry [29]. A different approach to CFD, often used in conjuction with CFD, is represented by reduced-order models, a simplified approach that aims at capturing only the most relevant physics of the problem. An example are network models [30, 31], which work best for non-complex geometries. The idea of a network model is to split the domain into different elements, each of which is characterised by homogeneous properties (ρ, u, p), and connect the different elements by means of jump conditions. The assumption that is always made, which is often reasonable, is that the flame is acoustically compact, meaning that the length of the flame is negligible compared to the length of the first acoustic mode. Network models are extensively used in this thesis.

All these computational methods require a closure relationship to describe how heat release rate fluctuations interact with acoustic (i.e. pressure and velocity) fluctuations. This closure always introduces a degree of uncertainty because ~~by construction~~ these models lump complex physics into a handful ~~number~~ of model parameters [32]. An example of a frequently adopted thermoacoustic model is the so-called $n-\tau$ model, often related by people to Crocco [14], but first introduced by Summerfield [33]. According to this model, heat release rate fluctuations are assumed to be proportional to velocity fluctuations through an interaction index, n, and time-delayed with respect to them by a factor of τ. The time delay is a crucial parameter in determining the system stability. Because it lumps several physical mechanisms, such as atomization, vaporization, mixing and reaction in case of a liquid propellant, the time delay is particularly prone to uncertainty [34]. Despite being quite old, the $n-\tau$ model is still extensively used today, because it contains the most influential physics of thermoacoustic instabilities [35–37]. For more complex systems, the relationship between acoustic velocity and heat release rate fluctuations is usually specified as function of the forcing frequency [38–41]. This functional relationship is called flame transfer function (FTF) and represents an extension of the $n-\tau$ model, which is instead valid for a fixed frequency or in a small range of frequencies. An even more general model of a flame is represented by the flame describing function (FDF), where the flame response is modelled as function of both the frequency and the amplitude [38, 42–46]. Regardless of the reduced-order model used, we do not expect thermoacoustic model parameters to be universal constants: we accept the fact that they may vary when changing the system, but we would like to work with models whose parameters do not vary significantly when the configuration or the operating points of the same system change, e.g. heater position, boundary conditions, equivalence ratio.

From the above discussion, it is clear that there is no unique approach for tackling the problem of thermoacoustic instability. Every approach, regardless of whether experimental or computational, comes with advantages and disadvantages. In this thesis, we aim to develop a framework that combines the imperfect information coming from experiments with physics-based reduced-order models, which provide ~~by definition~~ a simplified description of the reality. This is done in order to extract as accurate information as possible from a physical system. The strong industrial motivation, combined with the recent availability of automated experiments [47] and hence large datasets for thermoacoustic systems, encourages the use of concepts of probability theory and statistical inference to turn qualitatively-correct thermoacoustic models into quantitatively-correct models that can be used for design [48, Future Issue 2]. This framework is developed in Sec. 1.2 and the techniques used in this thesis are thoroughly described and discussed in Secs. 1.3 and 1.4.

We conclude this section by briefly describing the thermoacoustic system we investigate throughout this thesis: an electrically-heated Rijke tube. This system, first studied by Rijke [49] in 1859, represents a perfect device to investigate thermoacoustic oscillations because, in spite of its simplicity, it contains much of the relevant physics present in a real engine. A Rijke tube consists of a cylindrical tube that contains an electric heater or a flame inside it [49]. The vertical tube is open at both ends. A mean flow is induced by natural convection and, on top of this mean flow, acoustic fluctuations occur. For the first acoustic mode, which is that observed in our experiments, a tube open at both ends experiences a velocity node and a pressure antinode at the centre, and a pressure node and a velocity antinode at both ends [50]. When placed in the bottom half of the tube, the heat source experiences moments of higher-than-average (lower-than-average) velocity during the compression (expansion) phase. Consequently, in this position, the heat transfer increases due to the higher velocity during the compression phase, and decreases due to the lower velocity during the expansion phase. There is also a short time delay τ between the velocity perturbation and the subsequent heat release rate fluctuation [51], introduced above when discussing the $n-\tau$ model. The time delay is small compared to an acoustic period, meaning that moments of increased (decreased) pressure occur during moments of increased (decreased) heat transfer. This converts heat into work over an acoustic cycle, as first described by Rayleigh [9]. If this work input exceeds the work output due to dissipation and acoustic radiation, the acoustic energy inside the tube grows. The position of the heat source inside the tube determines the strength of the thermoacoustic driving mechanism. A rudimentary analysis concurs with the experimental results of Saito [52] that its maximum strength occurs when the heat source is placed at a distance of one quarter of the tube length, measured from the bottom end. When the heat source is instead placed in the top half of the tube, moments of increased heat transfer coincide with moments of lower pressure and moments of decreased heat transfer coincide with moments of higher pressure. This causes the acoustic energy to always decrease. In this thesis, we limit our analysis to the linear regime, which refers to the onset of thermoacoustic oscillations and is characterized by exponential growth in amplitude [53]. The nonlinear regime, characterized by pressure oscillations with saturated amplitude, requires techniques from nonlinear dynamics theory for its investigation, and will not be dealt with in this work.

1.2 Statistical learning

Scientific research relies on observations, which typically come from either experiments or high-fidelity simulations. By observing the behaviour of a system, scientists build models to make predictions. Often ~~times~~ the role of a model is not to provide a full description of the system under investigation, ~~like the governing equations do,~~ but rather to approximate the system behaviour by capturing only the most relevant physical phenomena that are involved. This is particularly true for reduced-order models, which typically rely on just a handful ~~number~~ of parameters. As such, reduced-order models are intrinsically imperfect, i.e. characterized by *epistemic* error endemic to the model. On the other hand, observations are imperfect too. Even in the case of a perfectly calibrated experimental equipment, hence with no epistemic error, two measurements of the same quantity taken at two different times will rarely be identical, i.e. they will differ from the true value of that quantity. This is referred to as *aleatoric* error. In measurements theory, aleatoric error is typically assumed to follow a Gaussian distribution with zero mean and unknown variance [54]. The variance cannot be known exactly, but can be estimated by repeating the experiment several times. The higher the number of realizations, the higher the confidence in the estimation. In general, making estimates, building confidence intervals, and testing hypotheses by looking at data is what frequentist statistics does. Said in other words, frequentist statisticians try to extract in an *objective* way as much information contained in a dataset as possible. When dealing with a physical system, however, we often have some *a-priori* knowledge of the physical phenomena involved. This can be in the form of a reduced-order model available to us, for example. We would often want to exploit this a-priori knowledge, i.e. our *subjective* view about the system, in order to improve our predictions. Combining observations, always characterized by noise, with imperfect models is what Bayesian statistics does. We refer to Bayesian statistical inference as *statistical learning*.

The pillar of statistical learning is Bayes' theorem (or rule). In order to derive this theorem, we first need to introduce some simple statistical concepts. Given two random variables Ψ and Φ, the probability of two events, $\Psi = \psi$ and $\Phi = \phi$, occurring together is defined by the *joint* probability density function $p(\psi, \phi)$. The *conditional* probability density function $p(\psi|\phi)$ describes the probability of a certain event $\Psi = \psi$ to occur, given the event $\Phi = \phi$. Moreover, by definition of joint probability, we have that

$$p(\psi, \phi) = p(\psi|\phi)p(\phi) = p(\phi|\psi)p(\psi) \tag{1.2}$$

from which it is possible to derive Bayes' theorem (or rule)

$$p(\psi|\phi) = \frac{p(\psi)p(\phi|\psi)}{p(\phi)} \tag{1.3}$$

For convenience, we replace ϕ with d and re-write Eq. (1.3) as

$$p(\psi|d) = \frac{p(d|\psi)p(\psi)}{p(d)} \tag{1.4}$$

where d represents the data and ψ represents, for a given model, the model parameters or the model state. By model state we simply mean the quantities predicted by the model. In the context of Bayesian inference, $p(\psi|d)$ is the *posterior* distribution, i.e. the probability of ψ given d, whereas $p(d|\psi)$ is the *likelihood function*, i.e. the probability of d given ψ, and $p(\psi)$ the *prior*. The denominator of the right-hand side of Eq. (1.4) is referred to as *evidence* or *marginal likelihood* and, for given d, represents a normalization constant that ensures that $p(\psi|d)$ integrates to 1 [55]:

$$p(d) = \int p(\psi, d)\, d\psi = \int p(d|\psi)p(\psi)\, d\psi \tag{1.5}$$

where the integration is intended over the entire ψ-space defined by the prior $p(\psi)$. Eq. (1.5) effectively evaluates the likelihood function, $p(d|\psi)$, integrating out or marginalizing out the prior (from here the name marginal likelihood). Eq. (1.5) can be computed, for example, using a Monte Carlo integration. For model comparison, computing Eq. (1.5) is not necessary because what we are ultimately interested in is the ratio:

$$\frac{p(\psi_2|d)}{p(\psi_1|d)} = \frac{p(d|\psi_2)p(\psi_2)}{p(d|\psi_1)p(\psi_1)} \tag{1.6}$$

to see which one of the two models (subscripts 1 and 2) has the highest posterior, i.e. the highest probability of being a better description of the data. These concepts are useful for understanding how the Markov Chain Monte Carlo method works. This will be detailed in Sec. 1.4.

Eq. (1.4) encapsulates the essence of what an *inverse problem* is: starting from some observations, we want to infer the parameters of a given model that best explain those observations, and quantify their uncertainty. This is called *inverse uncertainty quantification*. On the other hand, a *forward problem* is the propagation of the uncertainty from the parameters to the state. This can be done, for example, using a standard Monte Carlo method. Typically, one wants to first solve the inverse problem so as to quantify the uncertainty in the parameters, and then the forward problem so as to quantify the uncertainty in the state. This is because the uncertainty in the parameters is usually not known a priori. When dealing with time series, the inverse problem is usually referred to as *data assimilation*: typically, the model marches forward in time, and the estimates of model state and parameters improve every time new observations become available for assimilation. Kalman filters are especially useful for this ~~purpose~~ because they provide the optimal estimate of state and parameters, and corresponding uncertainty, at a given time, given all past observations (see Sec. 1.3). Kalman smoothers, ~~instead,~~ look at both past and future observations, and hence provide more robust estimates. The downside of this is that Kalman smoothers cannot be used for on-the-fly (i.e. real-time) data assimilation, simply because future observations are not available in real time.

Techniques from the field of inverse problems [56–58] were originally developed for oceanography and meteorology [59, 60]. These methods have become popular in fluid mechanics, for example in turbulent flow around aircraft [61], optimal sensor placement [62], mean flow reconstruction [63], and unsteady separated flow aerodynamics [64]. In the field of combustion, ensemble Kalman filters and smoothers have been used to tune the parameters of a qualitatively-correct kinematic flame model using DNS results [65] and experimental images [66], thus rendering them quantitatively accurate with a known error. Similarly, Labahn et al. [67] used an ensemble Kalman filter to assimilate high-speed experimental measurements into a Large Eddy Simulation in order to capture local extinction events in turbulent flames. Sengupta et al. [68] trained a heteroscedastic Bayesian Neural Network on a large amount of synthetic flame videos to infer the parameters of a G-equation model on the fly. Other methods, which are used for forward uncertainty quantification, have also been successfully applied to different combustion problems. For example, Guo et al. [69] used a Gaussian process to perform high-dimensional uncertainty quantification for both linear and nonlinear thermoacoustic instability analysis. Silva et al. [70] combined intrusive generalized Polynomial Chaos with a state-space thermoacoustic model to account for uncertainties in combustion noise prediction of confined flames. Avdonin et al. [71] used non-intrusive polynomial chaos expansion for forward uncertainty quantification and sensitivity analysis of thermoacoustic stability of two premixed flame configurations. Magri et al. [72] used standard Monte Carlo and Active Subspace Identification methods, in conjuction with adjoint sensitivity, to evaluate the thermoacoustic risk factor of two annular combustor configurations. In the field of thermoacoustics, recent studies have applied simple methods to identify the parameters of thermoacoustic models. Ghani et al. [73] used non-gradient-based optimization methods applied to network models of (i) a Rijke tube, (ii) a 14 kW laboratory burner operating in the laminar regime, and (iii) a 86.5 kW laboratory burner operating in the turbulent regime. Using a data-driven identification framework, Ghani et al. [73] successfully retrieved a flame model from experimental limit cycle measurements at specific operating points, but without testing the same model on the whole system. A highly detailed model of thermoacoustic oscillations in an electrically-heated Rijke tube was developed by Matveev [74]. Despite being painstakingly tuned to be quantitatively correct at one heater position (Figure 5-5 of [74]), this model was only qualitatively correct at nearby heater positions (Figures 5-6, 5-7, 5-8 of [74]). For larger devices, accurate prediction of thermoacoustic oscillations is similarly challenging [3].

The concept underlying this thesis is that thermoacoustic models contain systematic error and that their behaviour is so sensitive to this error that one cannot confidently construct quantitatively-accurate models *a priori* based on the behaviour of their components [75]. Instead, we propose to generate qualitatively-accurate models, which are general, and then to tune their parameters using statistical learning techniques so that they become quantitatively accurate. This approach allows us to evaluate probabilistically the adequacy (how well the model captures the trend in the data), the accuracy (how well the model fits the data), and the uncertainty of the proposed models. One of the purposes of this thesis is indeed to investigate and compare different thermoacoustic closure relationships both qualitatively and quantitatively, so as to find as a general model as possible, for a given system. This is done in Chapter 5. The methods used in this study lie at the interface between data science and physical science. From a data science perspective, we are training a model based on several hundred thousand observations, as we would if using neural networks or Gaussian process regression. Unlike a neural network, however, the model is strongly constrained by physics. The advantage of such a formulation, with respect to an entirely data-driven approach, is the gain in flexibility. Indeed, a physics-based model should remain, at least in principle, reasonably accurate when extrapolating beyond the range tested, due to the fact that it is based on physical principles.

This thesis builds upon the PhD thesis of Hans Yu [76], who set the basis for this work. In particular, [76] provided a robust and general theoretical framework of different Bayesian techniques used to solve eigenproblems and time-series problems. Among other things, [76] implemented and applied the Ensemble Kalman Filter (EnKF) to a G-equation model of a flame, assimilating high-quality images of the flame front using both experimental and DNS results. In the present thesis, we use the EnKF developed by [76] to investigate a different time-series problem, introduced and thoroughly discussed in Chapter 3. From the point of view of the techniques used, in addition to ~~what done by~~ [76], the present work introduces a statistical learning technique ~~never used before in the field of~~ thermoacoustics: the Markov Chain Monte Carlo method, described in Sec. 1.4. This has been ~~implemented by the author of this thesis and~~ applied to the eigenproblems discussed in Chapters 4 and 5. The MCMC is a general inverse uncertainty quantification technique and, as such, can be used with any model and any dataset. ~~Therefore, the wish is that this work is useful for future studies made by other members of the research group the author is part of at the University of Cambridge~~.

1.3 Ensemble Kalman filter

The Kalman filter (KF) is a sequential data assimilation method in which state and parameters of a *linear* model are improved every time new data become available. The theoretical background and the equations presented in this section are based on [57, §3]. We define G as the linear operator that evolves the model state by one timestep. Here the scalar quantity ψ represents the model state. We describe how model parameters are included in this analysis at the end of this section. We aim to obtain the best possible estimate of the true state ψ^{t}, given a model forecast ψ^{f} characterized by the unknown model error δ^{f}, and given the measurement d characterized by the unknown measurement error ε:

$$\psi^{\mathrm{f}} = \psi^{\mathrm{t}} + \delta^{\mathrm{f}} \tag{1.7}$$

$$d = \psi^{\mathrm{t}} + \varepsilon \tag{1.8}$$

The underlying assumptions of the KF are that δ^{f} and ε are normally distributed with zero mean and known variances, $C^{\mathrm{f}}_{\psi\psi}$ and $C_{\varepsilon\varepsilon}$, respectively. Hence the prior and the likelihood function can be expressed as

$$p(\psi) \propto \exp\left(-\frac{1}{2}(\psi-\psi^{\mathrm{f}})(C^{\mathrm{f}}_{\psi\psi})^{-1}(\psi-\psi^{\mathrm{f}})\right) \qquad \text{(prior)} \tag{1.9}$$

$$p(d|\psi) \propto \exp\left(-\frac{1}{2}(\psi-d)C^{-1}_{\varepsilon\varepsilon}(\psi-d)\right) \qquad \text{(likelihood function)} \tag{1.10}$$

According to Bayes'rule (Eq. (1.4)), the posterior distribution becomes

$$p(\psi|d) \propto p(d|\psi)p(\psi) \propto \exp\left(-\frac{1}{2}\mathscr{J}[\psi]\right) \tag{1.11}$$

where

$$\mathscr{J}[\psi] = (\psi-\psi^{\mathrm{f}})(C^{\mathrm{f}}_{\psi\psi})^{-1}(\psi-\psi^{\mathrm{f}}) + (\psi-d)C^{-1}_{\varepsilon\varepsilon}(\psi-d) \tag{1.12}$$

Minimizing Eq. (1.12) corresponds to finding the maximum likelihood estimate of $p(\psi|d)$. This gives the improved analyzed estimate ψ^{a} of ψ^{t}, and its variance $C^{\mathrm{a}}_{\psi\psi}$, based on both d and ψ^{f}

$$\psi^{\mathrm{a}} = \psi^{\mathrm{f}} + \frac{C^{\mathrm{f}}_{\psi\psi}}{C^{\mathrm{f}}_{\psi\psi}+C_{\varepsilon\varepsilon}}(d-\psi^{\mathrm{f}}) \tag{1.13}$$

$$C^{\mathrm{a}}_{\psi\psi} = C^{\mathrm{f}}_{\psi\psi}\left(1-\frac{C^{\mathrm{f}}_{\psi\psi}}{C^{\mathrm{f}}_{\psi\psi}+C_{\varepsilon\varepsilon}}\right) \tag{1.14}$$

where Eqs. (1.13) and (1.14) represent the so-called *analysis step* (superscript a), i.e. they provide an improved estimate of the state based on the degree of belief in both the model and the observation. The KF is guaranteed to be the optimal sequential data assimilation method for linear dynamics [57, §4.1]. The term "optimal" means that our estimator of the analyzed state is unbiased and with minimum error variance (assuming normal distributions). Starting from an estimate of the state's expected value and its variance (ψ^{f} and $C^{\mathrm{f}}_{\psi\psi}$), we update its expected value and variance (ψ^{a} and $C^{\mathrm{a}}_{\psi\psi}$) as data ($d$ and $C_{\varepsilon\varepsilon}$) become available. Once this new state is found, we integrate forward in time using the linear operator G. The time evolution is described by

$$\psi^{\mathrm{f}}(t_k) = G\psi^{\mathrm{a}}(t_{k-1}) \tag{1.15}$$

$$C^{\mathrm{f}}_{\psi\psi}(t_k) = GC^{\mathrm{a}}_{\psi\psi}(t_{k-1})G + C_{qq}(t_{k-1}) \tag{1.16}$$

where C_{qq} is the model error variance. (The model is imperfect over one time step. We assume that the model error is normally distributed with zero mean and variance C_{qq}.) Given an appropriate initial condition, Eqs. (1.15) and (1.16) can be used to forecast the state at each timestep, and every time new measurements become available, an analyzed estimate can be calculated using Eqs. (1.13) and (1.14). These equations define the KF for a linear scalar model and can be easily extended to the multidimensional case.

Despite the Kalman Filter being the best method for sequential data assimilation, its use is restricted to a relatively small category of problems. Indeed, its main drawbacks are the linearity assumption, which is often not valid in practical problems, and the fact that a covariance matrix $\boldsymbol{C}^{\mathrm{a}}_{\psi\psi}$ needs to be stored. In particular, if the model state vector consists of n variables, the covariance matrix size scales with $\mathscr{O}(n^2)$, and, for problems with many thousand degrees of freedom, the computational requirements associated to its storage are too high. This motivated people to find an alternative to circumvent these two problems. A new method, the Extended Kalman Filter (EKF), was derived to tackle the first drawback by linearising the nonlinear model operator in the true state $G(\psi^{\mathrm{t}}_k)$ about the analysed state $G(\psi^{\mathrm{a}}_k)$ using a Taylor series expansion. In other words, unlike the classic Kalman Filter, which linearly advances forward in time the mean and the covariance matrix of a Gaussian distribution using Eqs. (1.15) and (1.16), the Extended Kalman Filter aims to propagate the same quantities allowing for weak nonlinearities. Nonetheless, this method is not very successful because for strong nonlinearities one would need to retain many high-order terms in the Taylor series expansion in order for the method to be accurate, making it cumbersome. Moreover, the EKF does not solve the problem related to the need to store a covariance matrix.

The ensemble Kalman filter (EnKF) is a convenient solution to both problems (nonlinear models and computational cost) [57, §4.3]. Rather than evolving the mean and covariance matrix over time, the EnKF samples from a probability distribution and marches each member of the ensemble forward in time. By doing so, possible model nonlinearities are accounted for in the prediction step. Before the analysis step, a Gaussian distribution is reconstructed from the ensemble members. Then measurements are assimilated in a similar way to the KF. A schematic of this procedure is reported in Fig. 1.1. The fact that non-Gaussian contributions in the forecast state are not taken into account in the analysis step makes the scheme approximate. However, as highlighted by Evensen [57, §4.3.3], the analysis step is not a pure resampling of a Gaussian posterior distribution because the algorithm encapsulates many of the nonlinear effects through the prediction step. The resulting solution lies between a fully linear Gaussian update and an exact Bayesian computation. Furthermore, the algorithm is easy to implement and parallelize, and is computationally cheap because most of the computations reduce to matrix-vector multiplications that can be run in parallel.

For completeness, we report the main steps of the EnKF scheme for the multidimensional case and highlight the differences with the classical KF. The error covariance matrices for the forecast and analyzed estimate, $\boldsymbol{C}^{\mathrm{f}}_{\psi\psi}$ and $\boldsymbol{C}^{\mathrm{a}}_{\psi\psi}$, are replaced with their ensemble version

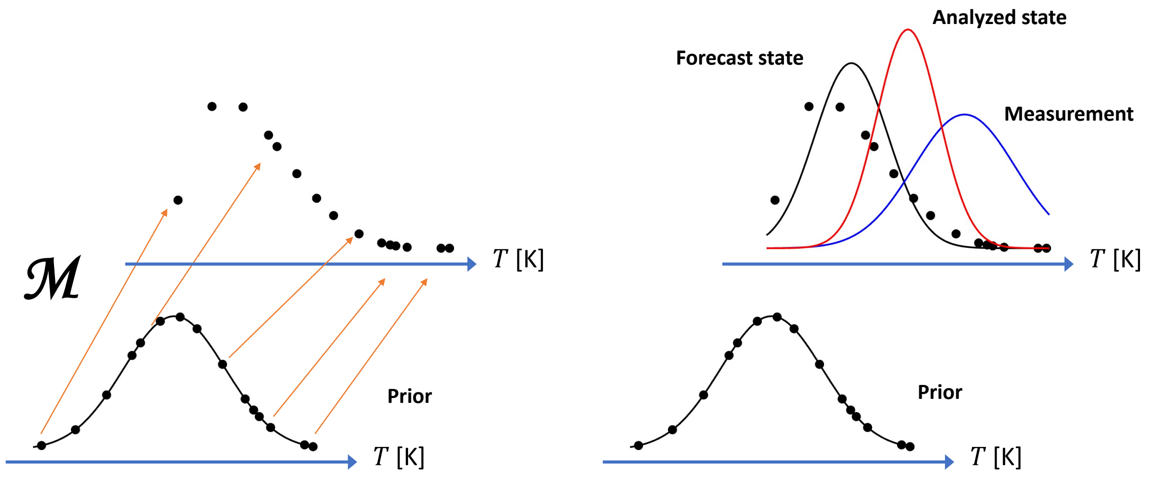

(a) Forecast step (b) Analysis step

Fig. 1.1 Qualitative schematic of the ensemble Kalman filter with a nonlinear temperature model $\mathscr{M}$. Black dots represent the ensemble members. (a) Prediction step. Each ensemble member evolves according to $\mathscr{M}$, and the corresponding new distribution is non-Gaussian if the model is nonlinear. (b) Analysis step. A Gaussian distribution representing the forecast state is reconstructed from the evolved ensemble members, and the analyzed step is computed, given the (Gaussian) distributions of the forecast state and the measurement.

(superscript e), $(\boldsymbol{C}^{\mathrm{e}}_{\psi\psi})^{\mathrm{f}}$ and $(\boldsymbol{C}^{\mathrm{e}}_{\psi\psi})^{\mathrm{a}}$, computed using ensemble-average quantities, denoted by $\overline{(\cdot)}$

$$(\boldsymbol{C}^{\mathrm{e}}_{\psi\psi})^{\mathrm{f}} = \overline{(\boldsymbol{\psi}^{\mathrm{f}} - \overline{\boldsymbol{\psi}^{\mathrm{f}}})(\boldsymbol{\psi}^{\mathrm{f}} - \overline{\boldsymbol{\psi}^{\mathrm{f}}})^{\mathrm{T}}} \approx \overline{(\boldsymbol{\psi}^{\mathrm{f}} - \boldsymbol{\psi}^{\mathrm{t}})(\boldsymbol{\psi}^{\mathrm{f}} - \boldsymbol{\psi}^{\mathrm{t}})^{\mathrm{T}}} = \boldsymbol{C}^{\mathrm{f}}_{\psi\psi} \tag{1.17}$$

$$(\boldsymbol{C}^{\mathrm{e}}_{\psi\psi})^{\mathrm{a}} = \overline{(\boldsymbol{\psi}^{\mathrm{a}} - \overline{\boldsymbol{\psi}^{\mathrm{a}}})(\boldsymbol{\psi}^{\mathrm{a}} - \overline{\boldsymbol{\psi}^{\mathrm{a}}})^{\mathrm{T}}} \approx \overline{(\boldsymbol{\psi}^{\mathrm{a}} - \boldsymbol{\psi}^{\mathrm{t}})(\boldsymbol{\psi}^{\mathrm{a}} - \boldsymbol{\psi}^{\mathrm{t}})^{\mathrm{T}}} = \boldsymbol{C}^{\mathrm{a}}_{\psi\psi} \tag{1.18}$$

It is then essential to define an ensemble of observations such that for each ensemble member

$$\boldsymbol{d}_j = \boldsymbol{d} + \boldsymbol{\varepsilon}_j \tag{1.19}$$

with $j = 1, \dots, N$, where N is the ensemble size. We now define the ensemble covariance matrix of the measurement errors as

$$\boldsymbol{C}^{\mathrm{e}}_{\varepsilon\varepsilon} = \overline{\boldsymbol{\varepsilon}\boldsymbol{\varepsilon}^{\mathrm{T}}} \tag{1.20}$$

Thus the analysis step for each ensemble member is

$$\boldsymbol{\psi}^{\mathrm{a}}_j = \boldsymbol{\psi}^{\mathrm{f}}_j + \boldsymbol{K}_{\mathrm{e}}(\boldsymbol{d}_j - \boldsymbol{M}\boldsymbol{\psi}^{\mathrm{f}}_j) \tag{1.21}$$

$$(\boldsymbol{C}^{\mathrm{e}}_{\psi\psi})^{\mathrm{a}} = (\boldsymbol{I} - \boldsymbol{K}_{\mathrm{e}}\boldsymbol{M})(\boldsymbol{C}^{\mathrm{e}}_{\psi\psi})^{\mathrm{f}} \tag{1.22}$$

$$\boldsymbol{K}_{\mathrm{e}} = (\boldsymbol{C}^{\mathrm{e}}_{\psi\psi})^{\mathrm{f}}\boldsymbol{M}^{\mathrm{T}}\left(\boldsymbol{M}(\boldsymbol{C}^{\mathrm{e}}_{\psi\psi})^{\mathrm{f}}\boldsymbol{M}^{\mathrm{T}} + \boldsymbol{C}^{\mathrm{e}}_{\varepsilon\varepsilon}\right)^{-1} \tag{1.23}$$

where $\boldsymbol{I}$ is the identity matrix, $\boldsymbol{K}_{\mathrm{e}}$ is the Kalman gain, $\boldsymbol{M}$ is a matrix that maps the state vector to the measurement vector, and $\boldsymbol{M}^{\mathrm{T}}$ is its transpose. The presence of $\boldsymbol{M}$ allows us to infer not only the model state, but also the model parameters. This is achieved by simply appending the parameters to the vector $\boldsymbol{\psi}$. The forecast state estimate is obtained by marching each member of the ensemble forward in time, thus accounting for possible model nonlinearities. The forecast covariance matrix is computed using the deviations from the ensemble mean (Eq. (1.17)). For linear dynamics, it can be proved that the EnKF converges to the KF for ensemble sizes tending to infinity [57, §4.1.3].

1.4 Markov Chain Monte Carlo

A Markov chain is a discrete-time stochastic model that consists of a sequence of events such that the probability of a certain event occurring depends uniquely on the event at the previous timestep. The background theory and equations presented in this section are based on [58, §11]. When dealing with continous time, we speak of a Markov process rather than a Markov chain. Markov Chain Monte Carlo (MCMC) is a statistical method whose goal is to obtain a sample from a target posterior distribution, $p(\boldsymbol{\psi}|\boldsymbol{d})$. Here $\boldsymbol{\psi}$ represents a vector containing the model parameters. The idea is to draw samples $\boldsymbol{\psi}$ from approximate distributions and correct those draws over time such that the approximate distributions converge to the target posterior distribution. In practice, one creates several independent chains starting from different initial points $\boldsymbol{\psi}^0$ in the parameter space. Then, at each timestep t and for each chain, a new value $\boldsymbol{\psi}^t$ is drawn from a *transition distribution*, $\mathscr{T}(\boldsymbol{\psi}^t|\boldsymbol{\psi}^{t-1})$, that depends only on the previous draw, $\boldsymbol{\psi}^{t-1}$. Many MCMC algorithms have been developed, differing in complexity and efficiency. In this study we use the Metropolis algorithm, whose steps can be summarized as follows:

1. An appropriate prior distribution $p(\boldsymbol{\psi})$ over the model parameters is chosen and a sample $\boldsymbol{\psi}^0 (= \boldsymbol{\psi}^{t-1})$ is drawn from it.

2. At time t, a sample $\boldsymbol{\psi}^*$ is drawn from a *proposal distribution*, $\mathscr{R}(\boldsymbol{\psi}^*|\boldsymbol{\psi}^{t-1})$, which must be symmetric, i.e. $\mathscr{R}(\boldsymbol{\psi}_a|\boldsymbol{\psi}_b) = \mathscr{R}(\boldsymbol{\psi}_b|\boldsymbol{\psi}_a)$ for any $\boldsymbol{\psi}_a$, $\boldsymbol{\psi}_b$. (Other algorithms relax the symmetry assumption.)

3. Based on Eq. (1.4), the acceptance ratio r is computed

$$r = \frac{p(\boldsymbol{\psi}^*|\boldsymbol{d})}{p(\boldsymbol{\psi}^{\mathrm{t}-1}|\boldsymbol{d})} = \frac{p(\boldsymbol{d}|\boldsymbol{\psi}^*)p(\boldsymbol{\psi}^*)}{p(\boldsymbol{d}|\boldsymbol{\psi}^{t-1})p(\boldsymbol{\psi}^{t-1})} \tag{1.24}$$

4. From a uniform distribution with bounds $[0,1)$, a random value ω is extracted.

5. The value $\boldsymbol{\psi}^t$ for the next iteration is set to:

$$\boldsymbol{\psi}^t = \begin{cases} \boldsymbol{\psi}^*, & \text{if } \omega < \min(r,1) \\ \boldsymbol{\psi}^{t-1}, & \text{otherwise} \end{cases} \tag{1.25}$$

6. The new $\boldsymbol{\psi}^t$ replaces $\boldsymbol{\psi}^{t-1}$ in (ii) for the next iteration and the steps are repeated.

A simplified schematic of how the Metropolis algorithm works is reported in Fig. 1.2. It can be proved that the above algorithm converges to the target posterior distribution. Here we limit our discussion to Eq. (1.25): the algorithm always accepts values of $\boldsymbol{\psi}^*$ that increase the posterior density, but only sometimes accepts downward values. The fact that it does not always reject downward values preserves the stochastic nature of the algorithm. Thus, the MCMC essentially constructs a biased random walk that explores the target posterior distribution in the parameter space. The above steps are performed for many chains starting from different initial conditions. The starting point of each chain is typically a low-density region of the posterior. Because each chain is independent of the others, the algorithm can be easily parallelized. For each chain, the initial portion of accepted samples (called *burn-in* or *warm-up*) is discarded, and only converged samples are retained. To determine the length of the burn-in, we inspect the evolution of the posterior density, and discard a certain number of initial samples depending on the number of iterations it takes for all the chains to leave low-density regions and move to high-density regions of the posterior. Termination occurs when the chains are deemed converged using metrics such as the Gelman-Rubin convergence diagnostic [77] or, more simply, when the Markov chains are sufficiently well mixed, as shown in Chapter 4. At the end of the process, the resulting samples can be used to visualize the posterior distribution and, more importantly, to make predictions and propagate parameter uncertainty through the model.

Choosing an appropriate proposal distribution $\mathscr{R}(\boldsymbol{\psi}^*|\boldsymbol{\psi}^{\mathrm{t}-1})$ is key to determining the performance of the algorithm: each jump in the parameter space must be big enough (otherwise the random walk moves too slowly), but at the same time the number of rejected jumps must not be too large (otherwise the random walk wastes too much time without moving at all). When dealing with few parameters, the covariance matrix entries of the proposal distribution can be chosen simply by trial and error. On the other hand, if the number of parameters increases significantly, the covariance matrix should change over time for efficiency purposes. In this case, more sophisticated samplers with adaptive schemes, such as the No-U-Turn sampler [78], should be preferred.

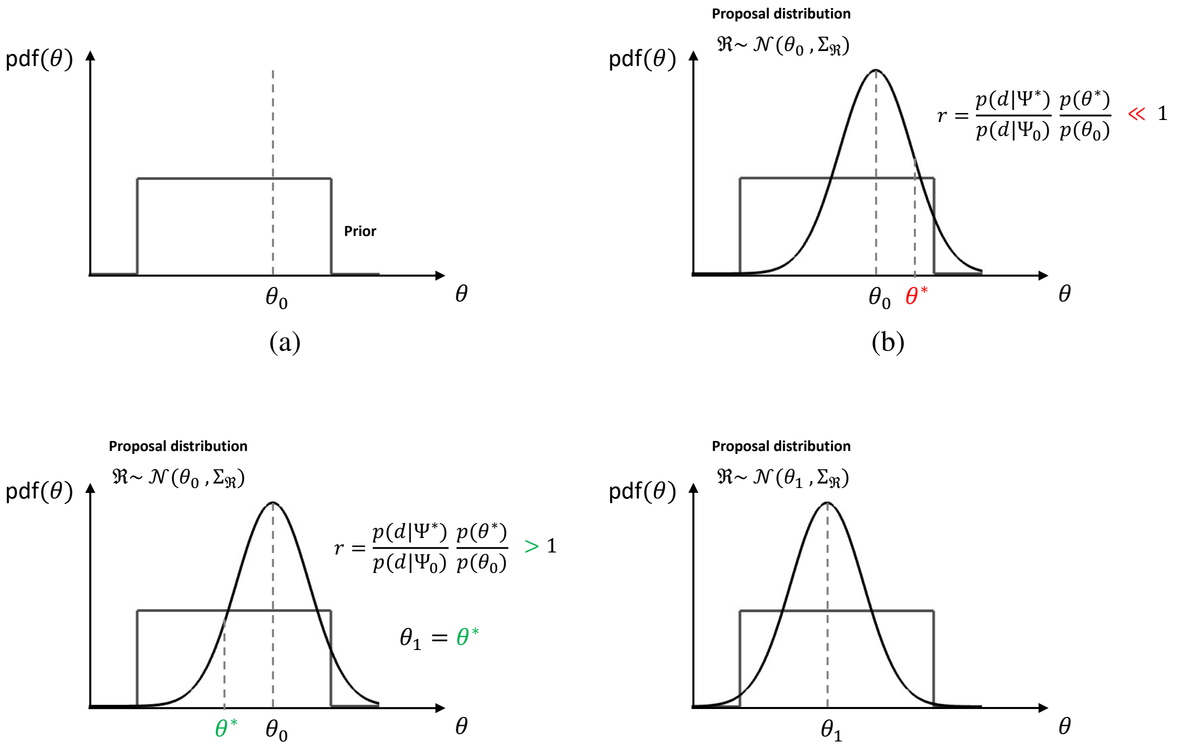
pdf(θ)
Prior
θ_0
θ
Proposal distribution
$\Re \sim \mathcal{N}(\theta_0, \Sigma_\Re)$
$r = \frac{p(d|\Psi^*)}{p(d|\Psi_0)} \frac{p(\theta^*)}{p(\theta_0)} \ll 1$
θ^*
$r = \frac{p(d|\Psi^*)}{p(d|\Psi_0)} \frac{p(\theta^*)}{p(\theta_0)} > 1$
$\theta_1 = \theta^*$
$\Re \sim \mathcal{N}(\theta_1, \Sigma_\Re)$
θ_1

(a) (b)

(c) (d)

Fig. 1.2 Qualitative schematic of the MCMC Metropolis algorithm. We assume a model $\mathscr{M}$ made up of one parameter only, θ. The model state is $\Psi = \mathscr{M}(\theta)$. We have one observation available, d. (a) We choose a prior distribution in the parameter space, e.g. a uniform distribution, and take a sample from it, θ_0. (b) We assume a Gaussian proposal distribution $\mathscr{R}$ with covariance matrix $\Sigma_{\mathscr{R}}$. We then center it around θ_0 and take a sample from it, θ^*. We compute the acceptance ratio, r. $\big($With a uniform prior, $p(\theta^*) = p(\theta_0)$.$\big)$. If $r \ll 1$, the algorithm will likely reject θ^*. (c) If this occurs, we take a new sample θ^* from the same proposal distribution. If $r > 1$, the algorithm definitely accepts θ^*, and we set $\theta_1 = \theta^*$. This value corresponds to a sample from the posterior, hence it is stored. (d) We center the proposal distribution around θ_1 and keep sampling from it, repeating the above steps until we collect several samples from the posterior distribution.

The MCMC is a more powerful tool than the EnKF because it makes fewer restrictive assumptions about the target posterior and therefore reconstructs its distribution more accurately. In particular, it does not assume that the posterior distribution is Gaussian. It can therefore explore any possible nonlinearity and multimodality present in the posterior. The downside is a higher computational cost. The main consequence of this is that, unlike the EnKF, the MCMC cannot cope with on-the-fly data assimilation. For on-the-fly data assimilation, a way to fully reconstruct the posterior distribution is by using *particle filters*, which work similarly to the EnKF but do not make any Gaussian assumption. For this reason, particle filter are significantly more expensive than EnKF, but much more efficient than MCMC when it comes to on-the-fly data assimilation. Description of particle filters is out of the scope of this thesis.

Chapter 2

Experimental setup

This chapter provides a detailed description of the experimental setup used to obtain the data. First, we describe the apparatus. Second, we explain how the data are acquired. Third, we discuss how the data are processed and show the experimental results. These results are used to train physics-based models in the next chapters.

2.1 Apparatus

In this section, we describe the experimental apparatus. A sketch of the laboratory rig is shown in Fig. 2.1. The rig consists of a 1 m long stainless steel vertical tube with an internal diameter of 47.4 mm and a wall thickness of 1.7 mm. An electric heater is attached to two thin threaded metal prongs and held in place at different positions. The heater consists of two concentric ceramic rings of the same external diameter as that of the tube, wrapped several times by a 0.559 mm diameter Ni-Cr filament (Fig. 2.2). The heater is powered by an Elektro-Automatik EA-PSI 5080-20 A DC programmable power supply with maximum power 640 W, controlled through National Instruments LabVIEW. A 4 Ω Visaton FRS 8 loudspeaker is placed near the base of the tube and is connected to a Stage Line STA-500 Pro Power amplifier with maximum power 600 W controlled through National Instruments LabVIEW. The experimental apparatus, as described so far, is that in [47, 79–81]. Six G.R.A.S. 40SA probe microphones are used to record the pressure near the inner surface of the tube at the following axial locations, measured from the bottom end of the tube: $x_\mathrm{m}/L = [0.45, 0.55, 0.65, 0.75, 0.85, 0.95]$. Each microphone is equipped with a 20 mm long probe, on top of which a temperature shield is mounted. All data is acquired through a National Instruments BNC-2110 DAQ device using LabVIEW. Eight type-K thermocouples are installed along the centreline of the tube through small holes at positions $x_\mathrm{t}/L = [0.20, 0.30, 0.40, 0.50, 0.60, 0.70, 0.80, 0.90]$ from the bottom end. An additional thermocouple is placed near the inlet section to record the ambient temperature. All the thermocouples are logged with four TC-08 USB DAQ boxes. A ~~large~~ LabView code deals with the full automation of the system and allows us to run experiments overnight. Finally, some sound absorbing foam is used to seal the laboratory door to minimize the external noise. This allows us to carry out ~~very~~ clean and accurate experiments.

2.2 Data acquisition

Experiments are conductued at the following heater positions, measured from the bottom end: $x_\mathrm{h}/L = [0.10, 0.15, 0.20, 0.25, 0.30, 0.35, 0.40, 0.45, 0.50, 0.55]$. When the heater is switched off, the heater position $x_\mathrm{h}/L = 0.01$ is also investigated. (The latter cannot be investigated when the heater is switched on because our heat transfer model breaks down when the heater is too close to the bottom end.) When the heater is switched on, the input power is increased every 70 minutes in steps of 10 W, from 10 W to 180 W, resulting in a 21-hour long fully-automated run. In this range of powers, the system is thermocoustically stable at every heater position, hence the acoustic ping provided through the loudspeaker dies out. The corresponding decay rate and frequency depend, however, on the thermoacoustic driving from the heater. Because voltage and current provided by the power supply fluctuate over time, a PID controller is implemented in LabView so that the provided power is as close as possible to the desired power. This results in fluctuations of less than 1 W, which is small compared to the desired powers.

All the thermocouples simultaneously provide a temperature measurement every 7 seconds. The loudspeaker provides sinusoidal acoustic pings at a frequency of 170 Hz, close to the natural frequency of the tube, which depends on the speed of sound inside the tube. The acoustic ping and the successive decay are recorded by means of the six probe microphones, which measure the pressure in the proximity of the inner surface of the tube with a sampling frequency of 10 kHz. This is higher than the anticipated frequencies of the thermoacoustic oscillations, 165 to 190 Hz. The high sampling rate guarantees that no aliasing effects occur and reduces measurement error in the growth rate and frequency.

For each heater position, the following set of experiments is carried out in sequence: (i) 100 acoustic pings with the empty tube (one ping every 3 s); (ii) 100 acoustic pings with the heater in place but switched off and without the thermocouples (one ping every 3 s); (iii) 100 acoustic pings with both the heater switched off and the thermocouples in place (one ping every 3 s); (iv) 10800 acoustic pings with the heater switched on and the thermocouples in place (one ping every 7 s). The cold flow experiments are performed manually in about 15

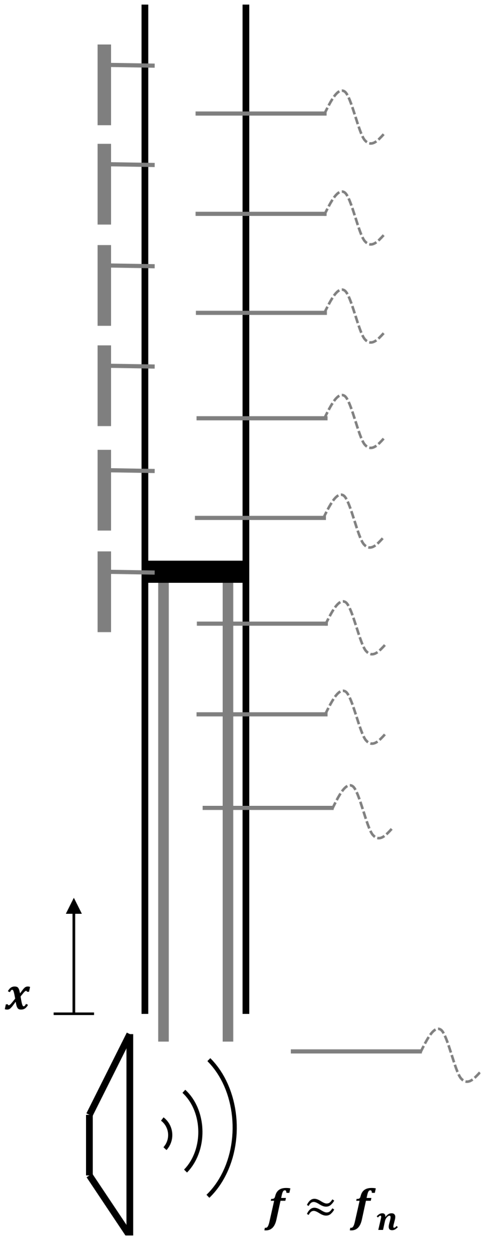

Fig. 2.1 Sketch of the experimental apparatus including 6 microphones, 8 thermocouples to measure the gas temperature at the tube centerline, a thermocouple to measure the ambient temperature, a loudspeaker, and an electric heater held in place by a pair of prongs and connected to a pair of electric wires. Note that the loudspeaker acoustically forces the system at a frequency, f, close to the natural frequency of the tube, f_{n}.

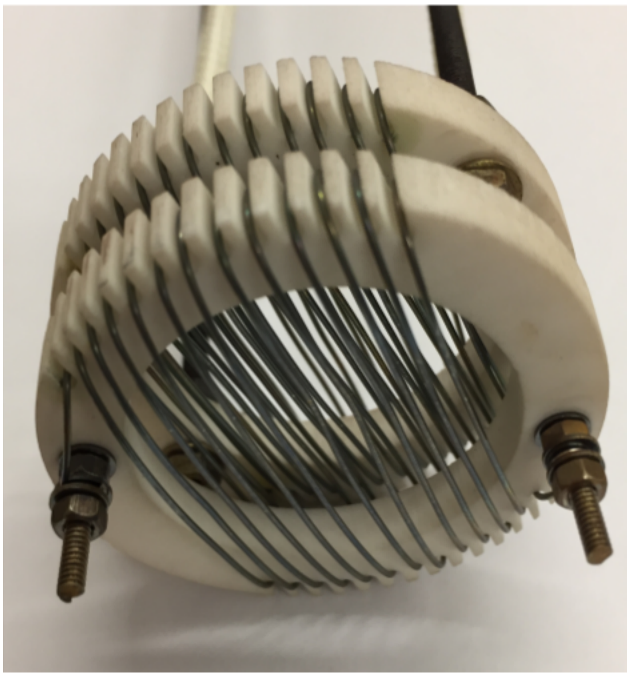

Fig. 2.2 Electric heater made up of 0.559 mm diameter Ni-Cr filaments wound between two parallel ceramic rings.

minutes. This sequence of experiments allows us to isolate the effect of heater, thermocouples and thermoacoustic mechanism, respectively.

Overall, the experimental campaign lasted approximately three weeks and required several months of preparation. The campaign resulted in $\mathscr{O}(10^5)$ acoustic pings, each measured by six probe microphones, and $\mathscr{O}(10^6)$ temperature measurements. The complete database can be found in Ref. [82]. In this database the following folders are included: `1_cold_emptyTube` contains the pressure measurements of the 100 acoustic pings performed for every heater position before the heater and thermocouples are placed in the tube, `2_cold_heaterOff` contains the pressure measurements of the 100 acoustic pings for every heater position in the presence of the heater switched off and without thermocouples, `3_cold_heaterOff_withThermocouples` contains the pressure measurements of the 100 acoustic pings for every heater position in presence of both the heater switched off and the eight thermocouples, `4_hot` contains the pressure measurements of the acoustic pings as well as the temperature measurements for every heater position when the heater is switched on and the thermocouples are present. `README` files are included to provide additional details such as the ambient temperature values in the cold flow experiments, the experiment setup and how to import files in binary format.

2.3 Data analysis and results

Before performing any experiments, we calibrate the thermocouples to minimize systematic measurement error. To do so, we record the temperature measured by all the thermocouples at two known temperatures: $T = 23$ °C (ambient temperature) and $T = 100$ °C (temperature of steam out of a kettle). We denote by $T_\mathrm{t}(23\ ^\circ\mathrm{C})$ and $T_\mathrm{t}(100\ ^\circ\mathrm{C})$ the corresponding temperatures measured by the generic thermocouple. The thermocouples are found to all agree (to within 0.1 °C) with the ambient temperature, i.e. we can safely assume $T_\mathrm{t}(23\ ^\circ\mathrm{C}) = 23\ ^\circ\mathrm{C}$. Furthermore, a linear calibration procedure is used for simplicity. Thus, to compute the calibrated temperature T, starting from the measured temperature T_t, we use the following formula

$$T = 23^\circ\mathrm{C} + \underbrace{\left(\frac{100\ ^\circ\mathrm{C} - 23^\circ\mathrm{C}}{T_\mathrm{t}(100\ ^\circ\mathrm{C}) - T_\mathrm{t}(23\ ^\circ\mathrm{C})}\right)}_{\text{calibration factor}} (T_\mathrm{t} - T_\mathrm{t}(23\ ^\circ\mathrm{C})) \tag{2.1}$$

where T and T_t are expressed in °C. It is easy to verify that $T = 23$ °C when $T_\mathrm{t} = T_\mathrm{t}(23\ ^\circ\mathrm{C})$, and $T = 100$ °C when $T_\mathrm{t} = T_\mathrm{t}(100\ ^\circ\mathrm{C})$. (The actual calibration was performed by Mr. Max Croci and the calibration factors were then kindly passed on to the author of this thesis.) In Fig. 2.3 we show some snapshots of the calibrated temperature measurements during the hot run at different heater powers. These data are used in Chapter 3 to build a reduced-order model of the slow time-scale base flow driven by natural convection.

The measurements of the six probe microphones are uncalibrated and expressed in Volts. In order to be useful for data processing, these measurements first need to be calibrated and then need to be converted to Pascal. To obtain V_calib (calibrated microphone measurement expressed in Volts) starting from V_uncalib (uncalibrated microphone measurement expressed in Volts) the following formula is used, as reported in the user manual of the microphones

$$V_\mathrm{calib} = 10^{-0.05\ cc} \cdot V_\mathrm{uncalib} \tag{2.2}$$

where cc is the calibration coefficient. The microphone manufacturer provides a calibration table in which the calibration coefficients depend on the frequency of the recorded signal. The values of the calibration coefficients we use are those at the excitation frequency, $f = 170$ Hz, and are reported in Table 2.1 together with the serial number of each microphone. The resulting calibrated measurement has units of Volts. Conversion to Pascal is achieved using the microphone sensitivity provided by the manufacturer and reported in Table 2.1. On top of this calibration, in order to reduce any remaining systematic error, each microphone is further calibrated against a reference microphone. This relative calibration procedure is explained in details in Sec. 4.4 when introducing the multi-microphone method. Finally, in order to

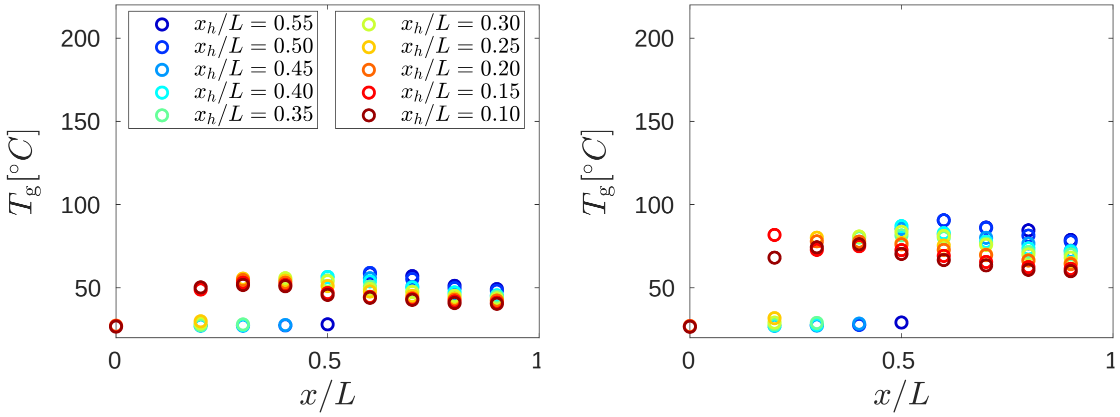

(a) $\dot{Q}_\mathrm{h} = 20$ W (b) $\dot{Q}_\mathrm{h} = 50$ W

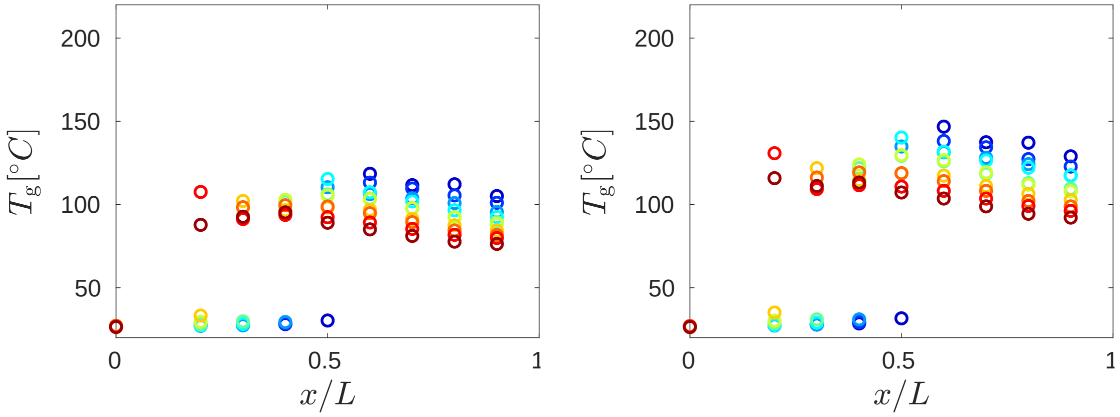

(c) $\dot{Q}_\mathrm{h} = 80$ W (d) $\dot{Q}_\mathrm{h} = 110$ W

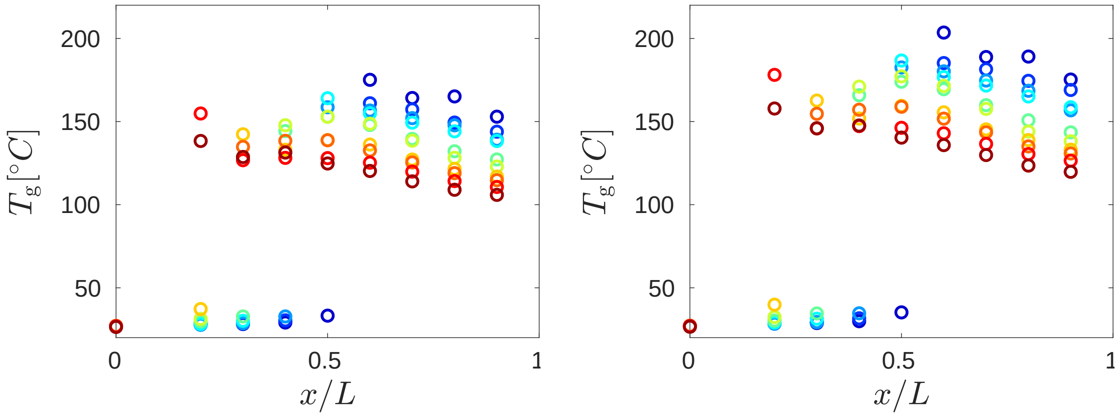

(e) $\dot{Q}_\mathrm{h} = 140$ W (f) $\dot{Q}_\mathrm{h} = 170$ W

Fig. 2.3 Measurements of the gas temperature at the tube centerline during the hot run. These snapshots refer to 35 seconds after the heater power reported in each figure caption is input. Different colours correspond to experiments performed on different days at different heater positions, as reported in the legend.

Table 2.1 Microphone specifications: serial number, calibration coefficient and sensitivity.

x_m/L	Serial number	Calibration coefficient	Sensitivity [V/Pa]
0.45	263704	0.030	$3.05 \cdot 10^{-3}$
0.55	263702	0.045	$2.80 \cdot 10^{-3}$
0.65	263703	-0.025	$3.02 \cdot 10^{-3}$
0.75	263707	0.015	$2.85 \cdot 10^{-3}$
0.85	263706	0.000	$2.95 \cdot 10^{-3}$
0.95	263705	-0.010	$2.99 \cdot 10^{-3}$

obtain the pressure oscillations from the calibrated pressure signal expressed in Pascal, we simply subtract from the pressure signal its mean value.

The acoustic pings provided by the loudspeaker located at the base of the tube are simultaneously recorded by the six microphones. Fig. 2.4a shows a typical ping and its successive natural decay. From this ping we want to extract the following information: the decay rate and frequency of the oscillations during the decay, and the corresponding values of the complex pressure for each microphone. To do this, for each microphone and for each acoustic ping the following steps are performed: (i) a Butterworth filter, centred at the excitation frequency (170 Hz) and with size ±25 Hz, is applied in order to filter out any undesired frequencies; (ii) a fast Fourier transform is applied only to the decaying part of the signal, with the aim to determine the complex pressure value (peak in the frequency spectrum) and the frequency of oscillations (frequency at which the peak occurs); (iii) a Hilbert transform is applied to the full pressure signal in order to obtain the signal amplitude and phase as functions of time; (iv) the logarithm function is applied to the signal amplitude; (v) a straight line is fitted to the decaying part of the signal. The best-fit line is obtained by weighted least squares regression using an exponentionally decaying function so that the low-amplitude signal, characterised by a lower signal-to-noise ratio, is weighted less. This procedure (except for step (ii)) can be visualized in Fig. 2.4b. The slope of the straight line corresponds to the decay rate, whereas the frequency of the oscillations is obtained from the fast Fourier transform. (The frequency of the oscillations can also be computed by averaging the instantaneous phase resulting from the Hilbert transform in the region where the decay occurs). Both the Hilbert and the fast Fourier transforms are Matlab® inbuilt functions. To provide a more robust estimate of the decay rate and frequency, the values obtained from the six microphones are averaged, although no significant scatter exists between them (see caption of Fig. 2.4 as an example). The averaged decay rate and frequency represent the real and imaginary parts of the experimental complex frequency s_{exp}, respectively. At the end of this process, we therefore obtain an accurate estimate of the average experimental complex frequency as well as the complex pressure value for each microphone during the decay. The magnitude of the complex pressure values gives rise to the pressure eigenmode (an example is shown in the inset figure of Fig. 2.4a). The complex pressure values are used within the multi-microphone method to compute the downstream reflection coefficient, as explained in Sec. 4.4. A Matlab® script to compute complex frequency and pressures from the experiments is reported in Appendix A.

The value of decay rates and frequencies for the empty tube case (each one averaged over the 100 acoustic pings obtained on each day) are shown in Fig. 2.5a (red circles). When the heater is placed inside the tube but switched off, additional drag is introduced into the system, which results in larger decay rates (black circles in Fig. 2.5a). The decay rates become even larger when both the heater and the thermocouples are placed inside the tube (Fig. 2.5b). These effects are modeled separately in Chapter 4.

In Fig. 2.6 we show the entire set of experimental complex frequencies when the heater is switched on and the thermocouples are in place. The frequency increases as the heater power increases because the air above the heater becomes hotter and has a higher sound speed. As the heater moves towards the bottom of the tube, the slope of Fig. 2.6b increases because the column of hot air is longer. The physical mechanism described in the final paragraph of Sec. 1.1 straightforwardly explains most of the observations: (i) when the heater is in the bottom half of the tube ($x_{\mathrm{h}}/L = [0.10, 0.15, 0.20, 0.25, 0.30, 0.40, 0.45]$), the growth rate becomes less negative as the heater power increases; (ii) the least stable condition occurs when the heater is placed near $x_{\mathrm{h}}/L = 0.25$, in agreement with Saito [52]; (iii) the most stable condition examined here occurs when the heater is in the top half of the tube ($x_{\mathrm{h}}/L = 0.55$). Two heater positions ($x_{\mathrm{h}}/L = [0.45, 0.50]$) deserve further comment because they reveal the position of the velocity node in the experiments. We expect the velocity node to move upstream as the heater power increases, due to the increasing difference in speeds of sound above (hot) and below (cold) the heater. When the heater is placed in the middle of the tube ($x_{\mathrm{h}}/L = 0.50$), it is always downstream of the velocity node so the thermoacoustic mechanism is always stabilizing and the growth rate becomes more negative as the heater power increases. When the heater is placed at $x_{\mathrm{h}}/L = 0.45$ the growth rate becomes less negative at low heater powers but more negative at high heater powers. This shows that, for this heater position, the velocity node passes through the heater (in the upstream direction) as the heater power increases. This is a key experimental configuration because it presents a particularly challenging test of the accuracy of the thermoacoustic models analyzed in this thesis.

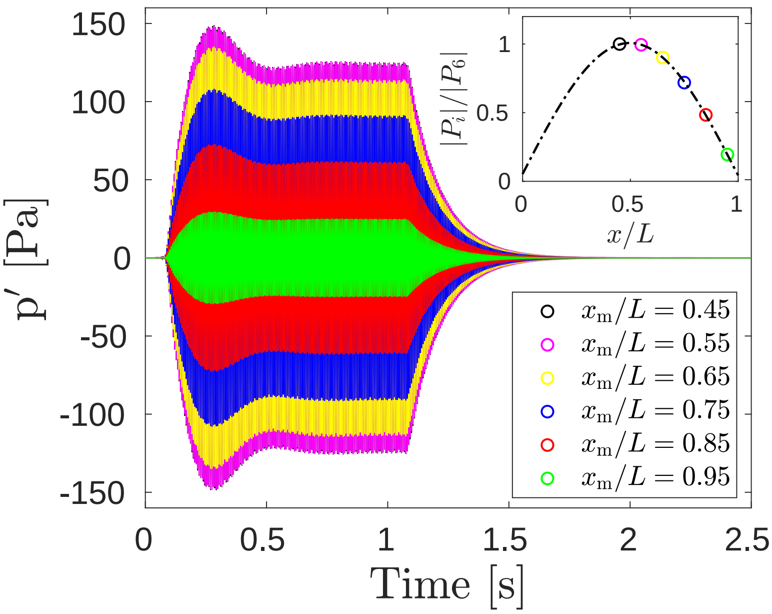

(a) Raw signals

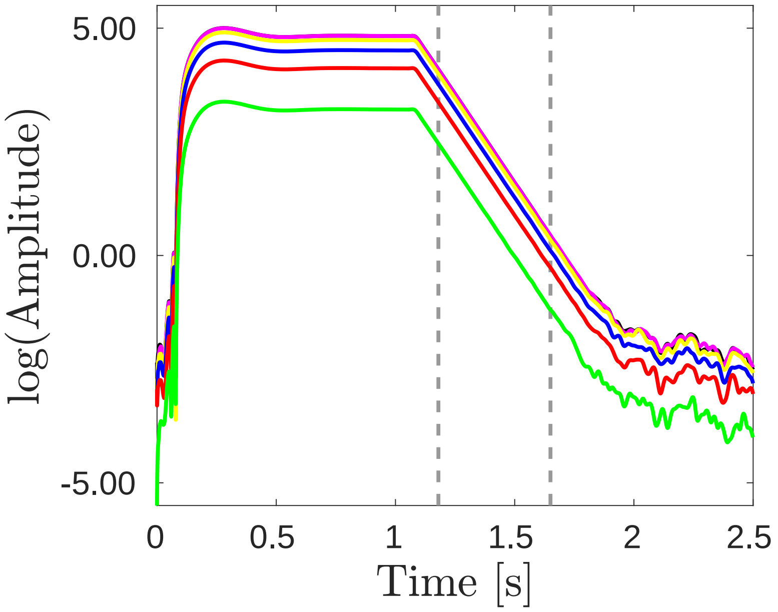

(b) Filtered and Hilbert-transformed signals

Fig. 2.4 (a) Raw pressure oscillations recorded by the six microphones after sinusoidal forcing at 170 Hz. The inset figure in (a) shows the corresponding pressure eigenmode. (b) Logarithm of the amplitude of the filtered and Hilbert-transformed oscillations. The two vertical dashed lines in (b) identify the exponential decay. Microphones at $x_\mathrm{m}/L = [0.45, 0.55, 0.65, 0.75, 0.85, 0.95]$ provide the following decay rates: $[-7.775, -7.775, -7.774, -7.775, -7.770, -7.764]$ rad $\cdot$ s^{-1}, respectively, and the same frequency: 168.46 Hz. This results in the average experimental complex frequency $s_\mathrm{exp} = -7.772\,\mathrm{rad}\cdot\mathrm{s}^{-1} + \mathrm{i}\,168.46$ Hz.

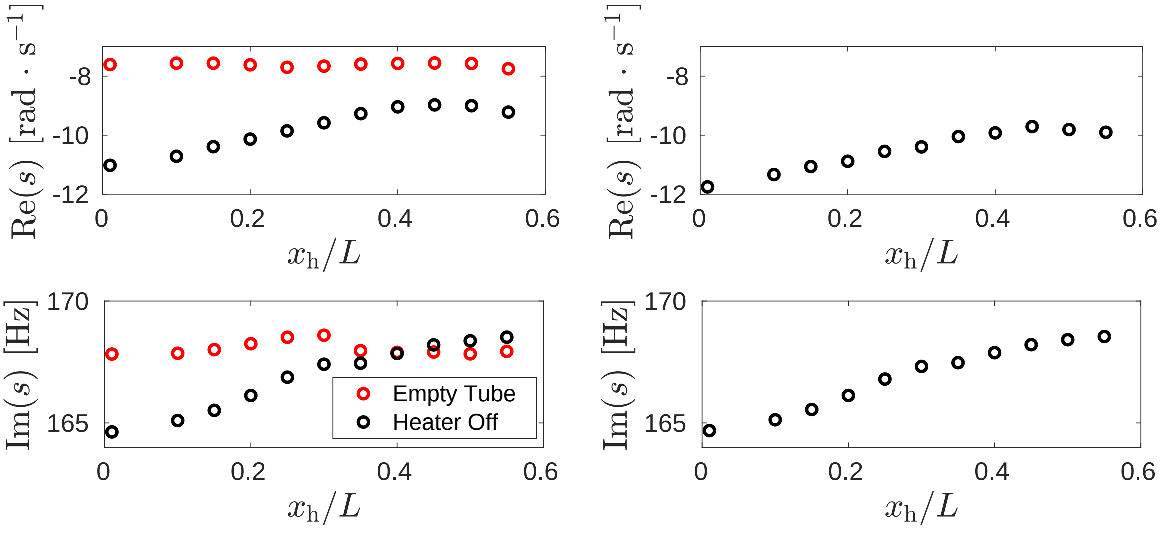

(a) Heater switched off

(b) Heater switched off and thermocouples

Fig. 2.5 Experimental observations of decay rate (top) and frequency (bottom) of acoustic oscillations when the heater is switched off and placed at different locations (a) without the thermocouples being inside the tube (black circles), and (b) with the thermocouples being inside the tube. The experimental complex frequencies in the empty tube case (red circles) are added to (a) to show the effect of the drag due to the heater.

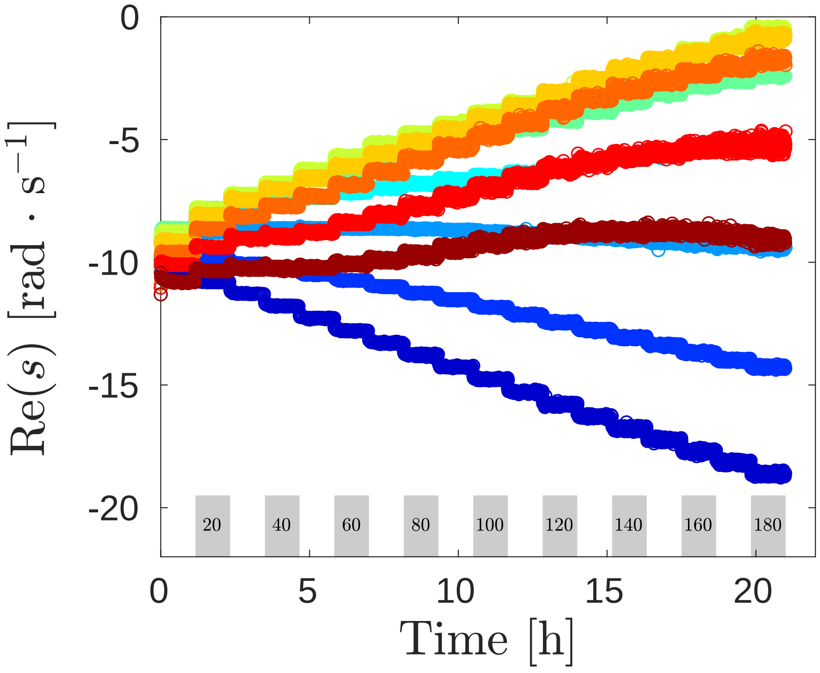

(a) Decay rate

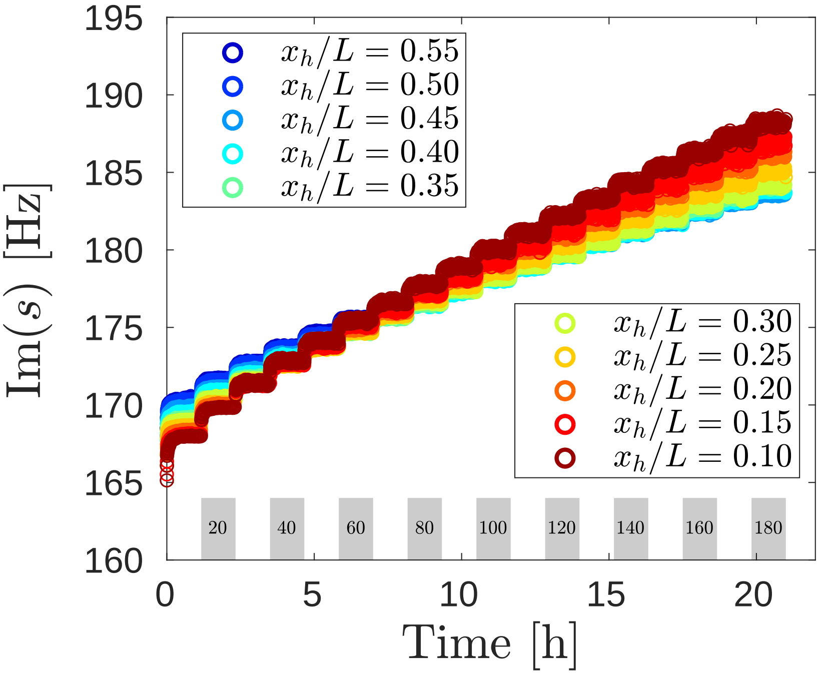

(b) Frequency

Fig. 2.6 Experimental observations of decay rate (a) and frequency (b) of thermoacoustic oscillations when the heater is switched on and the thermocouples are in place, as function of time and heater position. The heater power increases every 70 minutes in steps of 10 W (shown by bars at the bottom).

Chapter 3

Slow time-scale modeling

In this chapter we describe the heat transfer model used to predict at every instant in time the gas temperature profile inside the Rijke tube as well as the inlet bulk speed of the gas. We also provide details regarding its numerical implementation. We then discuss how the experiments obtained in the presence of the heater switched on are assimilated into the heat transfer model using the ensemble Kalman filter (EnKF) in order to infer the unknown model parameters and improve the state estimates. Finally, we show the results obtained from this analysis and explain how these are used to build the acoustic and thermoacoustic models presented in the next chapters.

3.1 Model

We consider a small element of tube of length δx, internal diameter D, and thickness r (see Fig. 3.1). The energy balance in the solid reads

$$(\rho_\mathrm{s} A_\mathrm{s} \delta x) c_\mathrm{s} \frac{\partial T_\mathrm{s}}{\partial t} = -\frac{\partial \dot{Q}_\mathrm{s}}{\partial x} \delta x - \dot{Q}_\mathrm{o} + \dot{Q}_\mathrm{i} \tag{3.1}$$

where $A_s = \frac{\pi}{4}[(D+2r)^2 - D^2] = \pi r(D+r)$. By assuming that the diffusive heat transfer is $\dot{Q}_\mathrm{s} = -\lambda_\mathrm{s} \frac{\partial T_\mathrm{s}}{\partial x}$, and that $\dot{Q}_\mathrm{o}$ and $\dot{Q}_\mathrm{i}$ can be modelled with convective heat transfer coefficients h_o and h_i, respectively, and by further assuming constant thermal conductivity λ_s, Eq. (3.1) can be re-written as

$$\rho_\mathrm{s} A_\mathrm{s} c_\mathrm{s} \frac{\partial T_\mathrm{s}}{\partial t} = \lambda_\mathrm{s} A_\mathrm{s} \frac{\partial^2 T_\mathrm{s}}{\partial x^2} - h_\mathrm{o} \pi_\mathrm{o} (T_\mathrm{s} - T_\mathrm{a}) + h_\mathrm{i} \pi_\mathrm{i} (T_\mathrm{g} - T_\mathrm{s}) \tag{3.2}$$

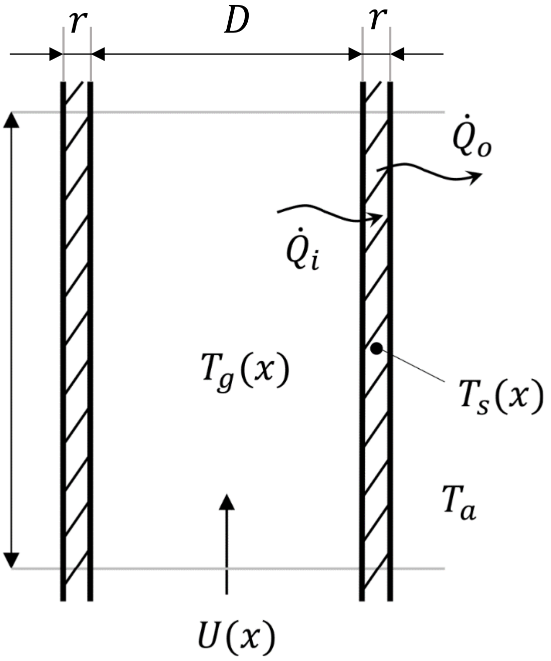

Fig. 3.1 Sketch of a small element of tube of length δx, internal diameter D, thickness r, with gas speed $U(x)$, gas temperature $T_\mathrm{g}(x)$, solid temperature $T_\mathrm{s}(x)$, ambient temperature T_a, and inner and outer heat flow rates $\dot{Q}_\mathrm{i}$ and $\dot{Q}_\mathrm{o}$, respectively.

where $\pi_\mathrm{i} = \pi D$ and $\pi_\mathrm{o} = \pi(D+2r)$. By re-arranging and replacing the convective heat transfer coefficients with Nusselt numbers, one obtains

$$\frac{\partial T_\mathrm{s}}{\partial t} = \frac{\lambda_\mathrm{s}}{\rho_\mathrm{s} c_\mathrm{s}} \frac{\partial^2 T_\mathrm{s}}{\partial x^2} - \mathrm{Nu}_\mathrm{o} \frac{\lambda_\mathrm{a}}{\rho_\mathrm{s} c_\mathrm{s}} \frac{\pi_\mathrm{o}}{A_\mathrm{s}\, L} (T_\mathrm{s} - T_\mathrm{a}) + \mathrm{Nu}_\mathrm{i} \frac{\lambda_\mathrm{g}}{\rho_\mathrm{s} c_\mathrm{s}} \frac{\pi_\mathrm{i}}{A_\mathrm{s}\, D} (T_\mathrm{g} - T_\mathrm{s}) \tag{3.3}$$

The same procedure can be applied to a control volume containing gas moving at local speed U, thus giving

$$(\rho_\mathrm{g} A_\mathrm{g} \delta x) c_{\mathrm{p,g}} \left(\frac{\partial T_\mathrm{g}}{\partial t} + U \frac{\partial T_\mathrm{g}}{\partial x} \right) = -\frac{\partial \dot{Q}_\mathrm{g}}{\partial x} \delta x - \dot{Q}_\mathrm{i} + \tilde{\dot{Q}}_\mathrm{h} \delta x \tag{3.4}$$

where $A_\mathrm{g} = \pi D^2/4$. In Eq. (3.4), the source term $\tilde{\dot{Q}}_\mathrm{h}$ represents the thermal power per unit length provided by the electric heater. The inlet gas quantities $(\cdot)_1$ are assumed to be ambient $(\cdot)_\mathrm{a}$. One can now apply the ideal gas law, as well as Fourier's law, and use mass conservation in its integral form $\left(\frac{\partial(\rho AU)}{\partial x} = 0\right)$ to obtain

$$\rho_1 A_\mathrm{g} c_{\mathrm{p,g}} \frac{T_1}{T_\mathrm{g}} \frac{\partial T_\mathrm{g}}{\partial t} + \rho_1 A_\mathrm{g} c_{\mathrm{p,g}} U_1 \frac{\partial T_\mathrm{g}}{\partial x} = \lambda_\mathrm{g} A_\mathrm{g} \frac{\partial^2 T_\mathrm{g}}{\partial x^2} - \mathrm{Nu}_\mathrm{i} \lambda_\mathrm{g} \frac{\pi_\mathrm{i}}{D} (T_\mathrm{g} - T_\mathrm{s}) + \tilde{\dot{Q}}_\mathrm{h} \tag{3.5}$$

The gas thermal conductivity is assumed to be equal to that of air at ambient conditions, i.e. $\lambda_\mathrm{g} = \lambda_\mathrm{a} = \lambda_1$. Radiation is not modelled.

We also solve the integral momentum equation, in which we assume that (i) the unsteady term is negligible, i.e. the inertia forces are negligible compared to the buoyancy and drag forces, and (ii) the total pressure losses Δp are concentrated at the heater location, and modelled through an inviscid pressure loss coefficient k_i, such that $\Delta p = k_\mathrm{i}(\rho_\mathrm{h} U_\mathrm{h}^2)/2$. The integral momentum equation is

$$\rho_2 U_2^2 - \rho_1 U_1^2 + k_\mathrm{i} \frac{\rho_\mathrm{h} U_\mathrm{h}^2}{2} = \int_0^L (\rho_1 - \rho_\mathrm{g}) g \, \mathrm{d}x \tag{3.6}$$

By doing so we neglect the presence of viscous losses, which would require the introduction of a fourth model parameter and would not change the results significantly. By using mass conservation and the ideal gas law, Eq. (3.6) can be re-arranged to

$$U_1^2 \left[\frac{k_\mathrm{i}}{2} \left(\frac{A_1}{A_\mathrm{h}} \right)^2 \frac{T_\mathrm{h}}{T_1} + \left(\frac{A_1}{A_2} \right)^2 \frac{T_2}{T_1} - 1 \right] = \int_0^L \frac{(\rho_1 - \rho_\mathrm{g})}{\rho_1} g \, \mathrm{d}x \tag{3.7}$$

In our case $A_1 = A_2 = A_\mathrm{h}$, but in general these areas could be different.

We non-dimensionalize Eqs. (3.3), (3.5) and (3.7) with the reference scales $\{L,\ g,\ T_1\}$, which naturally give a time scale $(L/g)^{1/2}$, and a velocity scale $(gL)^{1/2}$. Temperatures are measured relative to T_1 and then divided by T_1. For example, T becomes $\Theta^* = \frac{T - T_1}{T_1}$. Non-dimensional quantities are denoted by $(\cdot)^*$ to distinguish them from the corresponding dimensional quantities. The energy equation for the solid becomes

$$\frac{T_1}{(L/g)^{1/2}} \frac{\partial \Theta_\mathrm{s}^*}{\partial t^*} = \frac{\lambda_\mathrm{s}}{\rho_\mathrm{s} c_\mathrm{s}} \frac{T_1}{L^2} \frac{\partial^2 \Theta_\mathrm{s}^*}{\partial x^{*2}} - \mathrm{Nu}_\mathrm{o} \frac{\lambda_\mathrm{a}}{\rho_\mathrm{s} c_\mathrm{s}} \frac{\pi_\mathrm{o}}{A_\mathrm{s}\, L} T_1 \Theta_\mathrm{s}^* + \mathrm{Nu}_\mathrm{i} \frac{\lambda_\mathrm{a}}{\rho_\mathrm{s} c_\mathrm{s}} \frac{\pi_\mathrm{i}}{A_\mathrm{s}\, D} T_1 (\Theta_\mathrm{g}^* - \Theta_\mathrm{s}^*) \tag{3.8}$$

We define the following non-dimensional parameters

$$\eta_1^* = \frac{1}{L(gL)^{1/2}} \frac{\lambda_\mathrm{s}}{\rho_\mathrm{s} c_\mathrm{s}} \tag{3.9}$$

$$\eta_2^* = \frac{\pi_\mathrm{o}}{A_\mathrm{s}(gL)^{1/2}} \frac{\lambda_\mathrm{a}}{\rho_\mathrm{s} c_\mathrm{s}} \tag{3.10}$$

$$\eta_3^* = \frac{\pi_\mathrm{i}}{A_\mathrm{s}(gL)^{1/2}} \frac{L}{D} \frac{\lambda_\mathrm{a}}{\rho_\mathrm{s} c_\mathrm{s}} \tag{3.11}$$

and re-write Eq. (3.8) compactly as

$$\frac{\partial \Theta_{\mathrm{s}}^*}{\partial t^*} = \eta_1^* \frac{\partial^2 \Theta_{\mathrm{s}}^*}{\partial x^{*2}} - \mathrm{Nu_o}\,\eta_2^* \Theta_{\mathrm{s}}^* + \mathrm{Nu_i}\,\eta_3^* (\Theta_{\mathrm{g}}^* - \Theta_{\mathrm{s}}^*) \tag{3.12}$$

The energy equation for the gas becomes

$$\begin{aligned} \rho_{\mathrm{a}} A_{\mathrm{g}} c_{\mathrm{p,g}} \frac{T_1}{(L/g)^{1/2}} \frac{1}{(\Theta_{\mathrm{g}}^* + 1)} \frac{\partial \Theta_{\mathrm{g}}^*}{\partial t^*} + \rho_{\mathrm{a}} A_{\mathrm{g}} c_{\mathrm{p,g}} \frac{T_1}{(L/g)^{1/2}} U_1^* \frac{\partial \Theta_{\mathrm{g}}^*}{\partial x^*} = \\ \lambda_{\mathrm{a}} A_{\mathrm{g}} \frac{T_1}{L^2} \frac{\partial^2 \Theta_{\mathrm{g}}^*}{\partial x^{*2}} - \mathrm{Nu_i} \lambda_{\mathrm{a}} \frac{\pi_{\mathrm{i}}}{D} T_1 (\Theta_{\mathrm{g}}^* - \Theta_{\mathrm{s}}^*) + \tilde{\dot{Q}}_{\mathrm{h}} \end{aligned} \tag{3.13}$$

We define the following non-dimensional parameters

$$\eta_4^* = \frac{1}{L(gL)^{1/2}} \frac{\lambda_{\mathrm{a}}}{\rho_{\mathrm{a}} c_{\mathrm{p,g}}} \tag{3.14}$$

$$\eta_5^* = \frac{\pi_{\mathrm{i}}}{A_{\mathrm{g}}(gL)^{1/2}} \frac{L}{D} \frac{\lambda_{\mathrm{a}}}{\rho_{\mathrm{a}} c_{\mathrm{p,g}}} \tag{3.15}$$

$$\dot{Q}_{\mathrm{h}}^* = \frac{(L/g)^{1/2}}{T_1} \frac{\tilde{\dot{Q}}_{\mathrm{h}}}{\rho_{\mathrm{a}} A_{\mathrm{g}} c_{\mathrm{p,g}}} \tag{3.16}$$

and re-write Eq. (3.13) compactly as

$$\frac{1}{(\Theta_{\mathrm{g}}^* + 1)} \frac{\partial \Theta_{\mathrm{g}}^*}{\partial t^*} + U_1^* \frac{\partial \Theta_{\mathrm{g}}^*}{\partial x^*} = \eta_4^* \frac{\partial^2 \Theta_{\mathrm{g}}^*}{\partial x^{*2}} - \mathrm{Nu_i}\,\eta_5^* (\Theta_{\mathrm{g}}^* - \Theta_{\mathrm{s}}^*) + \dot{Q}_{\mathrm{h}}^* \tag{3.17}$$

The integral momentum equation becomes

$$\int_0^1 \frac{\Theta_{\mathrm{g}}^*}{\Theta_{\mathrm{g}}^* + 1} \mathrm{d}x^* = U_1^{*2} \left[\frac{k_{\mathrm{i}}}{2} \left(\frac{A_1}{A_{\mathrm{h}}} \right)^2 (\Theta_{\mathrm{h}}^* + 1) + \left(\frac{A_1}{A_2} \right)^2 (\Theta_2^* + 1) - 1 \right] \tag{3.18}$$

3.1.1 Summary of the non-dimensional model

The model consists of two energy equations, one for the solid and one for the gas, and the integral momentum equation. Upon non-dimensionalization, these can be written as follows

$$\frac{\partial \Theta_{\mathrm{s}}^*}{\partial t^*} = \eta_1^* \frac{\partial^2 \Theta_{\mathrm{s}}^*}{\partial x^{*2}} - \mathrm{Nu_o}\,\eta_2^* \Theta_{\mathrm{s}}^* + \mathrm{Nu_i}\,\eta_3^* (\Theta_{\mathrm{g}}^* - \Theta_{\mathrm{s}}^*) \tag{3.19}$$

$$\frac{1}{(\Theta_{\mathrm{g}}^* + 1)} \frac{\partial \Theta_{\mathrm{g}}^*}{\partial t^*} + U_1^* \frac{\partial \Theta_{\mathrm{g}}^*}{\partial x^*} = \eta_4^* \frac{\partial^2 \Theta_{\mathrm{g}}^*}{\partial x^{*2}} - \mathrm{Nu_i}\,\eta_5^* (\Theta_{\mathrm{g}}^* - \Theta_{\mathrm{s}}^*) + \dot{Q}_{\mathrm{h}}^* \tag{3.20}$$

$$\int_0^1 \frac{\Theta_\mathrm{g}^*}{\Theta_\mathrm{g}^*+1}\mathrm{d}x^* = U_1^{*2}\left[\frac{k_\mathrm{i}}{2}\left(\frac{A_1}{A_\mathrm{h}}\right)^2(\Theta_\mathrm{h}^*+1)+\left(\frac{A_1}{A_2}\right)^2(\Theta_2^*+1)-1\right] \tag{3.21}$$

The implementation of this model is reported in Appendix B, along with the values of the constants used.

3.2 Numerical implementation

In the derived model, the five coefficients η^* and $\dot{Q}_\mathrm{h}^*$ are known. On the other hand, the three model parameters, namely Nu_o, Nu_i and k_i, are unknown quantities whose value is updated in a probabilistic fashion using the ensemble Kalman filter in the way explained in Sec. 3.3. For now we suppose their value to be known.

The derived model consists of two coupled PDEs, namely Eqs. (3.19) and (3.20), which can be simultaneously solved once the non-dimensional inlet bulk speed, U_1^*, is known. From a physical point of view, this is a typical conjugate heat transfer problem, i.e. a problem where knowledge of the heat transfer to one phase (e.g. solid) is necessary to get information about the heat transfer to another phase (e.g. fluid), and vice versa. The non-dimensional inlet bulk speed can be derived using Eq. (3.21), which in turn requires knowledge of the gas temperature profile, Θ_g^*. This couples the three equations. The numerical steps to solve these equations are: (i) define the initial temperature profiles, Θ_g^* and Θ_s^*; (ii) approximate numerically the left-hand side of Eq. (3.21) and solve for U_1^*, algebraically; (iii) using the value of U_1^* computed at step (ii) and using a suitable numerical method, solve for Θ_g^* and Θ_s^*; (iv) iteratively repeat the above steps replacing the temperature profiles at step (i) with the values computed at step (iii).

The two one-dimensional energy equations are discretized on a grid of 101 points using the Finite-Difference method [83]. Because the Rijke tube used in this study has a length $L = 1$ m, this corresponds to placing a numerical grid point every centimeter between inlet and outlet. The Finite-Difference method relies on replacing exact derivatives of a certain function with finite differences of the same function at discrete locations or, in other words, with a linear combination of the function evaluated at different grid points. In particular, the approximation of the n-th-order derivative of a function ϕ with respect to the space coordinate x on a uniform grid with spacing h is given by

$$\left.\frac{\delta^n \phi}{\delta x^n}\right|_i = \frac{1}{h^n}\sum_{j=l}^{r}\omega_j\phi_{i+j} \tag{3.22}$$

where $l(\leq 0)$ and $r(\geq 0)$ define the stencil. The general approach to derive the stencil moments ω_j is to first expand each ϕ_{i+j} about ϕ_i using Taylor series, and then derive conditions that guarantee that the only non-zero term on the right-hand side of Eq. (3.22) is the one that multiplies $\frac{d^n\phi}{dx^n}$. More details are provided in [84, 85]. An intrinsic relationship between the stencil and the order of accuracy p of the n-th-order approximation exists. This can be summarised as follows

$$\begin{aligned}
\text{Arbitrary stencil:}\quad & p = r - l + 1 - n \\
\text{Centred stencil, } n \text{ odd:}\quad & p = (2r+1) - n, \quad \omega_j = -\omega_{-j}, \quad \omega_0 = 0 \\
\text{Centred stencil, } n \text{ even:}\quad & p = 2(r+1) - n, \quad \omega_j = \omega_{-j}, \quad \omega_0 \neq 0
\end{aligned}$$

Using centred stencils ($r = -l$) is particularly convenient because, among other things, they always guarantee an extra order of accuracy for approximations of even-order derivatives, compared to biased stencils that employ the same number of stencil weights [84].

In addition to accuracy, one should also take into account the stability of a particular approximation. Indeed, for given approximations of derivatives, and for given governing equations, there typically exists a critical timestep above which numerical instabilities occur. In simple cases, the critical timestep can be derived analytically using techniques such as Von Neumann Stability Analysis or Modified Equation Analysis. However, because of the presence of a source term in our governing equations, the analytical approach is not feasible. The simplest approach to use is a trial-and-error approach, where the timestep is iteratively chosen such that instabilities do not occur. Among all the timesteps that fulfill the stability criterion, we want to use a sufficiently large one to run the simulations as quickly as possible.

In the present study, fourth-order accurate centred approximations are used for both first- and second-order spatial derivatives. Fourth-order accurate biased approximations are used near the boundaries. The corresponding stencil moments are tabulated in [84]. For the sake of simplicity, zero temperature gradients are used at the inlet and outlet boundaries in both Eqs. (3.19) and (3.20). This turns out to be a reasonable assumption, provided that the grid is fine enough, as in our case. The second-order accurate midpoint rule is used for the integral in Eq. (3.21). To ease the implementation, differentiation matrices are used for spatial discretization. The time integration method is the explicit fourth-order accurate Runge-Kutta, known as RK4. This guarantees higher accuracy and allows for larger timesteps, if compared to the common (explicit) first-order accurate Euler method.

The source term in Eq. (3.20), $\dot{Q}_{\mathrm{h}}^{*}$, is modelled with a Gaussian distribution centred at the heater location, with variance set arbitrarily to 0.0005 m^2, normalized such that its integral equals the input power. Choosing a smaller variance would require a finer grid and this would make the equations computationally more expensive to solve. Fig. 3.2 shows the shape of this

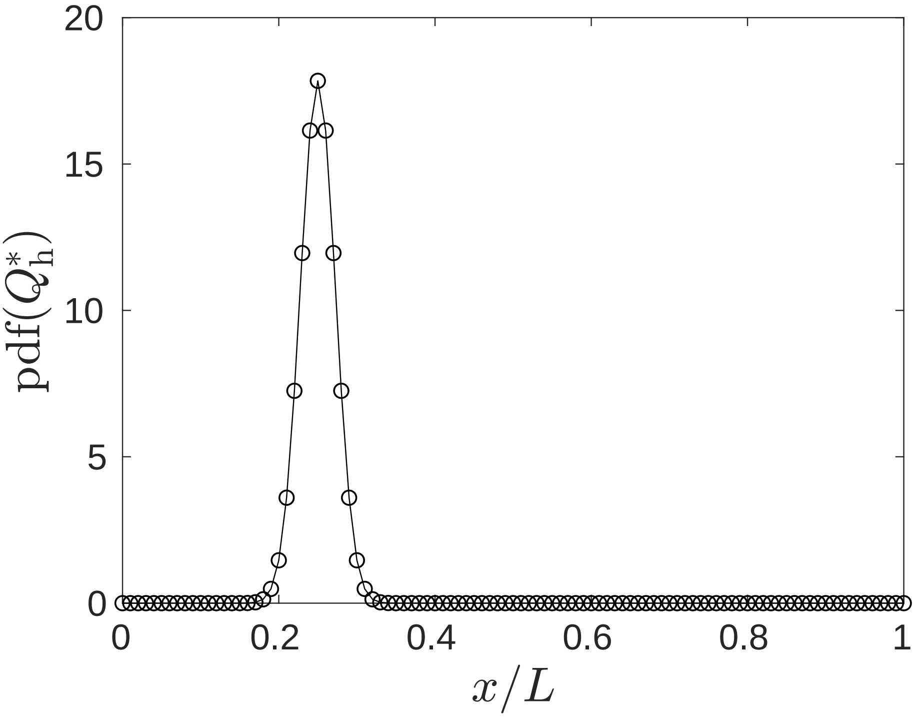

Fig. 3.2 Probability density function of the heater power, $\dot{Q}_\mathrm{h}^*$, when the heater is located at $x_\mathrm{h}/L = 0.25$. $\dot{Q}_\mathrm{h}^*$ is modelled with a Gaussian distribution centred at the heater location, with variance set arbitrarily to 0.0005 m^2. In this figure the distribution is normalized so that its integral equals 1.

distribution when $x_\mathrm{h}/L = 0.25$. When the heater approaches the bottom end ($x_\mathrm{h}/L = 0$), the slow time-scale model breaks down due to numerical instabilities that arise because the zero temperature gradient boundary condition conflicts with a non-zero value of the heat source probability density function at the same location. This is why the lowest heater position we investigate when the heater is switched on is $x_\mathrm{h}/L = 0.10$.

3.3 Data Assimilation

To integrate Eqs. (3.19) to (3.21) forward in time, we need to know the three model parameters: inner Nusselt number, Nu_i, outer Nusselt number, Nu_o, and inviscid pressure loss coefficient at the heater location, k_i. To do so, first, we define the state vector, made up of the solid and gas temperatures at the discrete locations. For each ensemble member, we initialize the state vector with constant values corresponding to the ambient temperature. In the context of the ensemble Kalman filter, an ensemble member is a numerical simulation that represents a sample extracted from a certain probability density function. Second, we initialize the three model parameters. Although these parameters are unknown, the choice of their initial value does not significantly affect the results. For each ensemble member, the parameter vector, appended to the state vector, is initialized with values randomly drawn from the following uniform distributions

$$p\left(\begin{bmatrix}\mathrm{Nu_i}\\ \mathrm{Nu_o}\\ k_\mathrm{i}\end{bmatrix}\right)=\mathscr{U}\left(\begin{bmatrix}7\cdot(1\pm0.2)\\ 60\cdot(1\pm0.3)\\ 9.5\cdot(1\pm0.1)\end{bmatrix}\right) \tag{3.23}$$

Third, the above model is integrated in time. Every ensemble member evolves with a different set of model parameters. In general, the ensemble members can evolve with both different initial states and different initial parameters. In our case, however, the initial state is the same for all members. Fourth, state and parameters are updated using the EnKF every time the temperature measurements become available, i.e. every 7 seconds. The ensemble used in this study consists of 30 members. For the update (or analysis) step, by computing sample mean and covariance matrix of the ensemble, a Gaussian distribution is reconstructed, even though the real distribution is not necessarily Gaussian (this happens when the model is nonlinear, as in our case). This Gaussian is then combined with the likelihood function, which is also assumed to be Gaussian, centred around the experimental measurement and with standard deviation of 2 K. The combination of these two distributions results in the optimal distribution of state and parameters. The optimal distributions then become the new prior distributions to sample from for the model prediction step, and the process repeats. With this process, one is able to (i) infer the evolution of the model parameters with their uncertainties, and (ii) improve the estimate of the state, which becomes more robust by learning from the experimental measurements.

3.4 Results

Fig. 3.3 shows the evolution of the model parameters from low powers (10 W) to high powers (180 W), with 95% confidence intervals. If on the one hand the inviscid pressure loss coefficient (Fig. 3.3d) seems to reach a steady value close to 10 at high powers for all the heater positions, on the other hand the behaviour of the inner and outer Nusselt numbers (Figs. 3.3b and 3.3c) is much less regular and of difficult physical interpretation. This happens because in our model we assimilate only gas temperature measurements. In other words, the model does not have any information about the solid temperature at any location, hence the problem is not well posed because there are several combinations of $(\Theta_\mathrm{s}^*, \mathrm{Nu_i}, \mathrm{Nu_o})$ that guarantee the same heat loss from the inside of the tube to the outside. Thus, the results in terms of Nusselt numbers and solid temperature profiles are not reliable. If one tries to change the thermocouple placement so as to assimilate fewer gas temperature measurements and at least a couple of solid temperature measurements (downstream of the heater), the agreement between gas temperature measurements and assimilated gas temperature profiles becomes poorer because the model tries to find the best compromise given all the measurements (not only the gas temperature measurements). Because in this study we are ultimately interested in predicting the gas temperature profiles in the most accurate way possible, we decided to use all the thermocouples available to measure the gas temperature only. Given that we do not actually assimilate any solid temperature measurement, it would be reasonable to use a simplified model where only one Nusselt number is used to model the heat transfer from the inside of the tube directly to the surrounding air. In this study, this is not done because the results of this model, reported in Fig. 3.4, are already ~~very~~ good. Fig. 3.4 shows different time snapshots of the gas temperature profile inside the Rijke tube for all the heater positions and for different heater powers. Indeed, we can see that the agreement between model predictions and experimental data is ~~very~~ good, even though these snapshots refer to the ~~very~~ early stage of the transients (35 s after the heater power reported in each figure caption is input). This agreement improves as time progresses towards the steady state because more data are assimilated. For the three lower-most heater positions ($x_\mathrm{h}/L = [0.10, 0.15, 0.20]$), the ambient temperature measurement is also assimilated into the model to obtain more reliable estimates. It is important to highlight that when the heater is placed at the same location as that of a thermocouple, the temperature measurement of that thermocouple is discarded because it is too affected by radiation. A summary of the temperature measurements used for assimilation for each heater position is reported in Table 3.1. The inlet bulk speed is instead shown in Fig. 3.5. It is worth noting that the inlet bulk speed depends only on the gas temperature profile (see Eq. (3.21)). Thus, even if the solid temperature profiles and the Nusselt numbers predictions are not accurate, the inlet bulk speed computation is accurate because the ensemble-average gas temperature profiles agree well with the gas temperature measurements (Fig. 3.4). The ensemble-average gas temperature and inlet bulk speed predicted by the base flow model are then used as input quantities for the acoustics model. For simplicity, we do not propagate any uncertainty from the base flow model to the acoustic model.

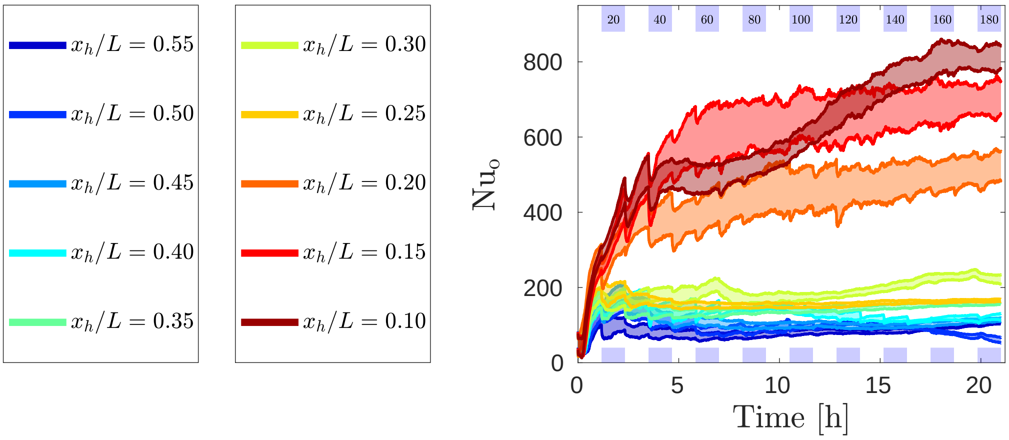

(a) Legend

(b) Outer Nusselt number

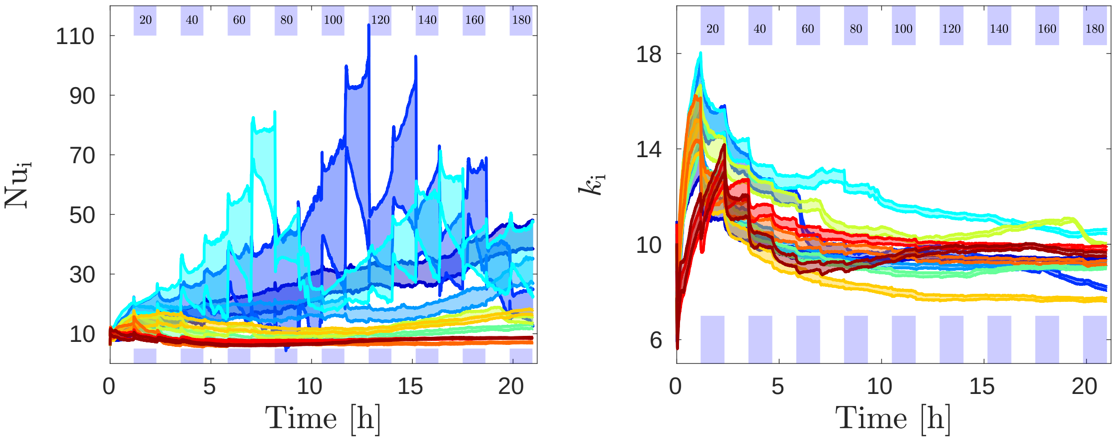

(c) Inner Nusselt number

(d) Inviscid pressure loss coefficient

Fig. 3.3 Slow time-scale model parameters with 95% confidence intervals as functions of time ([h], bottom axis) or heater power ([W], blue bars).

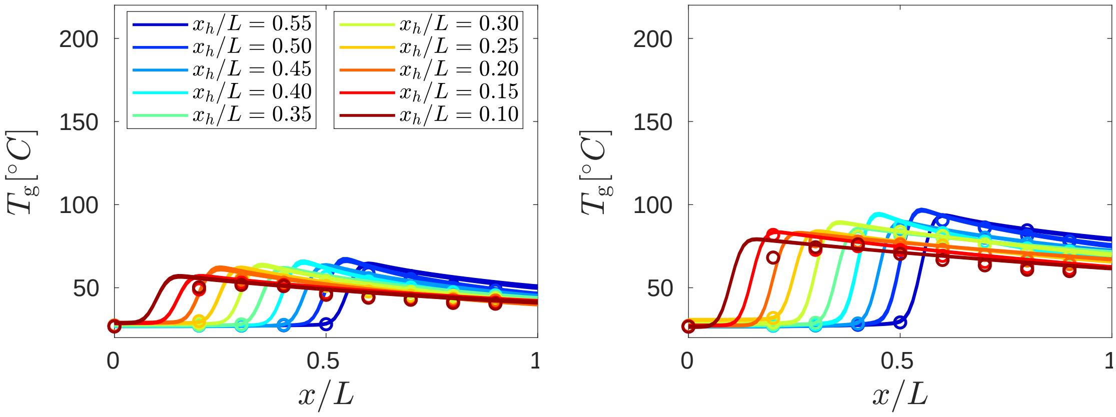

(a) $\dot{Q}_\mathrm{h} = 20$ W (b) $\dot{Q}_\mathrm{h} = 50$ W

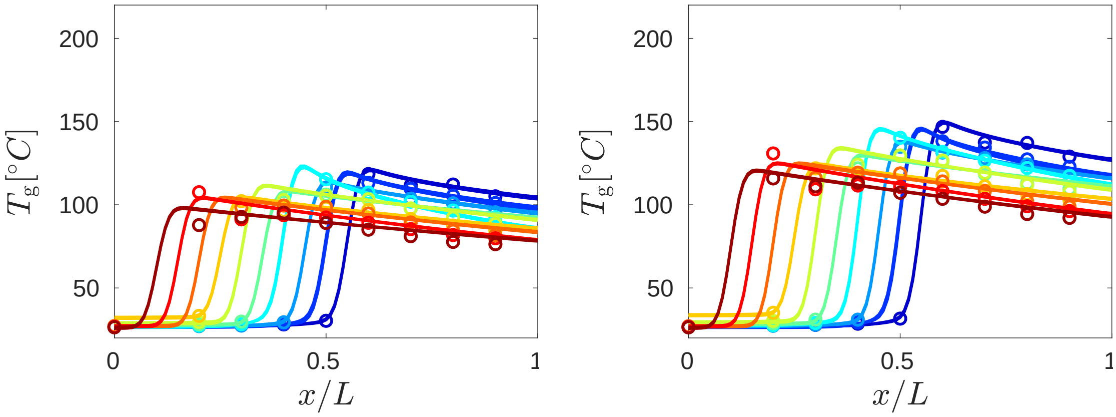

(c) $\dot{Q}_\mathrm{h} = 80$ W (d) $\dot{Q}_\mathrm{h} = 110$ W

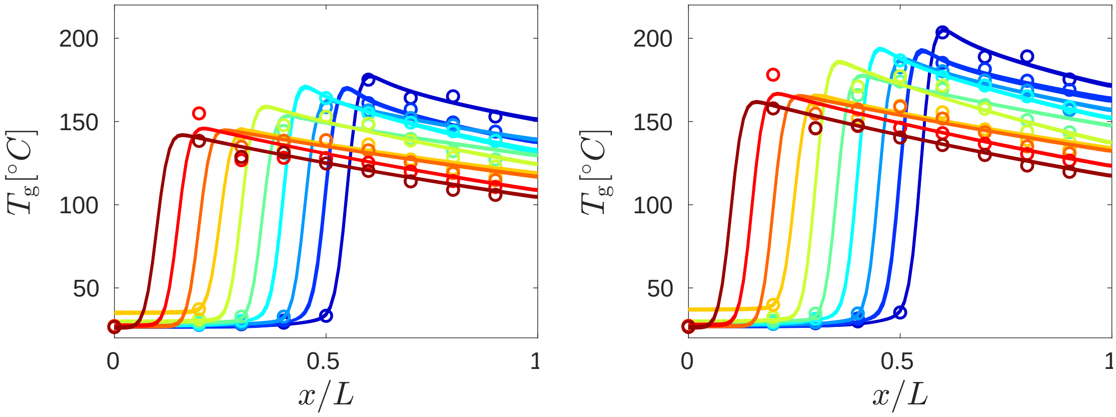

(e) $\dot{Q}_\mathrm{h} = 140$ W (f) $\dot{Q}_\mathrm{h} = 170$ W

Fig. 3.4 Comparison of gas temperature measurements at the tube centerline (circles) and model predictions with 95% confidence intervals (solid lines) during the hot run. These snapshots refer to 35 seconds after the heater power reported in each figure caption is input.

Table 3.1 Temperature measurements (identified by the thermocouple locations x_t/L) used for data assimilation into the slow time-scale model for each heater position x_h/L. Empty spaces represent data that are not used in the assimilation process.

x_h/L	x_t/L								
0.55		0.20	0.30	0.40	0.50	0.60	0.70	0.80	0.90
0.50		0.20	0.30	0.40		0.60	0.70	0.80	0.90
0.45		0.20	0.30	0.40	0.50	0.60	0.70	0.80	0.90
0.40		0.20	0.30		0.50	0.60	0.70	0.80	0.90
0.35		0.20	0.30	0.40	0.50	0.60	0.70	0.80	0.90
0.30		0.20		0.40	0.50	0.60	0.70	0.80	0.90
0.25		0.20	0.30	0.40	0.50	0.60	0.70	0.80	0.90
0.20	0.00		0.30	0.40	0.50	0.60	0.70	0.80	0.90
0.15	0.00	0.20	0.30	0.40	0.50	0.60	0.70	0.80	0.90
0.10	0.00	0.20	0.30	0.40	0.50	0.60	0.70	0.80	0.90

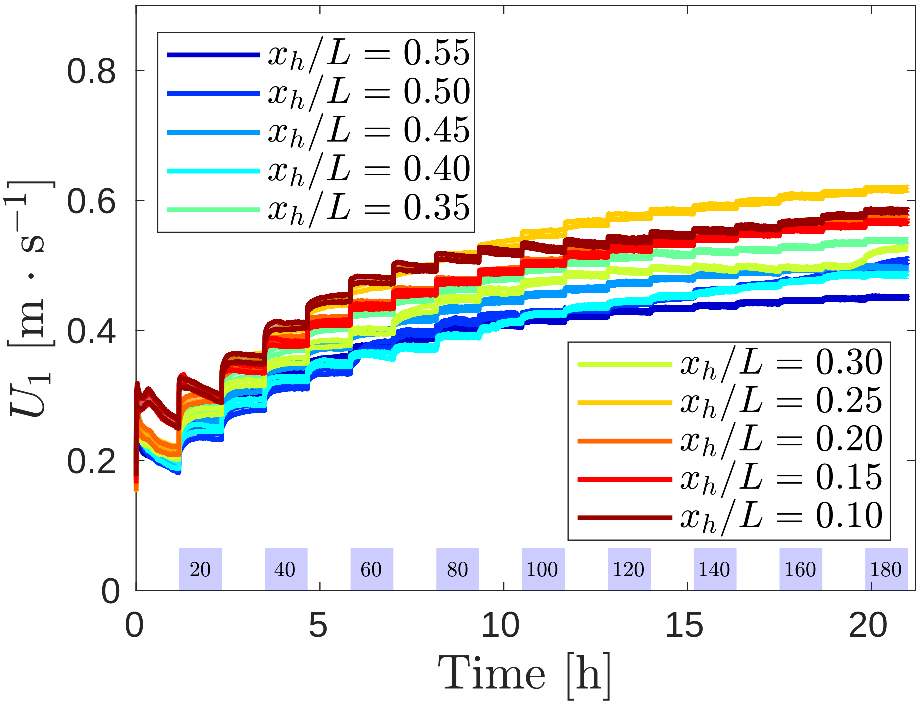

Fig. 3.5 Model predictions of inlet bulk speed with 95% confidence intervals for different heater positions as functions of time ([h], bottom axis) or heater power ([W], blue bars).

Chapter 4

Fast time-scale modelling without the thermoacoustic mechanism

This chapter is devoted to the modelling of the fast time scale in absence of any thermoacoustic effect. Starting from the results obtained in Chapter 3, we build an acoustic model able to make quantitatively-accurate predictions using a step-by-step procedure. First, we derive the governing equations for the empty tube and compute the corresponding reflection coefficient. Second, we model the behaviour of the heater and of the two rods that hold it in place (including the electricity wires) by introducing visco-thermal losses at the heater location and along the two rods (and wires). Third, we model the visco-thermal drag due to the presence of the thermocouples, which are assumed to be identical. Fourth, we provide details of how the multi-microphone method works. This method will be used in Chapter 5 to compute the downstream reflection coefficient, which changes when the thermoacoustic mechanism is accounted for.

4.1 Modelling the empty tube

We model the acoustic time scale inside the tube using a network model [86, 31] made up of 40 equally-spaced elements. Adjacent elements are connected by jump conditions that specify momentum and energy changes between two elements. A simplified sketch of a network model containing five acoustic elements is reported in Fig. 4.1. In our analysis we use a consistent number of elements because there is a temperature gradient inside the tube when the heater is switched on, which affects the tube acoustics, as highlighted by Li and Morgans [87]. Homogeneous properties are assumed inside each element. The set of governing equations in each element are the Navier-Stokes equations, which, in the

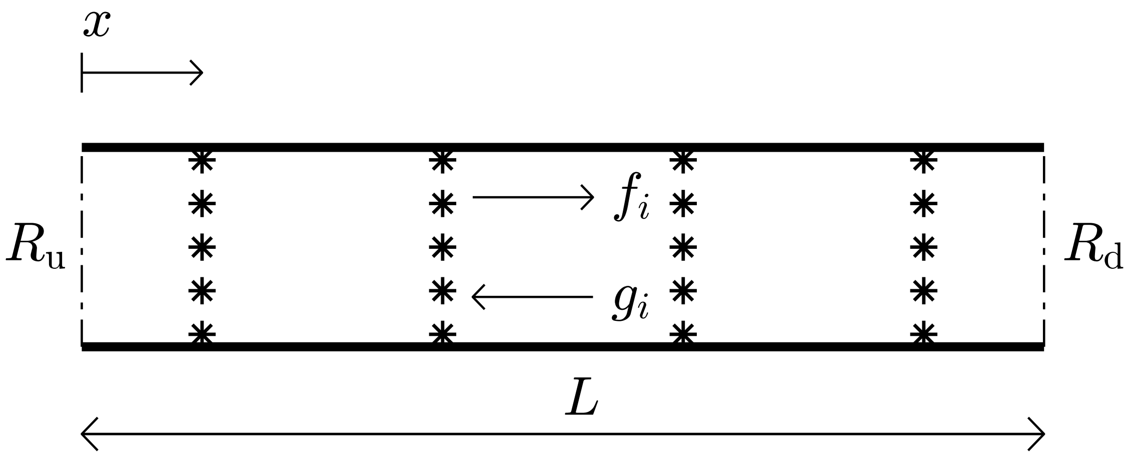

Fig. 4.1 Sketch of a simplified network model made up of five acoustic elements separated by four jump conditions. The forward and backward travelling waves in each acoustic element are denoted by f_i and g_i, respectively. R_{u} and R_{d} are the upstream and downstream reflection coefficients.

assumption of negligible viscosity and heat conduction, reduce to the Euler equations. Upon neglecting gravity and considering one dimensional flow, these equations are

$$\frac{\partial \rho}{\partial t}+u\frac{\partial \rho}{\partial x}+\rho\frac{\partial u}{\partial x}=0 \tag{4.1}$$

$$\rho\frac{\partial u}{\partial t}+\rho u\frac{\partial u}{\partial x}+\frac{\partial p}{\partial x}=0 \tag{4.2}$$

$$\frac{\partial p}{\partial t}+u\frac{\partial p}{\partial x}+\gamma p\frac{\partial u}{\partial x}=0 \tag{4.3}$$

Integrating Eqs. (4.1) to (4.3) across the boundary between two adjacent elements located at the generic axial coordinate $x=b$, and assuming no accumulation of mass, momentum and energy, lead to the following set of jump conditions

$$\left[\rho u\right]_{b^-}^{b^+}=0 \tag{4.4}$$

$$\left[p+\rho u^2\right]_{b^-}^{b^+}=0 \tag{4.5}$$

$$\left[\frac{\gamma}{\gamma-1}pu+\frac{1}{2}\rho u^3\right]_{b^-}^{b^+}=0 \tag{4.6}$$

We now write each of the three primitive variables (ρ, u, p) as a sum of a mean flow quantity, which depends neither on space (due to the homogeneity assumption) nor on time, and a quantity fluctuating in space and time: $p(x,t) = \overline{p} + p'(x,t)$, etc. Assuming planar acoustic perturbations prevents vorticity waves from propagating [88]. There is no constriction at the downstream end of the tube so we can safely assume that entropy waves have no influence on the thermoacoustic behaviour. The Mach number is around 10^{-3}, therefore we assume zero mean flow. Neglecting second-order terms allows us to derive the acoustics equations

$$\frac{\partial \rho'}{\partial t} + \overline{\rho}\frac{\partial u'}{\partial x} = 0 \tag{4.7}$$

$$\overline{\rho}\frac{\partial u'}{\partial t} + \frac{\partial p'}{\partial x} = 0 \tag{4.8}$$

$$\frac{\partial p'}{\partial t} + \gamma\overline{p}\frac{\partial u'}{\partial x} = 0 \tag{4.9}$$

Relaxing the above assumptions to include indirect noise due to entropy, vorticity, and composition fluctuations would result in more complicated equations [89, 90, 72]. Eq. (4.7) resembles Eq. (4.9). In fact, by substituting $\rho' = p'/c^2$ into Eq. (4.7) we get exactly Eq. (4.9), provided that one recalls the ideal gas law result $\gamma\overline{p} = \overline{\rho}\,\overline{c}^2$. (This result stems from the definition of the sound speed $c^2 \equiv (\frac{dp}{d\rho})_s$ and from the isentropic relationship for a perfect gas $p \propto \rho^\gamma$.) This means that, for each pair of adjacent elements, there are only two independent equations to solve, Eq. (4.8) and Eq. (4.9), together with the following linearized jump conditions

$$[p']_{b^-}^{b^+} = 0 \tag{4.10}$$

$$[u']_{b^-}^{b^+} = 0 \tag{4.11}$$

We can re-write Eqs. (4.8) and (4.9) in matrix form as $\mathbf{u}_t + \mathbf{A}\mathbf{u}_x = \mathbf{0}$, i.e.

$$\begin{bmatrix} u' \\ p' \end{bmatrix}_t + \begin{bmatrix} 0 & 1/\overline{\rho} \\ \gamma\overline{p} & 0 \end{bmatrix} \begin{bmatrix} u' \\ p' \end{bmatrix}_x = \begin{bmatrix} 0 \\ 0 \end{bmatrix} \tag{4.12}$$

This hyperbolic system of equations can be solved by making a change of variables that allows us to decouple the two equations. To do so, we proceed by first diagonalizing matrix **A** as follows

$$\mathbf{A} = \mathbf{S}\boldsymbol{\Lambda}\mathbf{S}^{-1} = \begin{bmatrix} 1/(\overline{\rho}\,\overline{c}) & -1/(\overline{\rho}\,\overline{c}) \\ 1 & 1 \end{bmatrix} \begin{bmatrix} \overline{c} & 0 \\ 0 & -\overline{c} \end{bmatrix} \begin{bmatrix} \overline{\rho}\,\overline{c}/2 & 1/2 \\ -\overline{\rho}\,\overline{c}/2 & 1/2 \end{bmatrix} \tag{4.13}$$

We then substitute Eq. (4.13) into Eq. (4.12) and pre-multiply each term by $\mathbf{S}^{-1}$, thus obtaining

$$\mathbf{S}^{-1}\mathbf{u}_t + \boldsymbol{\Lambda}\mathbf{S}^{-1}\mathbf{u}_x = \mathbf{0} \tag{4.14}$$

The two equations can now be decoupled upon using $\mathbf{v} = \mathbf{S}^{-1}\mathbf{u}$, so that Eq. (4.14) becomes $\mathbf{v}_t + \mathbf{\Lambda}\mathbf{v}_x = \mathbf{0}$, which is

$$\begin{bmatrix} \mathscr{U} \\ \mathscr{P} \end{bmatrix}_t + \begin{bmatrix} \bar{c} & 0 \\ 0 & -\bar{c} \end{bmatrix} \begin{bmatrix} \mathscr{U} \\ \mathscr{P} \end{bmatrix}_x = \begin{bmatrix} 0 \\ 0 \end{bmatrix} \tag{4.15}$$

Each of these two equations is a simple wave equation, and the components of the vector $\mathbf{v} = [\mathscr{U}, \mathscr{P}]^T$ represent the Riemann invariants of the system, i.e. the travelling waves. The solution to the system is given by

$$\mathscr{U}(x,t) = f\left(t - \frac{x}{\bar{c}}\right) \qquad \text{(forward travelling wave)} \tag{4.16}$$

$$\mathscr{P}(x,t) = g\left(t + \frac{x}{\bar{c}}\right) \qquad \text{(backward travelling wave)} \tag{4.17}$$

The solution to the original system, Eq. (4.12), can be obtained by re-transforming the variables according to $\mathbf{u} = \mathbf{S}\,\mathbf{v}$, thus leading, for the generic acoustic element $(\cdot)_i$, to the following equations

$$p_i'(x,t) = f_i\left(t - \frac{x}{\bar{c}_i}\right) + g_i\left(t + \frac{x}{\bar{c}_i}\right) \tag{4.18}$$

$$u_i'(x,t) = \frac{1}{\bar{\rho}_\mathrm{i}\bar{c}_i}\left[f_i\left(t - \frac{x}{\bar{c}_i}\right) - g_i\left(t + \frac{x}{\bar{c}_i}\right)\right] \tag{4.19}$$

Taking the Laplace transform of Eqs. (4.18) and (4.19) decouples the time dependence from the space dependence and hence further simplifies the problem: $f_i\left(t - \frac{x}{\bar{c}_i}\right) = F_i(s)\ \mathrm{e}^{st}\ \mathrm{e}^{-s\frac{x}{\bar{c}_i}}$ and $g_i\left(t + \frac{x}{\bar{c}_i}\right) = G_i(s)\ \mathrm{e}^{st}\ \mathrm{e}^{+s\frac{x}{\bar{c}_i}}$. Here s is a complex number whose real part corresponds to the growth rate and whose imaginary part corresponds to the oscillation frequency, analogously to s_exp. The forward and backward travelling waves form standing waves that grow or decay in time with growth rate and frequency equal to s.

In the empty tube case, the jump conditions model the distributed momentum and energy losses that occur in the boundary layer. From Juniper [91], the fluctuating wall shear stress is $\tau_\mathrm{wall} = -(\rho\nu/\delta_\mathrm{bl})u'$, where $\delta_\mathrm{bl} = 2\pi[2\nu/\mathrm{Im}(s)]^{1/2}$. Consider now an element of tube with length Δx and total perimeter πD_tot, with $D_\mathrm{tot} = D + 2(D_\mathrm{r} + D_\mathrm{w})$, where D_r and D_w are the diameters of each rod and each wire. This diameter allows us to account for the presence of the two rods and wires to which the heater is attached. The total fluctuating force on the fluid element is

$$\Delta F = \Delta x\ \pi D_\mathrm{tot}\ \tau_\mathrm{wall} = -\Delta x\ D_\mathrm{tot}\frac{\rho}{2^{3/2}}[\nu\,\mathrm{Im}(s)]^{1/2}u' \tag{4.20}$$

We now define an equivalent area, and corresponding equivalent diameter, to account for a reduced flow area in the acoustic elements that contain heater rods and wires

$$A_{\mathrm{eq}} = A - A_{\mathrm{r}} - A_{\mathrm{w}} = \frac{\pi}{4}(D^2 - 2D_{\mathrm{r}}^2 - 2D_{\mathrm{w}}^2) = \frac{\pi}{4}D_{\mathrm{eq}}^2 \tag{4.21}$$

(If an acoustic element does not contain heater rods and wires, then we set $D_{\mathrm{tot}} = D_{\mathrm{eq}} = D$ and $A_{\mathrm{eq}} = A$.) Integrating the momentum equation across adjacent acoustic elements gives the pressure jump as a known linear function of the acoustic velocity u'

$$p'_{i+1}(t) - p'_i(t) = \frac{\Delta F(t)}{A_{\mathrm{eq}}} = -\Delta x \frac{D_{\mathrm{tot}}}{\pi D_{\mathrm{eq}}^2} \rho \, [2\nu \, \mathrm{Im}(s)]^{1/2} u'_i(t) \equiv -k_{\mathrm{vis,bl}} \, u'_i(t) \tag{4.22}$$

Similarly, from Juniper [91], the heat transfer from the wall into the gas is

$$\Delta \dot{q} = -\Delta x \; \pi D_{\mathrm{tot}} \frac{\lambda}{\delta_{\mathrm{bl}}} T' \tag{4.23}$$

where δ_{bl} is assumed to be the same as for the viscous boundary layer because the Prandtl number for air is close to 1. The gas is assumed isentropic and ideal, so $\frac{T'}{T} = \frac{p'}{p}\frac{\gamma-1}{\gamma}$ and $p = \rho R_{\mathrm{g}}^* T$. By combining the previous relationships, we obtain the heat transfer as a known linear function of the acoustic pressure p'

$$\Delta \dot{q} = -\Delta x \; D_{\mathrm{tot}} \, \frac{[\nu \, \mathrm{Im}(s)]^{1/2}}{2^{3/2} \mathrm{Pr}} \, p' \tag{4.24}$$

This can be written as a jump condition for the acoustic velocity. Integrating the energy equation across adjacent acoustic elements gives

$$u'_{i+1}(t) - u'_i(t) = \frac{\gamma - 1}{\gamma} \, \frac{1}{\overline{p}} \, \frac{4}{\pi D_{\mathrm{eq}}^2} \Delta \dot{q}(t) = -\Delta x \; \frac{\gamma - 1}{\gamma} \, \frac{1}{\overline{p}} \, \frac{[\nu \, \mathrm{Im}(s)]^{1/2}}{2^{3/2} \mathrm{Pr}} \, p'_i(t) \equiv -k_{\mathrm{th,bl}} \, p'_i(t) \tag{4.25}$$

In Eqs. (4.22) and (4.25), the parameters $k_{\mathrm{vis,bl}}$ and $k_{\mathrm{th,bl}}$ depend only on geometry, fluid properties and on a rough estimate of the oscillation frequency, $\mathrm{Im}(s)$, available from the experiments. Hence they are fully known. We can now combine Eqs. (4.18), (4.19), (4.22) and (4.25) and write

$$F_{i+1} \mathrm{e}^{-s \frac{x_{\mathrm{dd}}}{\overline{c}_{i+1}}} + G_{i+1} \mathrm{e}^{+s \frac{x_{\mathrm{dd}}}{\overline{c}_{i+1}}} - F_i \left(1 - \frac{k_{\mathrm{vis,bl}}}{\overline{\rho}_i \overline{c}_i}\right) \mathrm{e}^{-s \frac{x_{\mathrm{dd}}}{\overline{c}_i}} - G_i \left(1 + \frac{k_{\mathrm{vis,bl}}}{\overline{\rho}_i \overline{c}_i}\right) \mathrm{e}^{+s \frac{x_{\mathrm{dd}}}{\overline{c}_i}} = 0 \tag{4.26}$$

$$F_{i+1}\frac{\mathrm{e}^{-s\frac{x_{\mathrm{dd}}}{\bar{c}_{i+1}}}}{\bar{\rho}_{i+1}\bar{c}_{i+1}} - G_{i+1}\frac{\mathrm{e}^{+s\frac{x_{\mathrm{dd}}}{\bar{c}_{i+1}}}}{\bar{\rho}_{i+1}\bar{c}_{i+1}} + F_i\left(k_{\mathrm{th,bl}}-\frac{1}{\bar{\rho}_i\bar{c}_i}\right)\mathrm{e}^{-s\frac{x_{\mathrm{dd}}}{\bar{c}_i}} + G_i\left(k_{\mathrm{th,bl}}+\frac{1}{\bar{\rho}_i\bar{c}_i}\right)\mathrm{e}^{+s\frac{x_{\mathrm{dd}}}{\bar{c}_i}} = 0 \tag{4.27}$$

The problem is closed once the boundary conditions for the first and last acoustic elements are specified

$$F_1\mathrm{e}^{-s\frac{x_{\mathrm{u}}}{\bar{c}_1}} - R_{\mathrm{u}}G_1\mathrm{e}^{+s\frac{x_{\mathrm{u}}}{\bar{c}_1}} = 0 \tag{4.28}$$

$$R_{\mathrm{d}}F_N\mathrm{e}^{-s\frac{x_{\mathrm{d}}}{\bar{c}_N}} - G_N\mathrm{e}^{+s\frac{x_{\mathrm{d}}}{\bar{c}_N}} = 0 \tag{4.29}$$

where R_{u} and R_{d} are the upstream and downstream reflection coefficients, respectively, and the subscripts 1 and N represent the first and last acoustic elements, respectively. (N coincides with the total number of acoustic elements.) The nodes of the first pressure mode fall slightly outside the two ends, so the reflection coefficient is complex [92]. Eqs. (4.26) to (4.29) form a system of equations in F and G that can be written in matrix form as

$$\mathbf{A}(s)\ \mathbf{w} = \mathbf{0} \tag{4.30}$$

where $\mathbf{w}$ is the vector of complex amplitudes $[F_i, G_i]^{\mathrm{T}}$, with $i = 1, \ldots, N$. Eq. (4.30) represents a nonlinear eigenvalue problem. To solve Eq. (4.30), we seek the value of s that ensures $\det(\mathbf{A}) = 0$ in order to obtain the non-trivial solutions. This problem can be solved efficiently using Jacobi's formula

$$\frac{d}{ds}\det(\mathbf{A}) = \det(\mathbf{A})\ \mathrm{tr}\left(\mathbf{A}^{-1}\ \frac{d\mathbf{A}}{ds}\right) \tag{4.31}$$

where $\det(\cdot)$ and $\mathrm{tr}(\cdot)$ are the determinant and trace of a given matrix. An iterative scheme can be set up by discretizing Eq. (4.31) at the generic k-th iteration $(\cdot)^k$

$$\frac{(\det(\mathbf{A}))^{k+1} - (\det(\mathbf{A}))^{k}}{\delta s} = (\det(\mathbf{A}))^{k}\ \mathrm{tr}\left(\left(\mathbf{A}^{-1}\right)^{k}\ \left(\frac{d\mathbf{A}}{ds}\right)^{k}\right) \tag{4.32}$$

At each iteration we set $(\det(\mathbf{A}))^{k+1} = 0$, in a similar fashion to Newton's method when seeking the zero of a function. This simplifies Eq. (4.32) and allows us to find δs. The pseudo-code that solves the eigenvalue problem is the following

Algorithm 4.1: Solution to the eigenvalue problem using Jacobi's formula

```
initialize $s$ and $\delta s$;
while $|\delta s| > eps$ do
    compute $\mathbf{A}(s)$ and $\frac{d\mathbf{A}}{ds}$ using the network model;
    $\delta s \leftarrow -1/\mathrm{tr}\left(\mathbf{A}^{-1}\,\frac{d\mathbf{A}}{ds}\right)$;
    $s \leftarrow s + \delta s$;
end
```

For the empty tube we assume the two reflection coefficients to be identical, $R_\mathrm{u} = R_\mathrm{d} = R$. In the empty tube case, we use Eq. (4.30) to solve for R given s, rather than for s given R. To do so, in Eq. (4.30) we set $s = s_\mathrm{exp}$ and find R using the same algorithm as Algorithm 4.1, except that matrix derivatives are computed with respect to R. By averaging over the 1100 empty tube experiments available, we find an average $s_\mathrm{exp} = -7.61\ \mathrm{rad \cdot s^{-1}} + i\ 168.10$ Hz, which leads to an average $R = -0.9758 + i\ 0.1003$. This value is always used for the upstream reflection coefficient. In the cold flow cases (Secs. 4.2 and 4.3), this value is also used for the downstream reflection coefficient. However, in the hot flow case (Chapter 5), the downstream reflection coefficient is computed using the multi-microphone method due to the fact that the reflection coefficient varies when the temperature of the downstream end varies [93, 94].

The reflection coefficient in the empty tube case may also be computed using the analytical formulation proposed by Levine and Schwinger [92]. However, [92] base their analysis on a semi-infinite unflanged circular pipe, which necessarily leads to small errors in the value of R. Because the reflection coefficient is an extremely important quantity in thermoacoustics, we choose to compute it in the way described above rather than with the fomula provided by [92]. To prove how sensitive the complex frequency s is to small changes of R, we can compute $\frac{ds}{dR}$ for a simplified case. If we imagine an empty tube with zero visco-thermal losses modelled with a network model made up of two elements (subscripts 1 and 2) that meet at $x = b$, then Eq. (4.30) simplifies to

$$\begin{bmatrix} -1 - R_\mathrm{u} e^{-s\tau_\mathrm{u}} & 1 + R_\mathrm{d} e^{-s\tau_\mathrm{d}} \\ 1 - R_\mathrm{u} e^{-s\tau_\mathrm{u}} & 1 - R_\mathrm{d} e^{-s\tau_\mathrm{d}} \end{bmatrix} \begin{bmatrix} G_1 \\ F_2 \end{bmatrix} = \begin{bmatrix} 0 \\ 0 \end{bmatrix} \tag{4.33}$$

where $\tau_\mathrm{u} = 2b/\bar{c}_1$ and $\tau_\mathrm{d} = 2(L-b)\bar{c}_2$, and where $\bar{c}_1 = \bar{c}_2 = \bar{c}$ because of no temperature gradient. Setting the determinant of the above matrix to zero leads to the following expression

$$R_\mathrm{u} R_\mathrm{d} = e^{s(\tau_\mathrm{u} + \tau_\mathrm{d})} \tag{4.34}$$

By defining the new timescale $\tau_{\text{tot}} = \tau_{\text{u}} + \tau_{\text{d}} = \frac{2b}{\bar{c}_1} + \frac{2(L-b)}{\bar{c}_2} = \frac{2L}{\bar{c}}$, and assuming $R_{\text{u}} = R_{\text{d}} = R$, we obtain

$$R^2 = e^{s\tau_{\text{tot}}} \tag{4.35}$$

Implicit differentiation of the above equation leads to

$$2R\,dR = \tau_{\text{tot}}\, e^{s\tau_{\text{tot}}} ds = \tau_{\text{tot}}\, R^2 ds \tag{4.36}$$

which allows us to derive the following analytical expression for the sensitivity of s with respect to R

$$\frac{ds}{dR} = \frac{2}{\tau_{\text{tot}} R} = \frac{\bar{c}}{RL} \tag{4.37}$$

Eq. (4.37) shows that for an empty tube the sensitivity of s to small changes of R is proportional to the average speed of sound inside the tube divided by the tube length, a value that in our case is larger than 340 s^{-1}. In the presence of heater and/or thermocouples inside the tube, an equivalent expression is more complex to derive analytically and does not provide straightforward insight. However, it is sensible to believe that this sensitivity remains high. This justifies the computation of R via Eq. (4.30) rather than analytically from the relation provided in [92].

4.2 Modelling the thermo-viscous drag from the switched-off heater

When the heater is in place but switched off, the decay rate is always stronger (i.e. more negative) than it is for the empty tube. The shift is greatest when the heater is near the velocity antinode and least near the velocity node (Fig. 2.5a). Juniper [91] provide feedback sensitivities from u' and from p' to the acoustic mass, momentum and energy equations for a Rijke tube. These sensitivities are obtained with discrete adjoint of the Finite-Element Method, and are shown in Figure 7a of [91], which, for convenience, is also reported in Fig. 4.2 of this thesis. In Fig. 4.2, first we note that the feedback sensitivities to the mass equation are identical to the feedback sensitivities to the energy equation. This confirms that the mass and energy equations are linearly dependent, as already proved in Sec. 4.1. Second, we focus on the absolute value of the feedback sensitivities (i.e. $\sqrt{(\text{Re}(f))^2 + (\text{Im}(f))^2}$ with f being the feedback sensitivity). We note from Fig. 2.5a that in the presence of the heater (i) the decay rate becomes more negative (compared to the empty tube case) when the heater is placed at the centre of the tube ($x_{\text{h}}/L = 0.5$). From Fig. 4.2 we see that the only mechanism that can cause this is pressure into the energy equation, i.e. thermal drag. (ii) The decay rate is most negative when the heater is at the entrance of the tube ($x_\mathrm{h}/L \approx 0$). From Fig. 4.2 we see that the only mechanism that can cause this is velocity into the momentum equation, i.e. viscous drag. Finally, the frequency is clearly affected by the heater (Fig. 2.5a), suggesting that we might need to include a time delay. This is indeed confirmed by the work of Lighthill [51]. Thus, the jump conditions at the heater location are written as

$$p'_{i+1}(t) - p'_i(t) = -k_\mathrm{vis,h}\, u'_i(t - \tau_\mathrm{vis,h}) \tag{4.38}$$

$$u'_{i+1}(t) - u'_i(t) = -k_\mathrm{th,h}\, p'_i(t - \tau_\mathrm{th,h}) \tag{4.39}$$

Eqs. (4.38) and (4.39) represent the simplest acoustic model of the heater we can build. The four heater parameters, $k_\mathrm{vis,h}$, $k_\mathrm{th,h}$, $\tau_\mathrm{vis,h}$, and $\tau_\mathrm{th,h}$ are first inferred by nonlinear regression and then with the Markov Chain Monte Carlo method. For nonlinear regression we use the Matlab® inbuilt function `lsqnonlin` with the Levenberg-Marquardt algorithm. We choose a real cost function, represented by the sum of the squares of the differences between the predicted and the observed decay rates and frequencies. When using nonlinear regression, the model parameters are inferred using all the experimental data available in order to obtain as accurate results as possible. Fig. 4.3a shows the predictions of the network model and compares them to the experimental measurements for all the heater positions. The inferred model parameters are reported in the figure caption. The time delay of the viscous drag, $\tau_\mathrm{vis,h}$, is negative, while the thermal time delay, $\tau_\mathrm{th,h}$, is positive, in agreement with Lighthill [51]. The sign of the time delays simply determines whether the waves u' and p' are in phase or out of phase. The pressure loss coefficient due to viscous drag at the heater location, $k_\mathrm{vis,h}$, is several orders of magnitude larger than the thermal loss coefficient, $k_\mathrm{th,h}$. Nevertheless, setting $k_\mathrm{th,h}$ to zero results in relatively large errors in Fig. 4.3a, meaning that the heat transfer to and from the heater cannot be neglected, even when the heater is switched off. We tried to build several other models alternative to Eqs. (4.38) and (4.39). For example, we tested different combinations of models in which the pressure jump is proportional to p' or the velocity jump is proportional to u'. However, these all failed to predict the correct trend. This is in perfect agreement with the predictions of the feedback sensitivities in Fig. 4.2.

Nonlinear regression has the advantage of being very fast. However, it does not provide any information on the uncertainty of the parameters and of the model predictions, which would help us quantify the robustness of our model. The computation of the parameter uncertainty starting from state observations is a typical inverse problem, which could be tackled, for example, with the ensemble Kalman filter, as done with the slow time-scale model. However, we prefer using the Markov Chain Monte Carlo method because this can explore any possible nonlinearity and/or multimodality present in the posterior distribution, thus providing

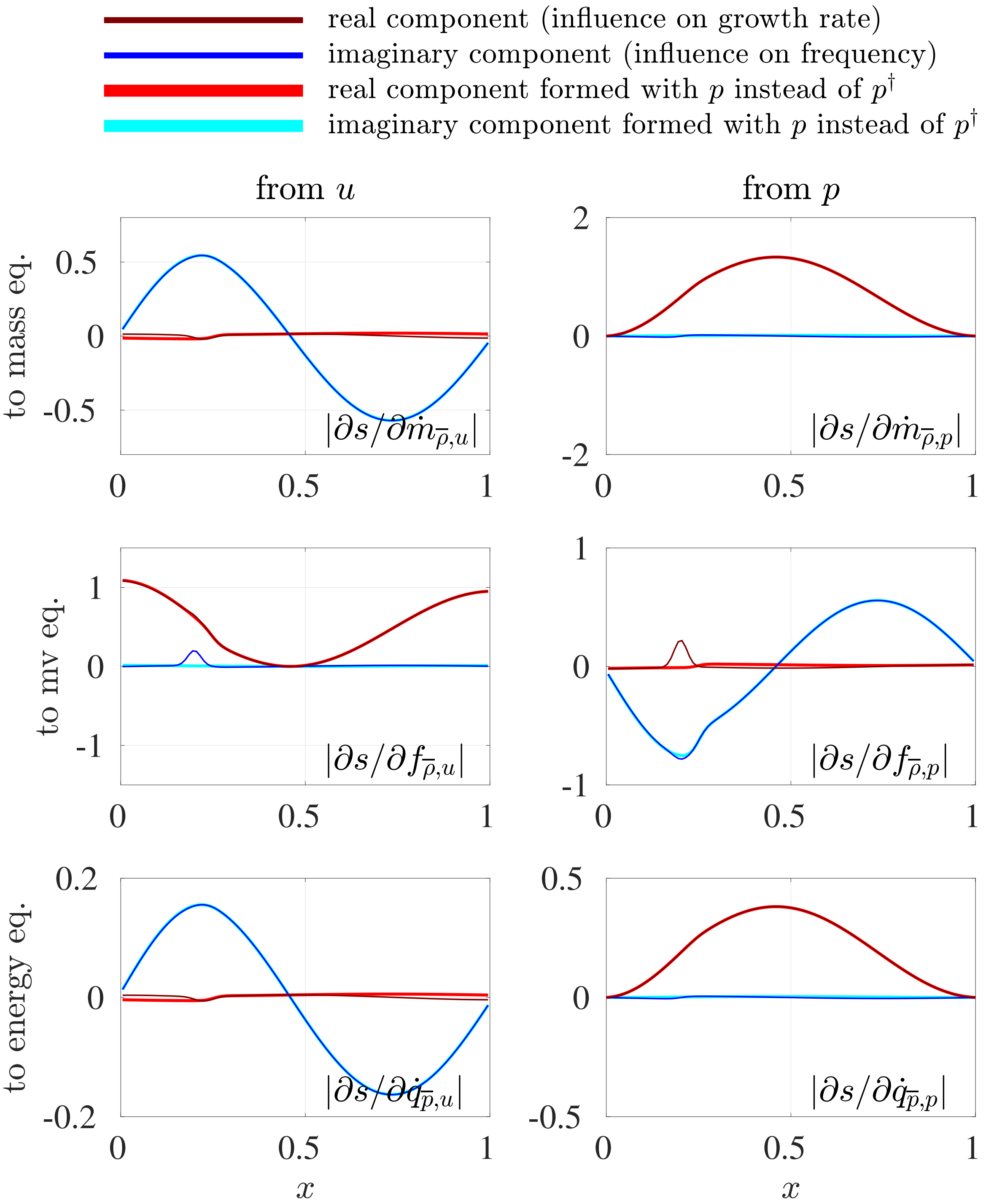

Fig. 4.2 Real and imaginary components of the feedback sensitivities, calculated with discrete adjoint (`DA`) of the finite element method (`FEM`) for the Rijke tube. The wider lines show the same sensitivities calculated when the adjoint pressure, $p^\dagger$, is replaced by the direction pressure, p, i.e. as if the system were self-adjoint. There is little difference for the Rijke tube. (This figure is taken from Juniper [91] and corresponds to Figure 7a of [91].)

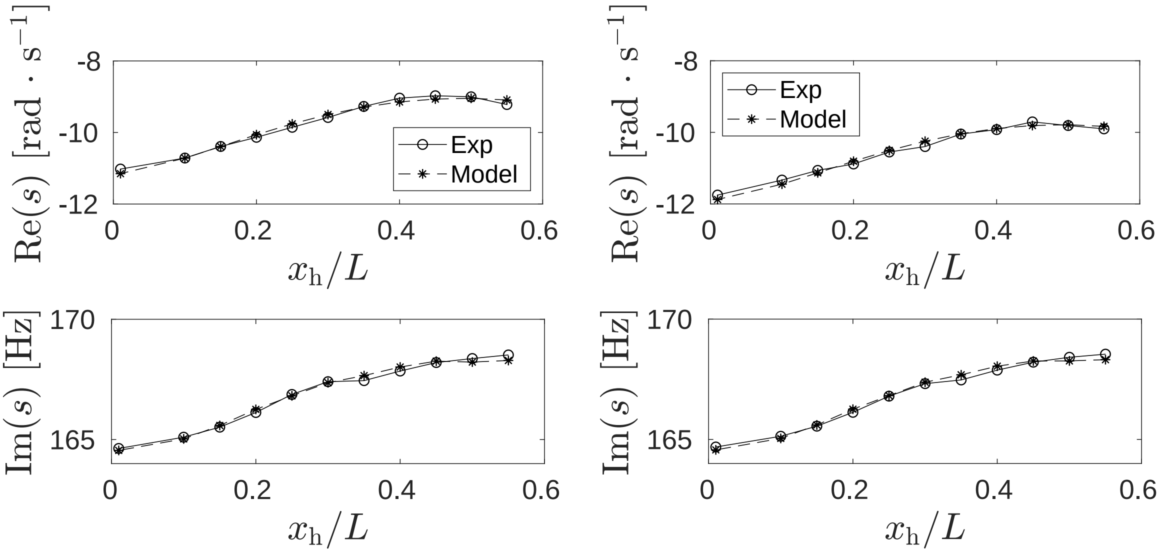

(a) Heater off without thermocouples. The inferred heater parameters are: $k_{\mathrm{vis,h}} = 27.3$ kg m^{-2} s^{-1}, $k_{\mathrm{th,h}} = 1.53 \cdot 10^{-5}$ kg^{-1} m^{2} s, $\tau_{\mathrm{vis,h}} = -1.36 \cdot 10^{-3}$ s, and $\tau_{\mathrm{th,h}} = 8.98 \cdot 10^{-4}$ s. All experimental data are used to infer the model parameters.

(b) Heater off with thermocouples. The inferred thermocouple parameters are: $k_{\mathrm{vis,t}} = 0.257$ kg m^{-2} s^{-1}, $k_{\mathrm{th,t}} = 1.44 \cdot 10^{-7}$ kg^{-1} m^{2} s. All experimental data are used to infer the model parameters.

Fig. 4.3 Decay rate (top) and frequency (bottom) of acoustic oscillations when the heater is switched off and placed at different positions x_{h}/L. Comparison of experimental observations and model predictions using nonlinear regression for two configurations: (a) no thermocouples present inside the tube, and (b) thermocouples present inside the tube.

more accurate results than the EnKF, which on the other hand can handle only Gaussian distributions. Moreover, instead of using all the available experiments as ~~done~~ above, here we train the model using only the experiments available at $x_\mathrm{h}/L = [0.20, 0.25, 0.30]$, which represent our training set. This allows us to test *a-posteriori* whether the model is able to extrapolate well on the heater positions outside of the training range. To use the MCMC, we need to define the likelihood function of the experimental observations. We assume a Gaussian likelihood function for convenience. The covariance matrix of the likelihood function, $\boldsymbol{\sigma}^2_\mathrm{lik}$, is a 2×2 matrix that allows us to compute the probability of observing the data, given the model parameters. The entries of this matrix represent a combination of observation error and model error, and hence are unknown. We assume the off-diagonal elements of $\boldsymbol{\sigma}^2_\mathrm{lik}$ to be zero and we treat the diagonal elements as two unknown parameters, σ^2_DR and σ^2_f, which we infer with the Markov Chain Monte Carlo method. Since we have no accurate knowledge of these six parameters ($k_\mathrm{vis,h}$, $k_\mathrm{th,h}$, $\tau_\mathrm{vis,h}$, $\tau_\mathrm{th,h}$, σ_DR, σ_f), we use a multivariate uniform distribution as a prior. We centre the four heater parameters around the best-fit values obtained from nonlinear regression and use reasonable intervals for σ_DR and σ_f (both expressed in $\mathrm{rad}\cdot\mathrm{s}^{-1}$):

$$p(\boldsymbol{\psi}) = p\left(\begin{bmatrix} k_\mathrm{vis,h} \\ k_\mathrm{th,h} \\ \tau_\mathrm{vis,h} \\ \tau_\mathrm{th,h} \\ \sigma_\mathrm{DR} \\ \sigma_\mathrm{f} \end{bmatrix}\right) = \mathscr{U}\left(\begin{bmatrix} (2.7\pm1.5)\cdot10^{1} \\ (1.5\pm1)\cdot10^{-5} \\ (-1.5\pm1)\cdot10^{-3} \\ (8\pm6)\cdot10^{-4} \\ (4\pm3)\cdot10^{-1} \\ (3\pm2)\cdot10^{0} \end{bmatrix}\right) \tag{4.40}$$

Next, we need to define the proposal distribution, $\mathscr{R}$. We use a Gaussian proposal distribution with a diagonal covariance matrix $\boldsymbol{\sigma}^2_\mathscr{R}$ chosen by trial and error as explained in Sec. 1.4. As an example, the covariance matrix used for this particular case is the following

$$\boldsymbol{\sigma}^2_\mathscr{R} = \begin{bmatrix} 2\cdot10^{-3} & 0 & 0 & 0 & 0 & 0 \\ 0 & 5\cdot10^{-15} & 0 & 0 & 0 & 0 \\ 0 & 0 & 5\cdot10^{-11} & 0 & 0 & 0 \\ 0 & 0 & 0 & 1\cdot10^{-11} & 0 & 0 \\ 0 & 0 & 0 & 0 & 1\cdot10^{-4} & 0 \\ 0 & 0 & 0 & 0 & 0 & 1\cdot10^{-4} \end{bmatrix} \tag{4.41}$$

where the diagonal elements of $\boldsymbol{\sigma}^2_\mathscr{R}$ from the top-left corner to the bottom-right corner represent the variances of $\{k_\mathrm{vis,h}, k_\mathrm{th,h}, \tau_\mathrm{vis,h}, \tau_\mathrm{th,h}, \sigma_\mathrm{DR}, \sigma_\mathrm{f}\}$, respectively. We run 12 different Markov chains in parallel, each of which is initialized with a set of parameters $\boldsymbol{\psi}^0$ randomly sampled from the prior distribution in Eq. (4.40). Each chain evolves independently. Using $\boldsymbol{\psi}^0$ we solve the network model and, for each experiment k, we compute the complex frequency predicted by the model, $\boldsymbol{s}_k^0$. Here $\boldsymbol{s}$ is a two-dimensional real vector containing the real and imaginary parts of s. Using $(\boldsymbol{\sigma}_{\text{lik}}^0)^2$ we then evaluate the log-likelihood function $\mathscr{L}$

$$\mathscr{L} = \log[\prod_k p(\boldsymbol{s}_{\exp,k}|\boldsymbol{s}_k^0;(\boldsymbol{\sigma}_{\text{lik}}^0)^2)] = \sum_k \log[p(\boldsymbol{s}_{\exp,k}|\boldsymbol{s}_k^0;(\boldsymbol{\sigma}_{\text{lik}}^0)^2)] \tag{4.42}$$

Here we use the fact that experiments are independent, meaning that the total likelihood is given by the product of the individual likelihoods. The individual likelihood $p(\boldsymbol{s}_{\exp,k}|\boldsymbol{s}_k^0;(\boldsymbol{\sigma}_{\text{lik}}^0)^2)$ is computed by evaluating at $\boldsymbol{s}_{\exp,k}$ the probability density function of a Gaussian distribution with mean $\boldsymbol{s}_k^0$ and covariance matrix $(\boldsymbol{\sigma}_{\text{lik}}^0)^2$, namely $\mathscr{N}\left(\boldsymbol{s}_k^0,(\boldsymbol{\sigma}_{\text{lik}}^0)^2\right)$. To avoid round-off errors, it is desirable to work with logarithms of probability density functions whenever possible. By doing so, a multiplication of two exponential functions becomes a sum of their exponents (see Eq. (4.42)). After computing the log-likelihood, we randomly sample a new set of parameters $\boldsymbol{\psi}^1$ from the proposal distribution $\mathscr{R} \sim \mathscr{N}(\boldsymbol{\psi}^0, \boldsymbol{\sigma}_{\mathscr{R}}^2)$, checking that $\boldsymbol{\psi}^1$ falls inside the prior distribution defined in Eq. (4.40). Otherwise we re-sample. Using $\boldsymbol{\psi}^1$ we compute the new model predictions, $\boldsymbol{s}_k^1$, and hence the new value of the log-likelihood function, $\mathscr{L} = \sum_k \log[p(\boldsymbol{s}_{\exp,k}|\boldsymbol{s}_k^1;(\boldsymbol{\sigma}_{\text{lik}}^1)^2)]$. Finally, we compute the acceptance ratio r using Eq. (1.24) and decide whether the new sampled set, $\boldsymbol{\psi}^1$, is accepted or rejected. A new sample $\boldsymbol{\psi}^2$ is then compared to $\boldsymbol{\psi}^1$ if $\boldsymbol{\psi}^1$ was accepted, or to $\boldsymbol{\psi}^0$ if $\boldsymbol{\psi}^1$ was rejected. The algorithm runs until the accepted parameter samples converge and all the 12 chains are well mixed. Fig. 4.4 shows the result of this process for the four heater parameters. The burn-in regions are identified by the vertical solid lines in Fig. 4.4: samples before these lines are discarded because the algorithm has not converged yet.

Once the samples in the burn-in region are discarded, for each experiment in theory we could use the standard Monte Carlo method to randomly sample from the converged posterior (parameter) distribution and obtain the predicted complex frequencies s. In this way, we would propagate the uncertainty from the parameters to the state. However, this procedure would allow us to compute the uncertainty of s only due to uncertainty in the parameters. We are instead interested in quantifying the total uncertainty, which is made up of three contributions: parameter uncertainty, model uncertainty, and observation uncertainty. To compute the total uncertainty, for each experimental datapoint we proceed as follows. We draw 500 samples from the posterior distribution obtained with the MCMC. For each of these samples, we first compute the corresponding complex frequency s predicted by the network model, and then draw 50 samples from a Gaussian distribution centred around s and with

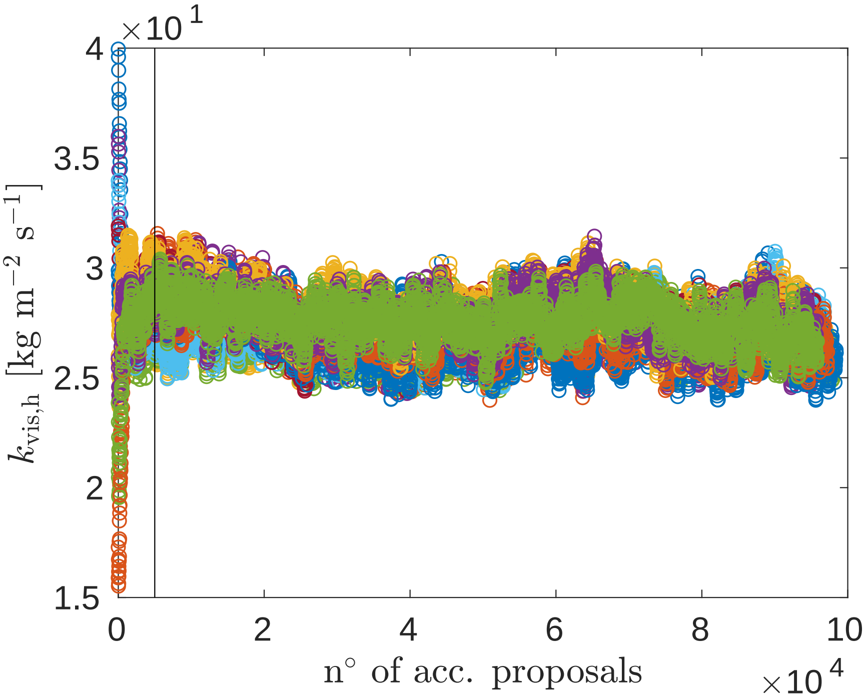

(a) $k_{\mathrm{vis,h}}$

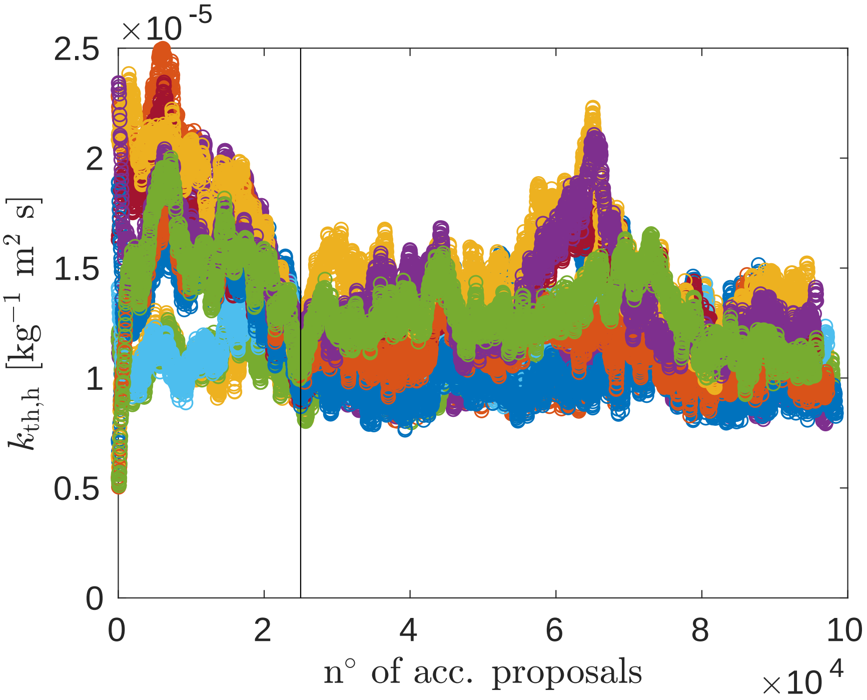

(b) $k_{\mathrm{th,h}}$

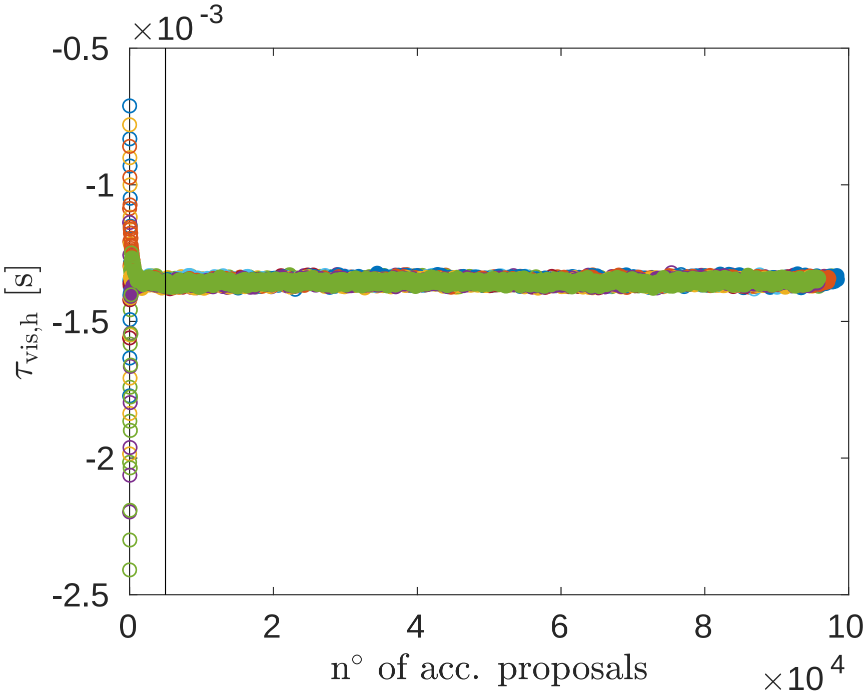

(c) $\tau_{\mathrm{vis,h}}$

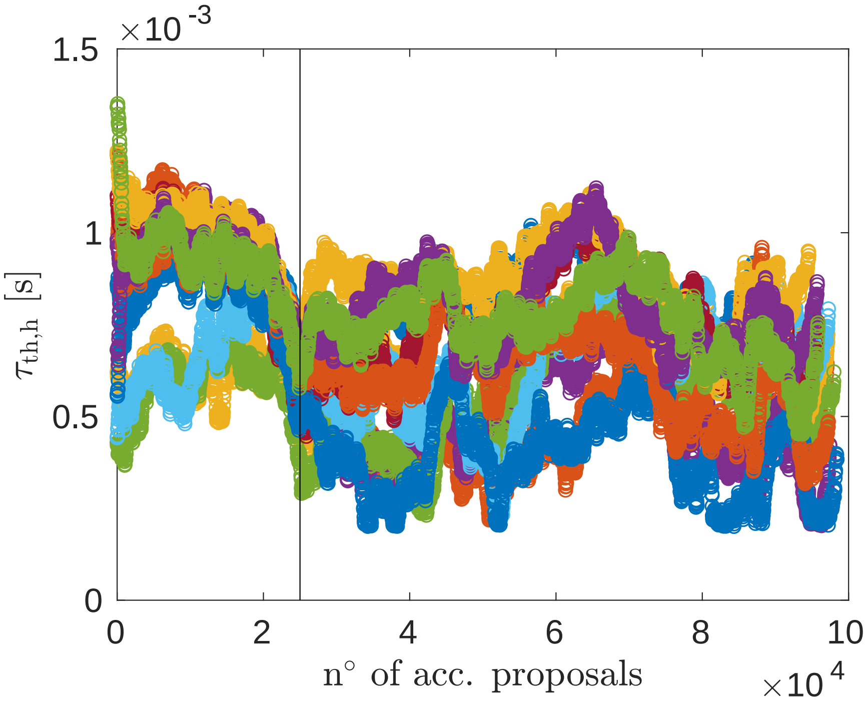

(d) $\tau_{\mathrm{th,h}}$

Fig. 4.4 Evolution of the 12 Markov chains for the case in which the heater is in place but switched off and the thermocouples are not present. Vertical black lines delimit the burn-in region, which comprises accepted proposals that are discarded.

covariance matrix equal to $\boldsymbol{\sigma}^2_{\text{lik}}$. (The sizes of the samples (500 and 50) are chosen arbitrarily. Results do not significantly change when different sizes are used, provided that these are not too small.) In this way, we are able to obtain a much wider ensemble of predicted complex frequencies, from which classic statistics (mean and standard deviation) can be extracted. This procedure is applied to both training and testing sets, and is reported in Algorithm 4.2.

Algorithm 4.2: Forward uncertainty propagation to state s using standard Monte Carlo. Line 7 is key for the computation of the total uncertainty, shown in Figs. 4.5, 5.1, 5.2, C.1 and D.1.

```
1  foreach experimental datapoint do
2      initialize array $\boldsymbol{z}$;
3      for $i = 1$ to 500 do
           /* The parameters to use depend on your model */
4          $(k_{\text{vis,h}},\ k_{\text{th,h}},\ \tau_{\text{vis,h}},\ \tau_{\text{th,h}},\ \sigma_{\text{DR}},\ \sigma_{\text{f}}) \leftarrow$ draw a sample from MCMC posterior;
5          $s \leftarrow$ use network model with $(k_{\text{vis,h}},\ k_{\text{th,h}},\ \tau_{\text{vis,h}},\ \tau_{\text{th,h}})$;
6          $\boldsymbol{\sigma}^2_{\text{lik}} \leftarrow$ build covariance matrix of the likelihood function using $(\sigma_{\text{DR}},\ \sigma_{\text{f}})$;
7          draw 50 samples from $\mathcal{N}(s, \boldsymbol{\sigma}^2_{\text{lik}})$ and append to $\boldsymbol{z}$;
8      end
       /* Now compute state prediction (mean) and uncertainty (standard deviation)
          for this experimental datapoint */
9      compute mean and standard deviation of $\boldsymbol{z}$;
10 end
```

Results in Fig. 4.5a show good agreement between model predictions and experimental observations, especially considering that the size of the training set is relatively small (27%). This is because the model we use contains the relevant physics of the problem and hence can extrapolate well beyond the training range. It is also important to note that, as expected, the parameter values in Fig. 4.4 agree with the best-fit values found with nonlinear regression and reported in the caption of Fig. 4.3a, although nonlinear regression cannot also assimilate the uncertainty.

4.3 Modelling the visco-thermal drag from the thermocouples

We assume that all eight thermocouples are identical drag devices across which acoustic momentum and energy losses occur through jump conditions. The total number of acoustic

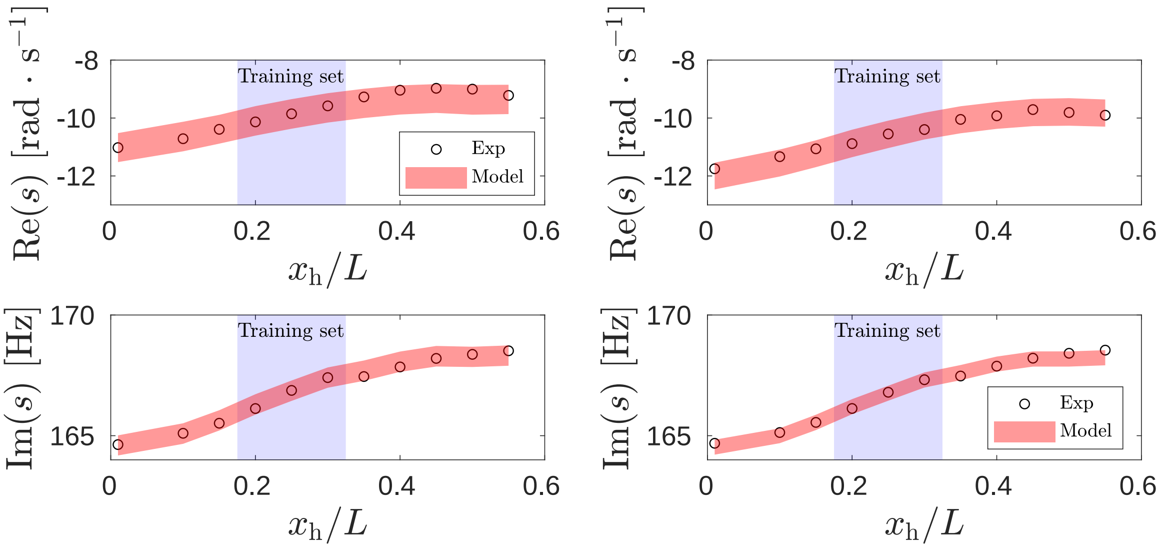

(a) Heater off without thermocouples. Only the experimental data corresponding to the heater positions highlighted in blue are used for inference.

(b) Heater off with thermocouples. Only the experimental data corresponding to the heater positions highlighted in blue are used for inference.

Fig. 4.5 Decay rate (top) and frequency (bottom) of acoustic oscillations when the heater is switched off and placed at different positions x_h/L. Comparison of experimental observations and model predictions using the MCMC with 95% confidence intervals for two configurations: (a) no thermocouples present inside the tube, and (b) thermocouples present inside the tube.

elements of the network model in the presence of both the heater and the 8 thermocouples is therefore 49. For simplicity, and because the influence of the thermocouples is small, we assume the time delays associated with the visco-thermal drag at the thermocouples to be negligible. Thus, the jump conditions across the thermocouples are

$$p'_{i+1}(t) - p'_i(t) = -k_{\mathrm{vis,t}}\, u'_i(t) \tag{4.43}$$

$$u'_{i+1}(t) - u'_i(t) = -k_{\mathrm{th,t}}\, p'_i(t) \tag{4.44}$$

To further simplify the problem, we assume that the ratio of viscous-to-thermal drag for the thermocouples is the same as that for the heater: $k_{\mathrm{vis,t}}/k_{\mathrm{th,t}} = k_{\mathrm{vis,h}}/k_{\mathrm{th,h}}$. This means that the visco-thermal drag of the thermocouples is described by a single independent parameter, e.g. $k_{\mathrm{vis,t}}$. The next set of experimental results, which contain both the heater and the thermocouples, is used to learn this independent thermocouple parameter. As in Sec. 4.2, we first perform nonlinear regression. When doing this, we fix the heater parameters to the ones found in Sec. 4.2 (see caption of Fig. 4.3a). At each algorithm iteration, we compute $k_{\mathrm{th,t}} = k_{\mathrm{vis,t}}/k_{\mathrm{vis,h}} \cdot k_{\mathrm{th,h}}$. Once again, we use the experiments available at all the heater positions for inference. The result of this process is shown in Fig. 4.3b and the values of $k_{\mathrm{vis,t}}$ and $k_{\mathrm{th,t}}$ are reported in the figure caption. As we can see, the additional drag due to the presence of the thermocouples is well captured by this simple model.

Next, we use the MCMC method to infer the uncertainty first in the parameters and then in the state. When doing so, we train our model using only the experiments available at three heater positions: $x_{\mathrm{h}}/L = [0.20, 0.25, 0.30]$, analogously to what was done in Sec. 4.2. Because we now have good knowledge of the four heater parameters from Sec. 4.2, we use a mixed prior distribution to describe the heater and thermocouple parameters, therefore allowing the heater parameters to float. In particular, for the four heater parameters and for the diagonal elements of the likelihood covariance matrix we use a multivariate Gaussian distribution that approximates the posterior found in Sec. 4.2, whereas for the independent thermocouple parameter, $k_{\mathrm{vis,t}}$, we use a uniform distribution around the best-fit value found with nonlinear regression

$$p(\psi_7) = p(k_{\mathrm{vis,t}}) = \mathscr{U}\left((3 \pm 3) \cdot 10^{-1}\right) \tag{4.45}$$

We choose again a proposal distribution $\mathscr{R}$ that is Gaussian with a diagonal covariance matrix whose entries are chosen by trial and error for simplicity

$$\boldsymbol{\sigma}^2_{\mathscr{R}} = \begin{bmatrix} 5\cdot 10^{-4} & 0 & 0 & 0 & 0 & 0 & 0 \\ 0 & 9\cdot 10^{-16} & 0 & 0 & 0 & 0 & 0 \\ 0 & 0 & 5\cdot 10^{-12} & 0 & 0 & 0 & 0 \\ 0 & 0 & 0 & 4\cdot 10^{-12} & 0 & 0 & 0 \\ 0 & 0 & 0 & 0 & 1\cdot 10^{-4} & 0 & 0 \\ 0 & 0 & 0 & 0 & 0 & 1\cdot 10^{-4} & 0 \\ 0 & 0 & 0 & 0 & 0 & 0 & 1.1\cdot 10^{-5} \end{bmatrix} \tag{4.46}$$

where the diagonal elements of $\boldsymbol{\sigma}^2_{\mathscr{R}}$ from the top-left corner to the bottom-right corner represent the variance of $\{k_{\mathrm{vis,h}}, k_{\mathrm{th,h}}, \tau_{\mathrm{vis,h}}, \tau_{\mathrm{th,h}}, \sigma_{\mathrm{DR}}, \sigma_{\mathrm{f}}, k_{\mathrm{vis,t}}\}$, respectively. Every time we sample a new set of parameters $\boldsymbol{\psi}$, we first compute $k_{\mathrm{th,t}} = k_{\mathrm{vis,t}} \cdot k_{\mathrm{th,h}}/k_{\mathrm{vis,h}}$ and then perform the steps decribed in Sec. 4.2. The model predictions for both the training and the testing data are shown in Fig. 4.5b. As before, the agreement is excellent on both training and testing sets. This shows that a relatively simple model is able to predict the system behaviour in a reliable manner, provided that sufficient data are used for training and that the model contains the relevant physics of the problem. In Fig. 4.5b we also note that the uncertainty in the predictions is slightly lower than in Fig. 4.5a, which is because we have less uncertainty in the prior. Fig. 4.6 shows the two-dimensional posterior distributions for each pair of heater and thermocouple parameters, which agree with the best-fit regression values found in Sec. 4.2. The main advantage of using the MCMC is that we are able to visualize any non-normality or multi-modality feature present in the posterior. Indeed, in Fig. 4.6 we see that none of the distributions is multi-modal but that some of them are non-Gaussian. Had we used the ensemble Kalman filter, we would not have been able to observe these features.

4.4 Multi-microphone method

The reflection coefficient at the open end of a tube depends on the temperature at the open end [93, 94]. When the heater is switched on, air leaves the tube at 300 to 460 K, depending on the heater power (see Fig. 3.4). Assuming a constant downstream reflection coefficient equal to the value computed in Sec. 4.1 therefore introduces systematic errors. We account for this variable downstream reflection coefficient using the multi-microphone method, which exploits the information contained in the microphone signals. The multi-microphone method (MMM) represents an extension of the classic two-microphone method (TMM) that was first

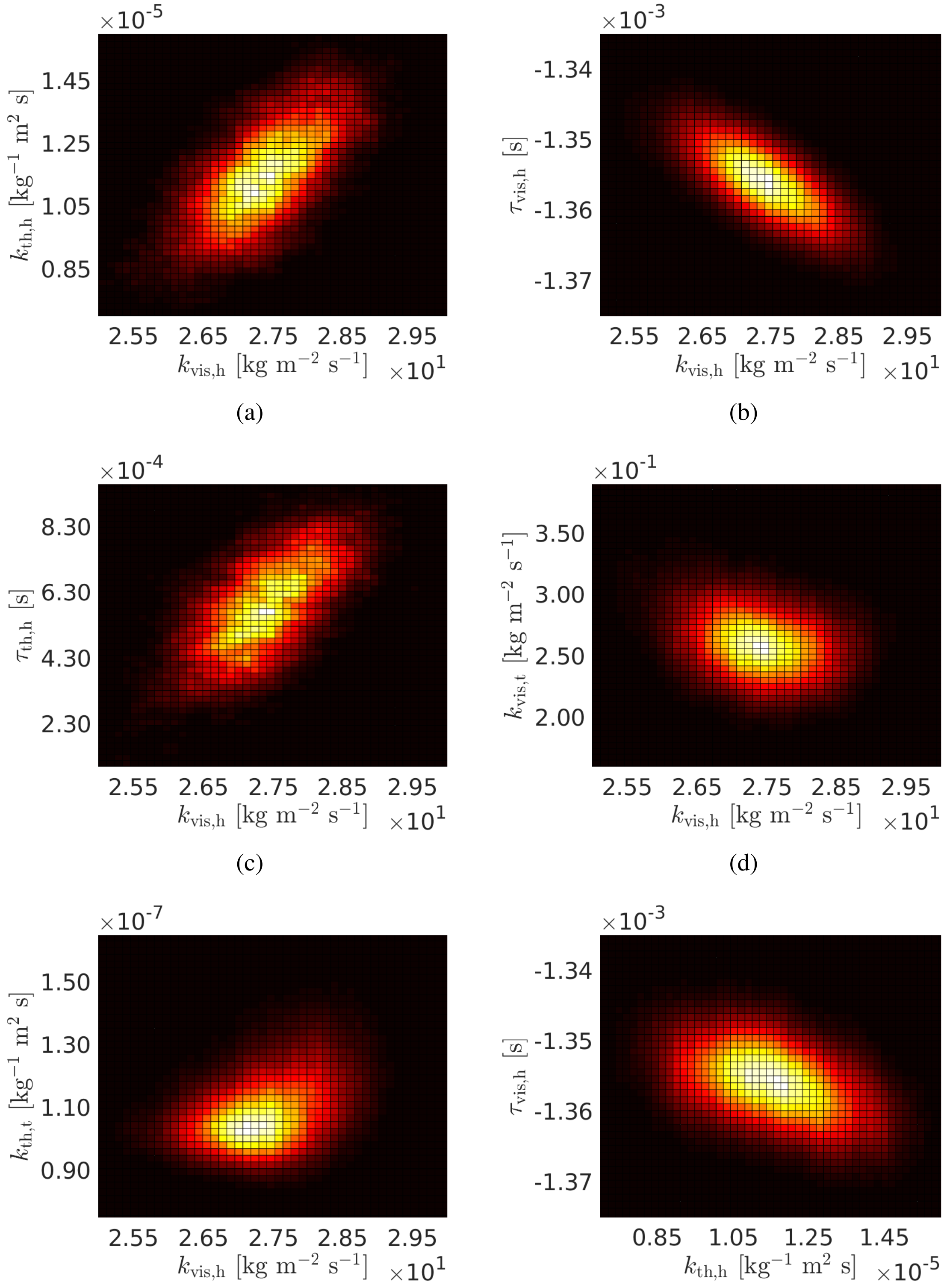

$\times 10^{-5}$
1.45
1.25
1.05
0.85
$k_{\mathrm{th,h}}$ [kg^{-1} m^2 s]
2.55
2.65
2.75
2.85
2.95
$k_{\mathrm{vis,h}}$ [kg m^{-2} s^{-1}]
$\times 10^{1}$
$\times 10^{-3}$
-1.34
-1.35
-1.36
-1.37
$\tau_{\mathrm{vis,h}}$ [s]
2.55
2.65
2.75
2.85
2.95
$k_{\mathrm{vis,h}}$ [kg m^{-2} s^{-1}]
$\times 10^{1}$
$\times 10^{-4}$
8.30
6.30
4.30
2.30
$\tau_{\mathrm{th,h}}$ [s]
2.55
2.65
2.75
2.85
2.95
$k_{\mathrm{vis,h}}$ [kg m^{-2} s^{-1}]
$\times 10^{1}$
$\times 10^{-1}$
3.50
3.00
2.50
2.00
$k_{\mathrm{vis,t}}$ [kg m^{-2} s^{-1}]
2.55
2.65
2.75
2.85
2.95
$k_{\mathrm{vis,h}}$ [kg m^{-2} s^{-1}]
$\times 10^{1}$
$\times 10^{-7}$
1.50
1.30
1.10
0.90
$k_{\mathrm{th,t}}$ [kg^{-1} m^2 s]
2.55
2.65
2.75
2.85
2.95
$k_{\mathrm{vis,h}}$ [kg m^{-2} s^{-1}]
$\times 10^{1}$
$\times 10^{-3}$
-1.34
-1.35
-1.36
-1.37
$\tau_{\mathrm{vis,h}}$ [s]
0.85
1.05
1.25
1.45
$k_{\mathrm{th,h}}$ [kg^{-1} m^2 s]
$\times 10^{-5}$

(a) (b)

(c) (d)

(e) (f)

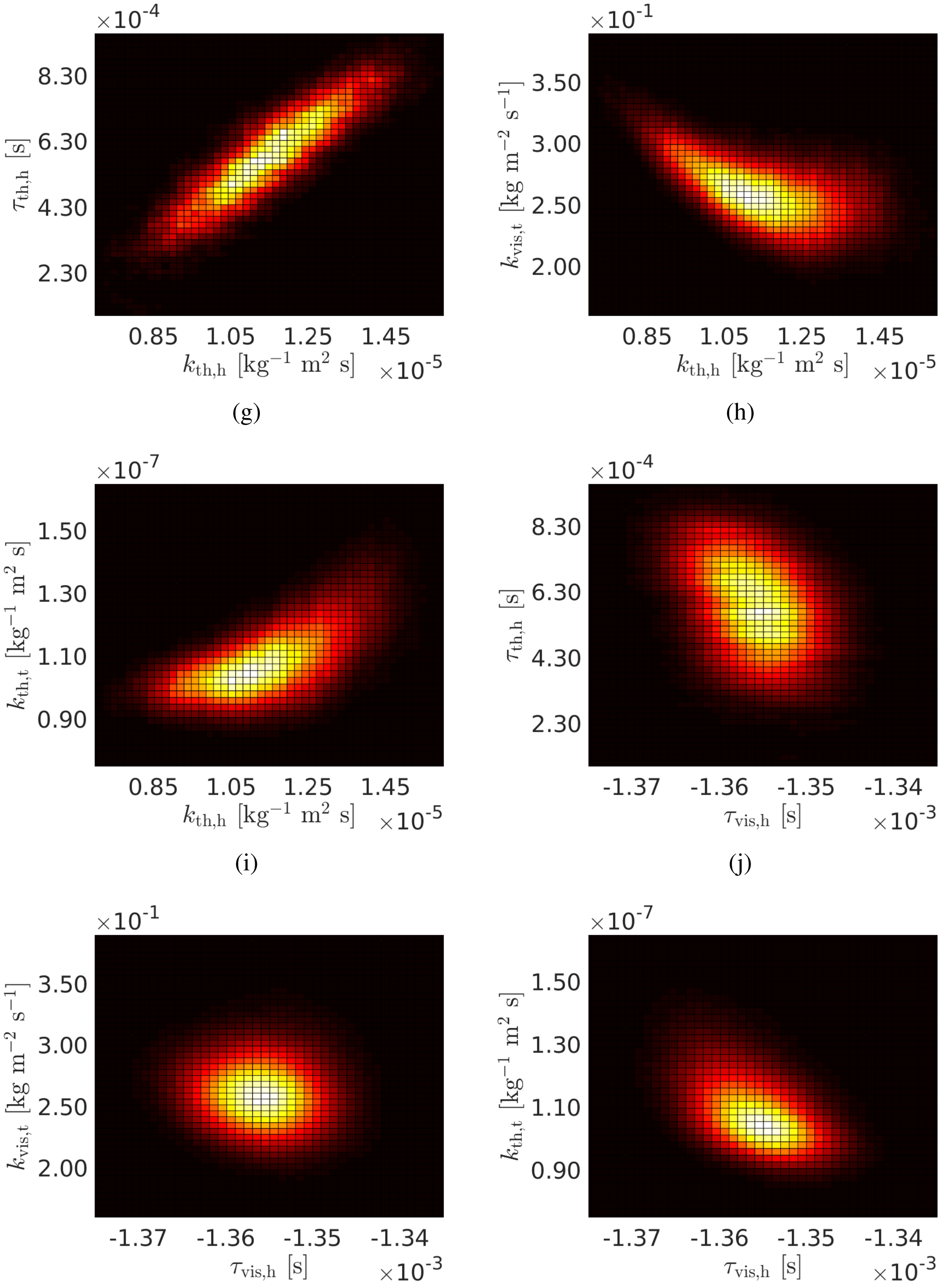
×10-4
8.30
6.30
4.30
2.30
$\tau_{\mathrm{th,h}}$ [s]
0.85 1.05 1.25 1.45
$k_{\mathrm{th,h}}$ [kg^{-1} m^2 s] ×10-5
×10-1
3.50
3.00
2.50
2.00
$k_{\mathrm{vis,t}}$ [kg m^{-2} s^{-1}]
0.85 1.05 1.25 1.45
$k_{\mathrm{th,h}}$ [kg^{-1} m^2 s] ×10-5
×10-7
1.50
1.30
1.10
0.90
$k_{\mathrm{th,t}}$ [kg^{-1} m^2 s]
0.85 1.05 1.25 1.45
$k_{\mathrm{th,h}}$ [kg^{-1} m^2 s] ×10-5
×10-4
8.30
6.30
4.30
2.30
$\tau_{\mathrm{th,h}}$ [s]
-1.37 -1.36 -1.35 -1.34
$\tau_{\mathrm{vis,h}}$ [s] ×10-3
×10-1
3.50
3.00
2.50
2.00
$k_{\mathrm{vis,t}}$ [kg m^{-2} s^{-1}]
-1.37 -1.36 -1.35 -1.34
$\tau_{\mathrm{vis,h}}$ [s] ×10-3
×10-7
1.50
1.30
1.10
0.90
$k_{\mathrm{th,t}}$ [kg^{-1} m^2 s]
-1.37 -1.36 -1.35 -1.34
$\tau_{\mathrm{vis,h}}$ [s] ×10-3

(g) (h)

(i) (j)

(k) (l)

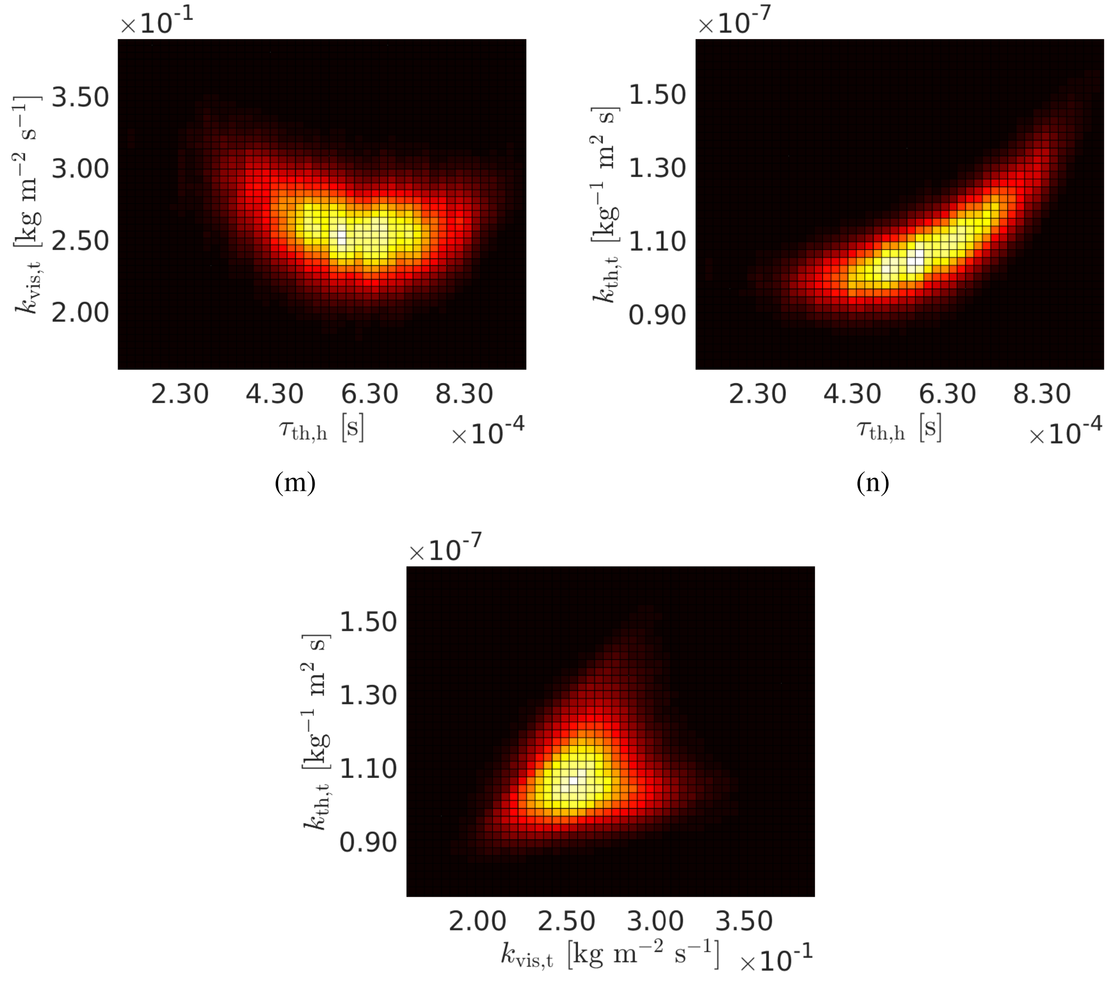

(m)

(n)

(o)

Fig. 4.6 Two-dimensional probability distributions of the heater and thermocouple parameters $\{k_{\mathrm{vis,h}}, k_{\mathrm{th,h}}, \tau_{\mathrm{vis,h}}, \tau_{\mathrm{th,h}}, k_{\mathrm{vis,t}}, k_{\mathrm{th,t}}\}$ obtained with the heater (switched off) and the thermocouples in place.

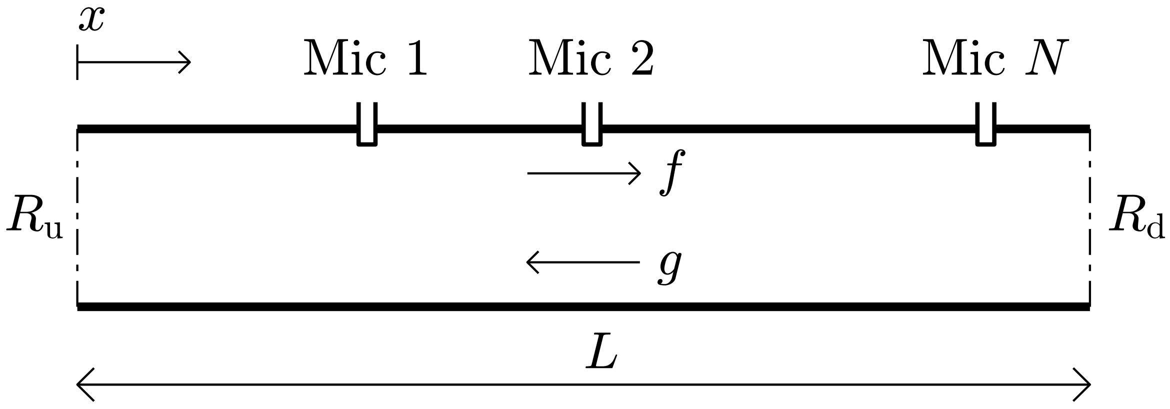

Fig. 4.7 Sketch of an acoustically-excited tube. N different microphones are located at $x_1,\ldots,x_N$. We consider the tube to be a single acoustic element with travelling waves f and g that reflect off the upstream and downstream boundaries characterised by the reflection coefficients R_u and R_d, respectively.

developed by Seybert and Ross [95]. To explain how it works, we assume for the moment that the tube is modelled by a single acoustic element, and that N different microphones are placed at locations $x_1,\ldots,x_N$ (see Fig. 4.7). The pressure fluctuations recorded by each microphone j are given by Eq. (4.18). By taking the Laplace transform of this equation we obtain

$$\hat{P}_j = F\mathrm{e}^{-s\frac{x_j}{\bar{c}}} + G\mathrm{e}^{+s\frac{x_j}{\bar{c}}} \tag{4.47}$$

The left-hand side of Eq. (4.47) is the complex pressure computed in the way described in Sec. 2.3. To solve Eq. (4.47) for $[F,G]^\mathrm{T}$, at least two microphones are needed. If more than two microphones are available, Eq. (4.47) represents an overdetermined linear system of equations, for which $[F,G]^\mathrm{T}$ can be obtained in a more robust way by using least-squares regression. The reflection coefficient at $x = L$ can then be computed using Eq. (4.29):

$$R_\mathrm{d} = \frac{G}{F}\frac{\mathrm{e}^{+s\frac{L}{\bar{c}}}}{\mathrm{e}^{-s\frac{L}{\bar{c}}}} \tag{4.48}$$

If more than one acoustic element is present, one needs to solve the overall network model and, in Eq. (4.48), use the values of F, G, and $\bar{c}$ of the most downstream acoustic element. The difficulty with using Eq. (4.48) is that s needs to be known in order to compute R_d. In order to obtain s, however, one needs to solve Eq. (4.30), which in turn requires knowledge of R_d. This difficulty is overcome by solving for s and R_d simultaneously. The new system of equations to solve is

$$\mathbf{A}(s)\mathbf{w} = \mathbf{p} \tag{4.49}$$

where now $\mathbf{A}(s)$ is no longer square because it contains the right-hand side of Eq. (4.47). These additional rows replace the row where R_d appears, therefore R_d is no longer present in $\mathbf{A}(s)$. Analogously, $\mathbf{p}$ is a vector that contains not only 0, but also the left-hand side of Eq. (4.47). Eq. (4.49) is an overdetermined nonlinear system of equations that is numerically more challenging to solve than Eq. (4.30). We solve Eq. (4.49) iteratively by finding the value of s that minimizes the difference between the left-hand side and the right-hand side of the same equation. For this, we use the Matlab® inbuilt function `lsqnonlin` with the Levenberg-Marquardt algorithm. With the obtained value of s one can compute R_d using Eq. (4.48), if needed. If a microphone is located at the heater position, its signal is discarded when using the MMM.

Given the high sensitivity of s to the boundary conditions and hence to the microphone complex pressures, $\hat{P}_j$, the MMM is a reliable tool only if the microphones are accurately calibrated. In addition to the calibration procedure explained in Sec. 2.3, we further calibrate each microphone against a reference microphone. (This is essentially a relative calibration procedure.) We choose the microphone located at $x_\mathrm{m}/L = 0.45$ to be our reference microphone because it is characterised by the highest signal-to-noise ratio. (Choosing the microphone located at $x_\mathrm{m}/L = 0.55$ would be equivalent, given the symmetry of the first pressure eigenmode.) We then compute for each empty tube experiment the reference pressure eigenmode using the complex pressure of the reference microphone and the empty tube reflection coefficient (these two information uniquely identify the pressure eigenmode). Finally, we compute the calibration coefficient for the generic microphone j as $z_j = \hat{P}_j^\mathrm{ref}/\hat{P}_j$, where $\hat{P}_j^\mathrm{ref}$ is the complex pressure value that lies on the reference pressure eigenmode at $x = x_j$. Multiplying the complex pressure value of each microphone by the corresponding calibration coefficient means, in other words, applying a correction factor that ensures that the complex pressure lies on the reference pressure eigenmode. Once the calibration coefficients are computed, we call the MMM routine using the calibrated complex pressures $(z_j\hat{P}_j)$. Fig. 4.8 shows the values of the calibration coefficients for the empty tube experiments. If the microphones were perfectly calibrated, then $z_j = 1$. However, as can be seen in Fig. 4.8, the calibration coefficients z_j differ from 1 ($z = 1$ holds only for the reference microphone because by definition the complex pressure value of the reference microphone lies on the reference pressure eigenmode). Thus, assuming $z_j = 1$ would lead to less accurate predictions of the complex frequency s.

In Fig. 4.8 it is interesting to note that the clouds of points are not uniformly distributed. Each cloud corresponds to a set of 100 experiments performed after approximately 24 hours. A possible reason of the non-uniformity is a change in the ambient conditions of the lab room (temperature and humidity). Because it would be too complicated to model the dependence of the calibration coefficients upon the ambient conditions, we prefer using for each microphone an average calibration coefficient that varies from day to day, so as to aim to obtain the most accurate results. Thus, for each heater position, we have a set of five calibration coefficients that correspond to the average of each cloud of points in Fig. 4.8. These are reported in Table 4.1. Finally, it is important to notice that, when calling the MMM routine, we discard the information coming from the microphone located at the same position of the heater (if any) because that information would not be accurate. These are highlighted in red in Table 4.1.

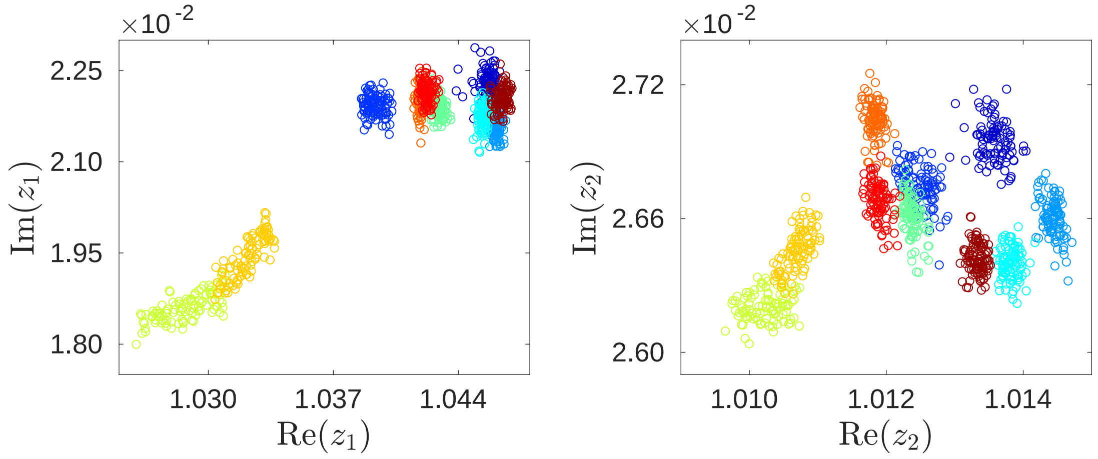

(a) $x_{\mathrm{m}}/L = 0.95$ (b) $x_{\mathrm{m}}/L = 0.85$

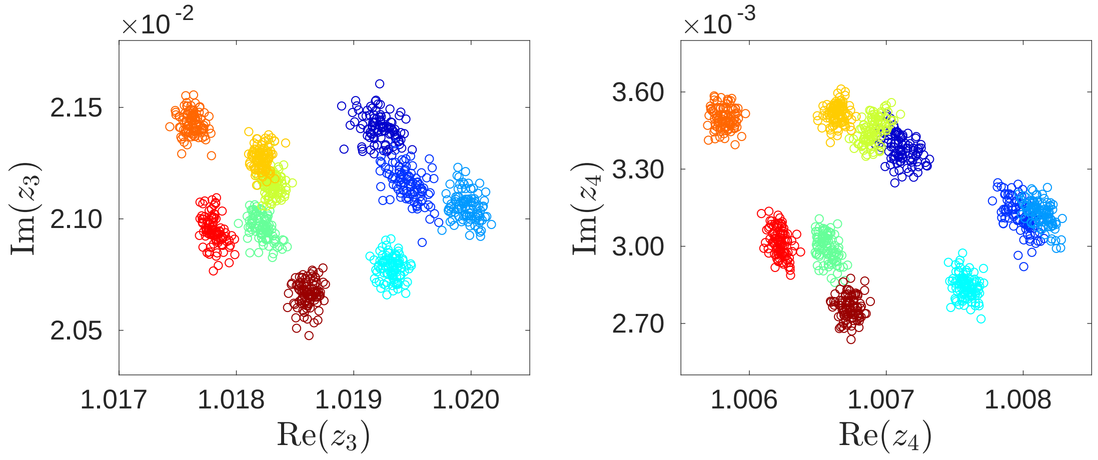

(c) $x_{\mathrm{m}}/L = 0.75$ (d) $x_{\mathrm{m}}/L = 0.65$

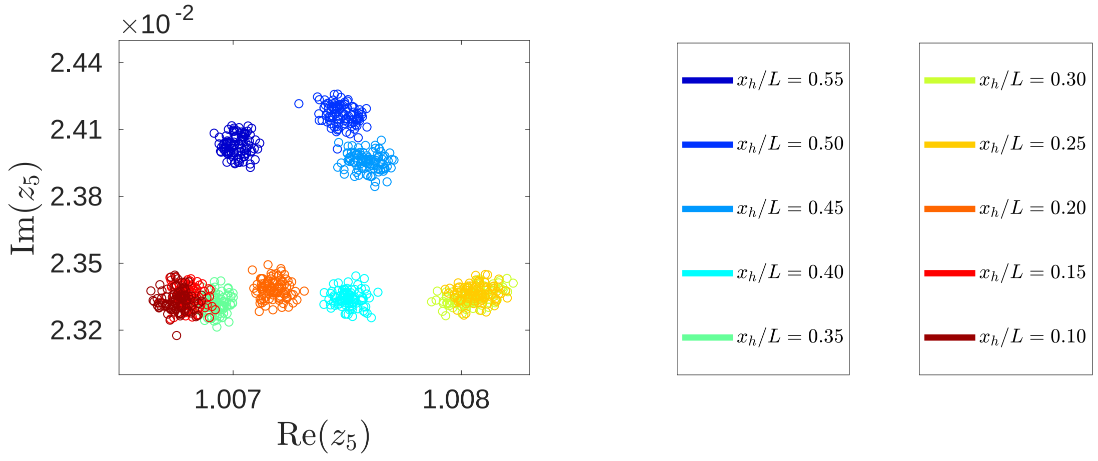

(e) $x_{\mathrm{m}}/L = 0.55$ (f) Legend

Fig. 4.8 Relative calibration coefficients, z_j, of the top 5 microphones. Reference microphone is that at $x_{\mathrm{m}}/L = 0.45$. Different colours represent experiments performed on different days.

Table 4.1 Relative calibration coefficients z_j of each microphone j for each heater position x_h/L. $[z_1,\ z_2,\ z_3,\ z_4,\ z_5,\ z_6]$ are the calibration coefficients of microphones located at $x_\mathrm{m}/L = [0.45,\ 0.55,\ 0.65,\ 0.75,\ 0.85,\ 0.95]$, respectively. The reference microphone is that at $x_\mathrm{h}/L = 0.45$, hence by definition $z_1 = 1$. Information coming from the microphone located at the same position of the heater (if any) is discarded because not accurate: the calibration coefficients of these microphones are reported in red.

x_h/L	z_1	z_2	z_3	z_4	z_5	z_6
0.55	$1.0000 + \mathrm{i}\,0.0000$	$1.0070 + \mathrm{i}\,2.4028 \cdot 10^{-2}$	$1.0071 + \mathrm{i}\,3.3779 \cdot 10^{-3}$	$1.0192 + \mathrm{i}\,2.1405 \cdot 10^{-2}$	$1.0136 + \mathrm{i}\,2.6948 \cdot 10^{-2}$	$1.0456 + \mathrm{i}\,2.2287 \cdot 10^{-2}$
0.50	$1.0000 + \mathrm{i}\,0.0000$	$1.0075 + \mathrm{i}\,2.4168 \cdot 10^{-2}$	$1.0081 + \mathrm{i}\,3.1272 \cdot 10^{-3}$	$1.0195 + \mathrm{i}\,2.1156 \cdot 10^{-2}$	$1.0125 + \mathrm{i}\,2.6749 \cdot 10^{-2}$	$1.0394 + \mathrm{i}\,2.1922 \cdot 10^{-2}$
0.45	$1.0000 + \mathrm{i}\,0.0000$	$1.0076 + \mathrm{i}\,2.3958 \cdot 10^{-2}$	$1.0081 + \mathrm{i}\,3.1272 \cdot 10^{-3}$	$1.0200 + \mathrm{i}\,2.1055 \cdot 10^{-2}$	$1.0144 + \mathrm{i}\,2.6604 \cdot 10^{-2}$	$1.0461 + \mathrm{i}\,2.1602 \cdot 10^{-2}$
0.40	$1.0000 + \mathrm{i}\,0.0000$	$1.0075 + \mathrm{i}\,2.3341 \cdot 10^{-2}$	$1.0076 + \mathrm{i}\,2.8437 \cdot 10^{-3}$	$1.0193 + \mathrm{i}\,2.0780 \cdot 10^{-2}$	$1.0138 + \mathrm{i}\,2.6399 \cdot 10^{-2}$	$1.0454 + \mathrm{i}\,2.1732 \cdot 10^{-2}$
0.35	$1.0000 + \mathrm{i}\,0.0000$	$1.0069 + \mathrm{i}\,2.3318 \cdot 10^{-2}$	$1.0066 + \mathrm{i}\,2.9936 \cdot 10^{-3}$	$1.0182 + \mathrm{i}\,2.0960 \cdot 10^{-2}$	$1.0124 + \mathrm{i}\,2.6611 \cdot 10^{-2}$	$1.0429 + \mathrm{i}\,2.1911 \cdot 10^{-2}$
0.30	$1.0000 + \mathrm{i}\,0.0000$	$1.0080 + \mathrm{i}\,2.3347 \cdot 10^{-2}$	$1.0069 + \mathrm{i}\,3.4513 \cdot 10^{-3}$	$1.0183 + \mathrm{i}\,2.1153 \cdot 10^{-2}$	$1.0102 + \mathrm{i}\,2.6205 \cdot 10^{-2}$	$1.0288 + \mathrm{i}\,1.8605 \cdot 10^{-2}$
0.25	$1.0000 + \mathrm{i}\,0.0000$	$1.0081 + \mathrm{i}\,2.3365 \cdot 10^{-2}$	$1.0066 + \mathrm{i}\,3.5154 \cdot 10^{-3}$	$1.0182 + \mathrm{i}\,2.1272 \cdot 10^{-2}$	$1.0107 + \mathrm{i}\,2.6459 \cdot 10^{-2}$	$1.0322 + \mathrm{i}\,1.9436 \cdot 10^{-2}$
0.20	$1.0000 + \mathrm{i}\,0.0000$	$1.0072 + \mathrm{i}\,2.3385 \cdot 10^{-2}$	$1.0058 + \mathrm{i}\,3.4987 \cdot 10^{-3}$	$1.0176 + \mathrm{i}\,2.1429 \cdot 10^{-2}$	$1.0118 + \mathrm{i}\,2.7045 \cdot 10^{-2}$	$1.0419 + \mathrm{i}\,2.2020 \cdot 10^{-2}$
0.15	$1.0000 + \mathrm{i}\,0.0000$	$1.0068 + \mathrm{i}\,2.3349 \cdot 10^{-2}$	$1.0062 + \mathrm{i}\,3.0155 \cdot 10^{-3}$	$1.0178 + \mathrm{i}\,2.0947 \cdot 10^{-2}$	$1.0119 + \mathrm{i}\,2.6681 \cdot 10^{-2}$	$1.0422 + \mathrm{i}\,2.2150 \cdot 10^{-2}$
0.10	$1.0000 + \mathrm{i}\,0.0000$	$1.0068 + \mathrm{i}\,2.3332 \cdot 10^{-2}$	$1.0067 + \mathrm{i}\,2.7606 \cdot 10^{-3}$	$1.0186 + \mathrm{i}\,2.0665 \cdot 10^{-2}$	$1.0133 + \mathrm{i}\,2.6419 \cdot 10^{-2}$	$1.0465 + \mathrm{i}\,2.2045 \cdot 10^{-2}$

Chapter 5

Thermoacoustic modelling

Building on the results obtained in Chapters 2 to 4, this chapter presents both a qualitative and a quantitative comparison between four different physics-based reduced-order thermoacoustic models. We introduce some flexibility in the models when the underlying physical principles cannot be identified. Each model is trained using a small portion of the data and extrapolation is performed on the remaining data. We show that some frequently-used thermoacoustic models are inadequate to fully describe the entire dataset in our possession, and this occurs even if all the data are used for training. In the first part of this chapter we introduce the models. Next, we use the Markov Chain Monte Carlo method to infer the model parameters. After that, we propagate the uncertainty from the parameters to the state for both the training and the testing data. Finally, we compute the average log-likelihood per datapoint and use this as metric to quantitatively compare the four models and draw conclusions on the best performing model.

5.1 Models description

When the heater is switched on, the right-hand side of Eq. (4.3) becomes non-zero at the heater location

$$\frac{\partial p}{\partial t} + u\frac{\partial p}{\partial x} + \gamma p \frac{\partial u}{\partial x} = (\gamma - 1)\,\delta(x-b)\,\frac{\dot{q}(x,t)}{A} \tag{5.1}$$

where $\frac{\dot{q}(x,t)}{A}$ is the heat release rate per unit area and $\delta(x-b)$ is the Dirac delta function centred at $x = b$. The corresponding jump condition becomes

$$\left[\frac{\gamma}{\gamma-1} p u + \frac{1}{2}\rho u^3\right]_{b^-}^{b^+} = \frac{\dot{q}(b,t)}{A} \tag{5.2}$$

Linearization of Eq. (5.1) translates to

$$\frac{\partial p'}{\partial t} + \gamma \overline{p} \frac{\partial u'}{\partial x} = (\gamma - 1)\, \delta(x - b)\, \dot{q}'(x,t) \tag{5.3}$$

(The second term on the left-hand side of Eq. (5.2) vanishes due to the no mean flow assumption: $\overline{u} = 0$.) This means that, when Eq. (5.3) is integrated across the heater, a new term corresponding to the heat release rate fluctuations appears in the velocity jump condition

$$u'_{i+1}(t) - u'_i(t) = -k_{\mathrm{th,h}}\, p'(t - \tau_{\mathrm{th,h}}) + \frac{\gamma - 1}{\gamma}\, \frac{1}{p}\, \frac{4}{\pi D^2} \dot{q}'_{\mathrm{h}}(t) \tag{5.4}$$

where we set $\dot{q}'_{\mathrm{h}}(t) = \dot{q}'(x_{\mathrm{h}}, t)$ for simplicity. A closure relationship between $\dot{q}'_{\mathrm{h}}(t)$ and the acoustic variables $u'(x,t)$ and $p'(x,t)$ is required, i.e. a heat release rate model needs to be specified. In this study, we compare the performance of four different heat release rate models.

Model 1. The first model is a classic closure relationship provided by the $n - \tau$ model, first introduced by Crocco and Cheng [96]

$$\frac{\dot{q}'_{\mathrm{h}}(t)}{\dot{Q}_{\mathrm{h}}} = n\, \frac{u'_{\mathrm{h}}(t - \tau)}{U_1} \tag{5.5}$$

in which the heat release rate fluctuations are assumed to be proportional to the velocity fluctuations at the heater location through the interaction index n with a time delay τ. Here n and τ are both constant. The time delay τ determines whether the thermoacoustic mechanism drives or damps acoustic oscillations. Thermoacoustic driving occurs when τ is such that $\dot{q}'_{\mathrm{h}}(t)$ is sufficiently in phase with the pressure oscillations $p'(x,t)$. The $n - \tau$ model is a popular thermoacoustic model, used for example by Stow and Dowling [30] within a network model of an annular combustor. Using the Markov Chain Monte Carlo method, we infer n and τ in a probabilistic fashion.

Model 2. The second model represents an extension of model 1 and is based on Lighthill [51], who performed a perturbation analysis on the boundary layer of a laminar flow around a cylinder in cross-flow. We test this model because the electric heater used in our experiments contains several thin cylindrical filaments in cross-flow, each with diameter d_{f} (see Fig. 2.2). The model can be written as:

$$\frac{\dot{q}'_{\mathrm{h}}(t)}{\dot{Q}_{\mathrm{h}}} = n\, \frac{u'_{\mathrm{h}}(t - \tau)}{U_1} \quad , \qquad \tau = k_\tau \frac{0.2 d_{\mathrm{f}}}{U_1} \tag{5.6}$$

In his analysis, Lighthill [51] found a time delay proportionality constant of 0.2, shown above. In our model, we introduce a further dimensionless parameter k_τ to account for possible inaccuracies in this constant. (i.e. Lighthill's value of k_τ would be 1.) With this model, we infer n and k_τ.

Model 3. The third model allows τ to depend on the heater location in order to account for location-dependent flow variations over the heater. We include this effect because τ is the parameter with most influence on the thermoacoustic behaviour, and models 1 and 2 may be unduly restrictive: model 1 assumes that τ is fixed, while model 2 assumes that it is inversely proportional to the natural convection velocity. Nevertheless, having allowed τ to vary, we give it as little flexibility as possible by restricting it to be an affine function of heater location

$$\frac{\dot{q}'_{\mathrm{h}}(t)}{\dot{Q}_{\mathrm{h}}} = n\,\frac{u'_{\mathrm{h}}(t-\tau)}{U_1} \quad , \quad \tau = m_\tau \frac{x_{\mathrm{h}}}{L} + q_\tau \tag{5.7}$$

We therefore infer three parameters, n, m_τ, and q_τ, rather than two.

Model 4. The last model we test represents a variation of model 3 and is based on King's law [97]. The analysis developed by [97] was used by Heckl [98] to investigate nonlinear acoustic effects in a Rijke tube. The difference with model 3 lies in the fact that the interaction index n is now considered to be a function of the Reynolds and Prandtl numbers

$$\frac{\dot{q}'_{\mathrm{h}}(t)}{\dot{Q}_{\mathrm{h}}} = \frac{k_n}{2+(0.5\,\pi\,\mathrm{Pr}\,\mathrm{Re}_1)^{-0.5}}\,\frac{u'_{\mathrm{h}}(t-\tau)}{U_1} \quad , \quad \tau = m_\tau \frac{x_{\mathrm{h}}}{L} + q_\tau \tag{5.8}$$

where $\mathrm{Re}_1 = (d_{\mathrm{f}} U_1)/\nu$ and $\mathrm{Pr} = (\mu c_p)/\lambda$, with fluid properties at ambient conditions, for simplicity. (Evaluating fluid properties at different conditions, for example at the temperature at the heater location, would not change the conclusions of this analysis.) The theoretical value of k_n should be 1, but we allow it to vary to account for possible inaccuracies in this constant. The parameters we aim to infer are therefore k_n, m_τ, and q_τ. We now report the steps needed to deri[illegible]his new equivalent interaction index starting from King's law.

King [97] consider a cylinder in cross-flow. In our case, the cylinder corresponds to one of the many filaments the heater is made up of. Eq. 33 in King [97] reads

$$H = \kappa\theta_0 + 2\sqrt{\pi\kappa s\sigma a}\,U^{\frac{1}{2}}\,\theta_0 \tag{5.9}$$

where H is the heat loss of the cylinder per unit length, θ_0 is the temperature of the cylinder above that of the free stream, κ is the thermal conductivity of the fluid, s is the specific heat capacity per unit mass of the fluid, σ is the density of the fluidy, a is the cylinder radius, and U is the fluid velocity. We assume the fluid properties to be evaluated at the free-stream temperature and the fluid velocity to be the free-stream velocity. Using the cylinder diameter $d_\mathrm{f} = 2a$, we can define a convective heat transfer coefficient h and the corresponding Nusselt number Nu as follows

$$h = \frac{H}{\theta_0 d_\mathrm{f}} \tag{5.10}$$

$$\mathrm{Nu} = \frac{h d_\mathrm{f}}{\kappa} = 1 + 2\sqrt{\frac{\pi}{2}\frac{s\mu}{\kappa}\frac{\sigma d_\mathrm{f} U}{\mu}} = 1 + 2\sqrt{\frac{\pi}{2}}\sqrt{\mathrm{Pr}\,\mathrm{Re}} \tag{5.11}$$

where μ is the dynamic viscosity of the fluid, and Re and Pr are the Reynolds and Prandtl numbers, respectively. Now we consider small perturbations of H, Nu and Re around their mean values, H_0, Nu_0 and Re_0, respectively

$$H = H_0 + d(H) = H_0 + H' \tag{5.12}$$

$$\mathrm{Nu} = \mathrm{Nu}_0 + d(\mathrm{Nu}) = \mathrm{Nu}_0 + \mathrm{Nu}' \tag{5.13}$$

$$\mathrm{Re} = \mathrm{Re}_0 + d(\mathrm{Re}) = \mathrm{Re}_0 + \mathrm{Re}' \tag{5.14}$$

where Re_0 is based on the free-stream velocity U, whereas Re' is based on the perturbed velocity u'. The relation between Nu' and Re' is

$$\mathrm{Nu}' = \left.\frac{d(\mathrm{Nu})}{d(\mathrm{Re})}\right|_{\mathrm{Re}_0} \mathrm{Re}' = \sqrt{\frac{\pi}{2}}\sqrt{\frac{\mathrm{Pr}}{\mathrm{Re}_0}}\mathrm{Re}' \tag{5.15}$$

Finally, the relationship between the heat release rate fluctuations and the velocity perturbations is given by

$$\frac{H'}{H_0} = \frac{\mathrm{Nu}'}{\mathrm{Nu}_0} = \frac{\sqrt{\pi/2}\sqrt{\mathrm{Pr}/\mathrm{Re}_0}}{1 + 2\sqrt{\pi/2}\sqrt{\mathrm{Pr}\,\mathrm{Re}_0}}\mathrm{Re}' = \frac{1}{2 + (0.5\,\pi\,\mathrm{Pr}\,\mathrm{Re}_0)^{-0.5}}\,\frac{u'}{U} \tag{5.16}$$

By replacing U with U_1, and Re_0 with Re_1, and by introducing k_n, we obtain the interaction index shown in Eq. (5.8).

5.2 Qualitative comparison

When the heater is switched on, we build upon the results obtained in the previous chapters. We fix the heater and thermocouple visco-thermal parameters to their mean values obtained in Secs. 4.2 and 4.3, and use the multi-microphone method to compute the downstream reflection coefficient, R_d. The upstream reflection coefficient, R_u, is fixed to the value found in Sec. 4.1. The cold flow parameters could be treated as uncertain parameters and be inferred simultaneously with the thermoacoustic model parameters, but here we fix them to their mean values because, if the thermoacoustic model is wrong, they would compensate for that error by shifting to new values to match the data. In addition, the cold flow parameters are expected to have a lower impact on the results than the thermoacoustic model parameters, so neglecting their uncertainty is reasonable. Here we investigate the thermoacoustic models using only the Markov Chain Monte Carlo method. The training set contains the same heater positions as those used for the cold runs: $x_\mathrm{h}/L = [0.20, 0.25, 0.30]$. The thermoacoustic effect is strongest when the heater is at these positions so these are the best positions at which to infer the parameters of the thermoacoustic model. Similarly to the cold flow case, we infer not only the thermoacoustic model parameters but also σ_DR and σ_f, which are used in the likelihood covariance matrix $\boldsymbol{\sigma}^2_\mathrm{lik}$ to estimate observation and model error. The posterior distribution in the parameter space is obtained following the steps described in Sec. 4.2. The same holds for the uncertainty quantification.

Fig. 5.1 shows the predictions of model 1 at all the heater positions, both training (shaded purple) and testing data. We can see that model 1 performs accurately within the range of the training data but becomes inaccurate when extrapolating beyond the training range. For example, when $x_\mathrm{h}/L = 0.10$, at high powers the growth rate predictions are several standard deviations away from the observations (see top subfigure in Fig. 5.1j). Moreover, even if all the experimental data are used in the training set, the predictions of this model are still poor over the entire range of the data because the thermoacoustic model is not sufficiently flexible. This is not shown here because the results do not differ significantly from Fig. 5.1. Model 2 gives very similar results to model 1 (see Fig. C.1 in Appendix C) because the mean velocity in the tube is similar in all the experiments (see Fig. 3.5). This means that it is not possible to infer a unique set of parameters (either $n-\tau$ in model 1, or $n-k_\tau$ in model 2) that provide accurate results for the whole range of analysed data. These two models can be accurately used only when limiting them to specific configurations where the heater position does not change significantly. In the studies available in the literature, the $n-\tau$ model has been used successfully only because the heater position was fixed. Here instead we show that this thermoacoustic model breaks down when used for a wide range of heater positions.

Model 3 introduces one further model parameter and we find that this gives sufficient flexibility to provide a good fit over the entire testing range. Fig. 5.2 shows the growth rate and frequency predictions of model 3 at every heater position, after training on heater positions $x_\mathrm{h}/L = [0.20, 0.25, 0.30]$ (shaded purple). All the results for the central heater positions are within the 95% confidence interval and, while there is clearly some systematic discrepancy at the extreme heater positions, there is far less than there was for models 1 and 2. Indeed, when $x_\mathrm{h}/L = 0.45$, this model can even replicate the experimental observation

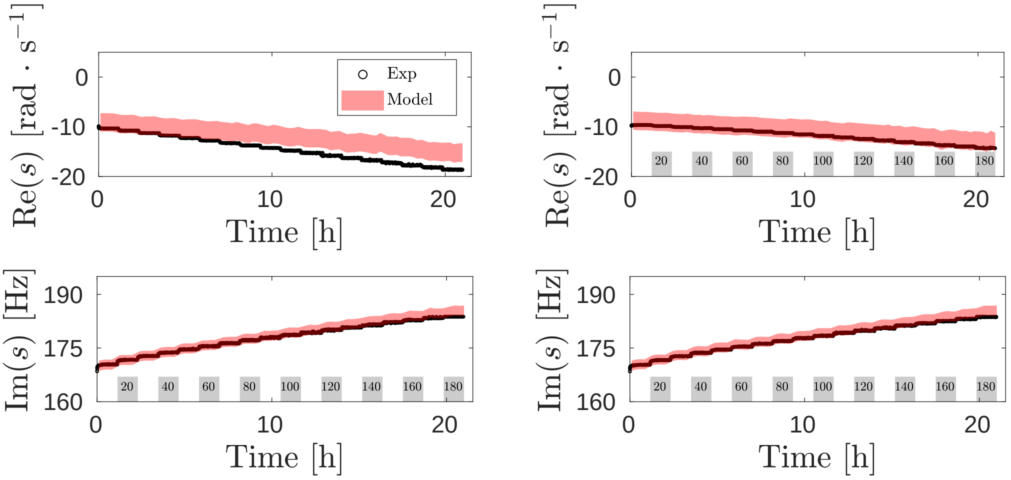

(a) $x_\mathrm{h}/L = 0.55$ (b) $x_\mathrm{h}/L = 0.50$

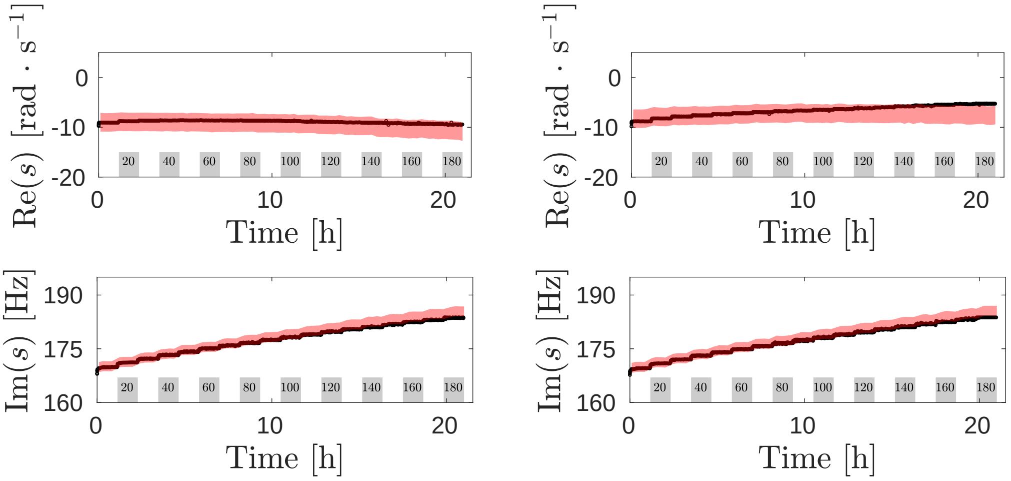

(c) $x_\mathrm{h}/L = 0.45$ (d) $x_\mathrm{h}/L = 0.40$

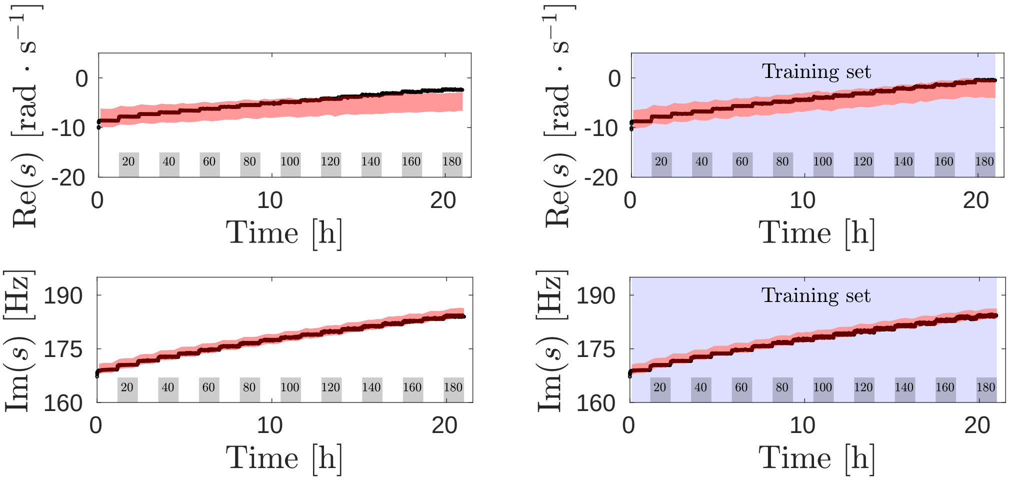

(e) $x_\mathrm{h}/L = 0.35$ (f) $x_\mathrm{h}/L = 0.30$

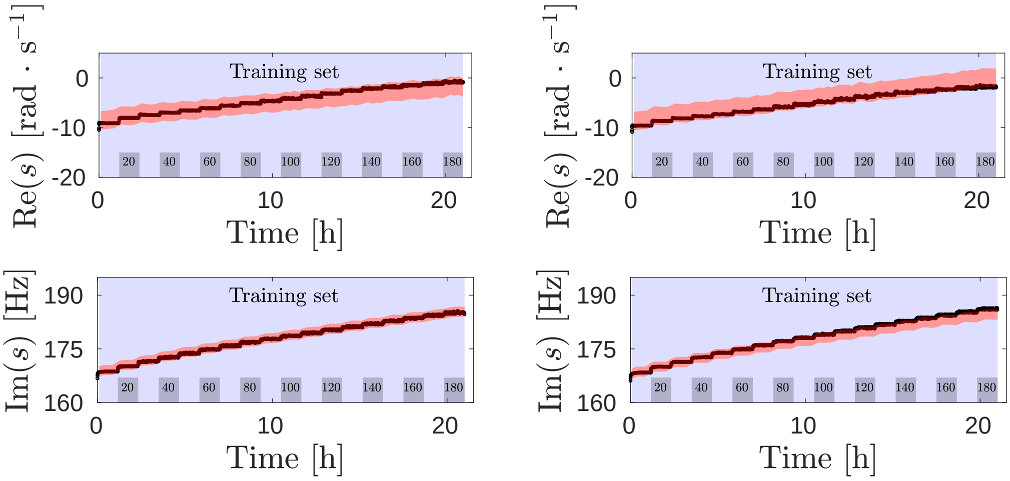

(g) $x_\mathrm{h}/L = 0.25$ (h) $x_\mathrm{h}/L = 0.20$

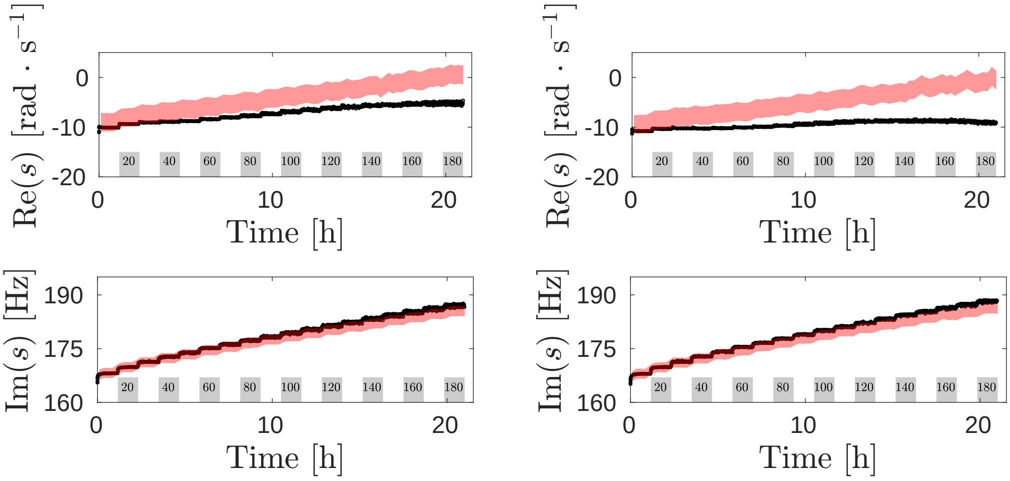

(i) $x_\mathrm{h}/L = 0.15$ (j) $x_\mathrm{h}/L = 0.10$

Fig. 5.1 Comparison between experimental data and predictions of **model 1** with 95% confidence intervals, when the training set comprises experimental data at $x_\mathrm{h}/L = [0.20, 0.25, 0.30]$. The heater power is increased every 70 minutes in steps of 10 W (shown by bars at the bottom).

that the velocity node passes through the heater as the heater power increases (i.e. the growth rate becomes less negative at low heater powers and more negative at high heater powers). Results of model 4 are very similar to those shown in Fig. 5.2 and are reported in Fig. D.1 in Appendix D. This means that the improvement obtained with model 4 is limited as will be shown also in Sec. 5.3.

5.3 Quantitative comparison

As well as the qualitative comparisons shown in Sec. 5.2, the Bayesian methods used here can provide quantitative comparisons of the four models. We evaluate the performance of our models with the average (marginal) log-likelihood per datapoint: a less negative log-likelihood indicates a better performance. This quantity is obtained by marginalizing the model parameters for each datapoint and averaging the resulting likelihoods. This metric is computed just for the testing set in order to provide more robustness to the analysis. The correct computational procedure to do so is reported in Algorithm 5.1. It is important to note that the definition of marginal likelihood involves sampling from the **prior** distribution and then evaluating the likelihood function for each parameter sample. Given that here we are interested only in the testing set, to compute the marginal likelihood in Algorithm 5.1 we sample from the **posterior** parameter distribution (rather than the prior). This is done because we want to evaluate the best possible performance of our models, i.e. we want to use our models once they are calibrated. This is equivalent to stating that, in the definition of the marginal likelihood (see Eq. (1.5)), we replace the original prior distribution with the posterior distribution from the training data and then obtain the marginal likelihood of the testing data.

We show the results of this algorithm in Table 5.1 along with the computation of the root mean square error (RMSE) of growth rate and frequency of each model. The RMSE values are also computed just for the testing set. Table 5.1 shows that model 2 provides a less negative log-likelihood of the testing data than model 1, but a similar RMSE. This means that the average accuracy of the two models is comparable, but the physical model in which τ depends inversely on the mean flow speed (model 2) provides a lower uncertainty, on average, compared to the one in which τ is fixed (model 1). Hence it should be preferred. On the other hand, model 3 provides a less negative log-likelihood of the testing data than both models 1 and 2, so is a better description of the data. It also has a significantly lower RMSE of the growth rate predictions. This comes at the cost of a slight increase in RMSE of the frequency predictions, although this is easily outweighed by the improvement in the growth rate prediction. Table 5.1 therefore quantifies the improvement that can be seen qualitatively

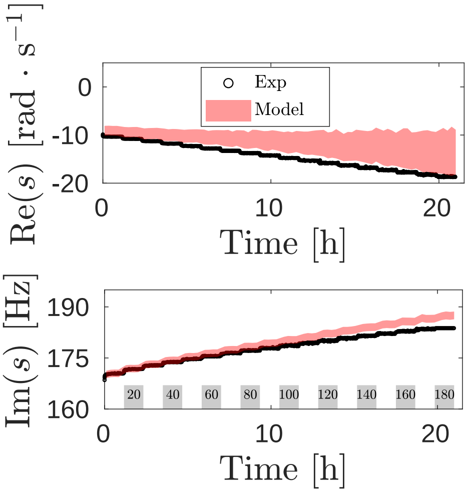

(a) $x_\mathrm{h}/L = 0.55$

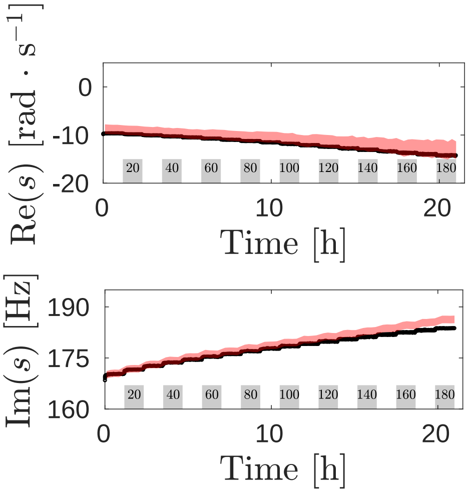

(b) $x_\mathrm{h}/L = 0.50$

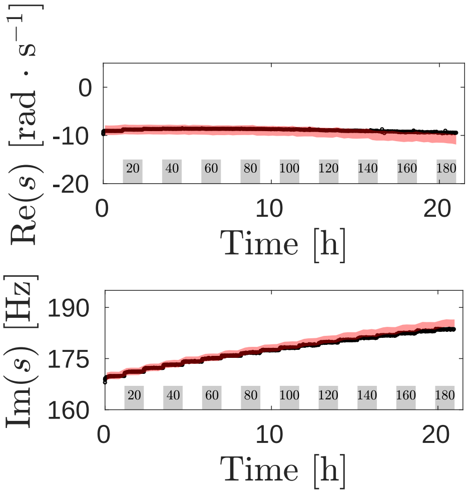

(c) $x_\mathrm{h}/L = 0.45$

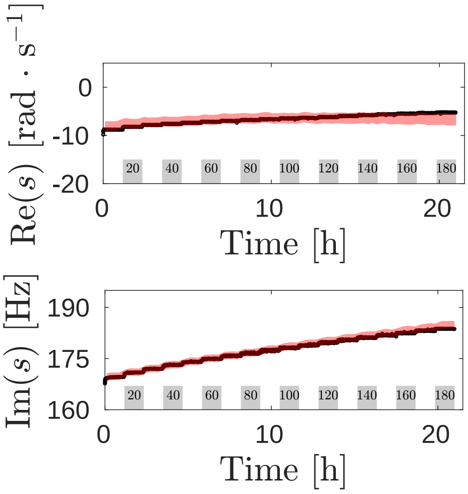

(d) $x_\mathrm{h}/L = 0.40$

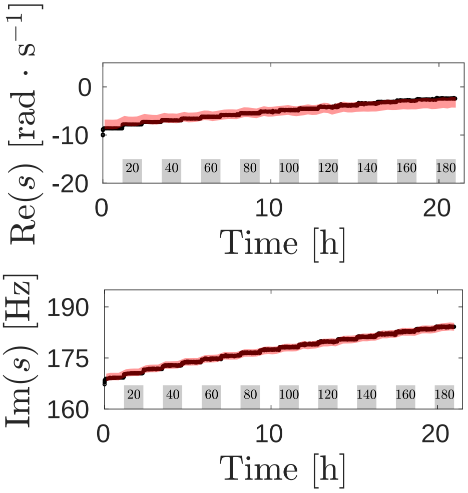

(e) $x_\mathrm{h}/L = 0.35$

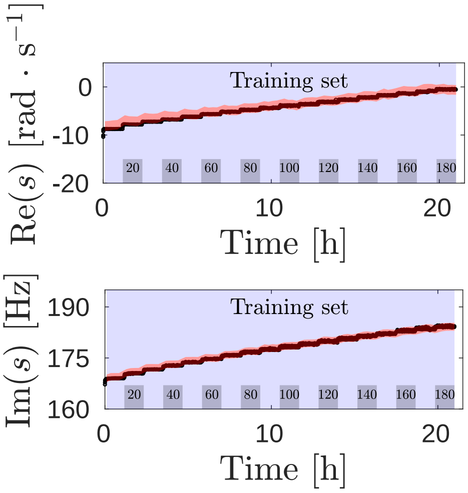

(f) $x_\mathrm{h}/L = 0.30$

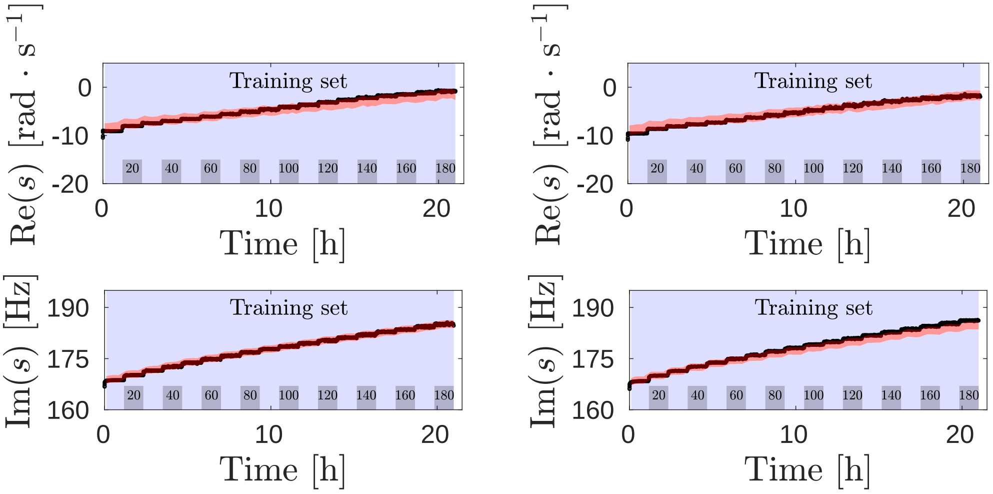

(g) $x_\mathrm{h}/L = 0.25$ (h) $x_\mathrm{h}/L = 0.20$

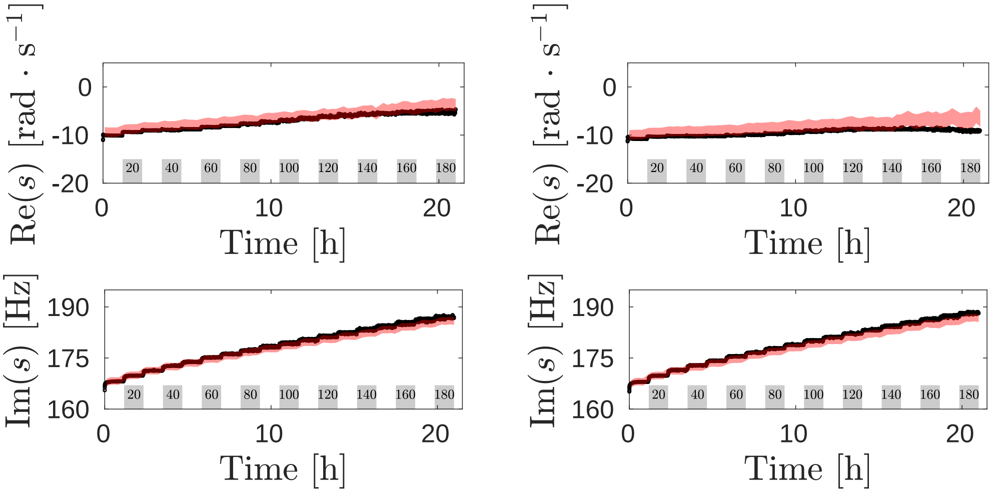

(i) $x_\mathrm{h}/L = 0.15$ (j) $x_\mathrm{h}/L = 0.10$

Fig. 5.2 Comparison between experimental data and predictions of **model 3** with 95% confidence intervals, when the training set comprises experimental data at $x_\mathrm{h}/L = [0.20, 0.25, 0.30]$. The heater power is increased every 70 minutes in steps of 10 W (shown by bars at the bottom).

by comparing Fig. 5.1 with Fig. 5.2. As stated in Sec. 5.2, Model 4 is comparable to model 3, meaning that the interaction index has less influence on the prediction of the growth rate and frequency than does the time delay. Because model 3 is simpler than model 4, it ought to be preferred. In conclusion, this analysis shows that model 3 performs best.

Fig. 5.3 shows the two-dimensional parameter distributions of model 3 obtained with the MCMC. The long thin ellipse in Fig. 5.3c shows that a range of pairs of m_τ and q_τ fit the data reasonably well, reflecting the fact that we are fitting a line through three points at similar values of x_h/L in Eq. (5.7). Had we trained on data from a wider range of x_h/L, the uncertainty in these parameters would have been smaller and the ellipse in Fig. 5.3c would have been more circular.

Algorithm 5.1: Computation of the average log-likelihood per datapoint

```
/* ********************************************************************* */
/* Note:  inside the inner for-loop it is fine to work with likelihoods rather
   than log-likelihoods because the inference has already been done, hence we
   will not face any round-off problems because the model is already close
   enough to the data at this stage */
/* ********************************************************************* */
/* Initialize array of log-likelihoods */
initialize array loglik;
/* Initialize array of likelihoods */
initialize array lik;
foreach experimental datapoint $s_{\mathrm{exp}}$ do
    for $i = 1$ to 500 do
        /* Change the T.A. parameters if you are using a different model */
        $(n,\ m_\tau,\ q_\tau,\ \sigma_{\mathrm{DR}},\ \sigma_{\mathrm{f}}) \leftarrow$ sample from MCMC posterior;
        $s \leftarrow$ use network model $(k_{\mathrm{vis,h}},\ k_{\mathrm{th,h}},\ \tau_{\mathrm{vis,h}},\ \tau_{\mathrm{th,h}},\ n,\ m_\tau,\ q_\tau)$;
        $l \leftarrow$ compute likelihood: $p(s_{\mathrm{exp}}|s, \sigma_{\mathrm{DR}}, \sigma_{\mathrm{f}})$;
        append $l$ to lik;
    end
    /* Compute log of mean likelihood of this experimental datapoint */
    $b \leftarrow$ compute mean of lik and then take the logarithm;
    append $b$ to loglik;
end
/* Compute average log-likelihood per datapoint */
compute mean of loglik;
```

Table 5.1 Average (marginal) log-likelihood per datapoint and RMSE of growth rate, Re(s), and frequency, Im(s), for each model. All these metrics are computed just for the testing set $x_\mathrm{h}/L = [0.10, 0.15, 0.35, 0.40, 0.45, 0.50, 0.55]$. For each row the best results are reported in bold.

	Model 1	Model 2	Model 3	Model 4
Average (marginal) log-likelihood	-6.81	-6.10	**-5.39**	-5.51
RMSE (Re(s)) [rad $\cdot$ s^{-1}]	2.65	2.52	**1.53**	1.62
RMSE (Im(s)) [Hz]	**0.97**	1.01	1.09	1.10

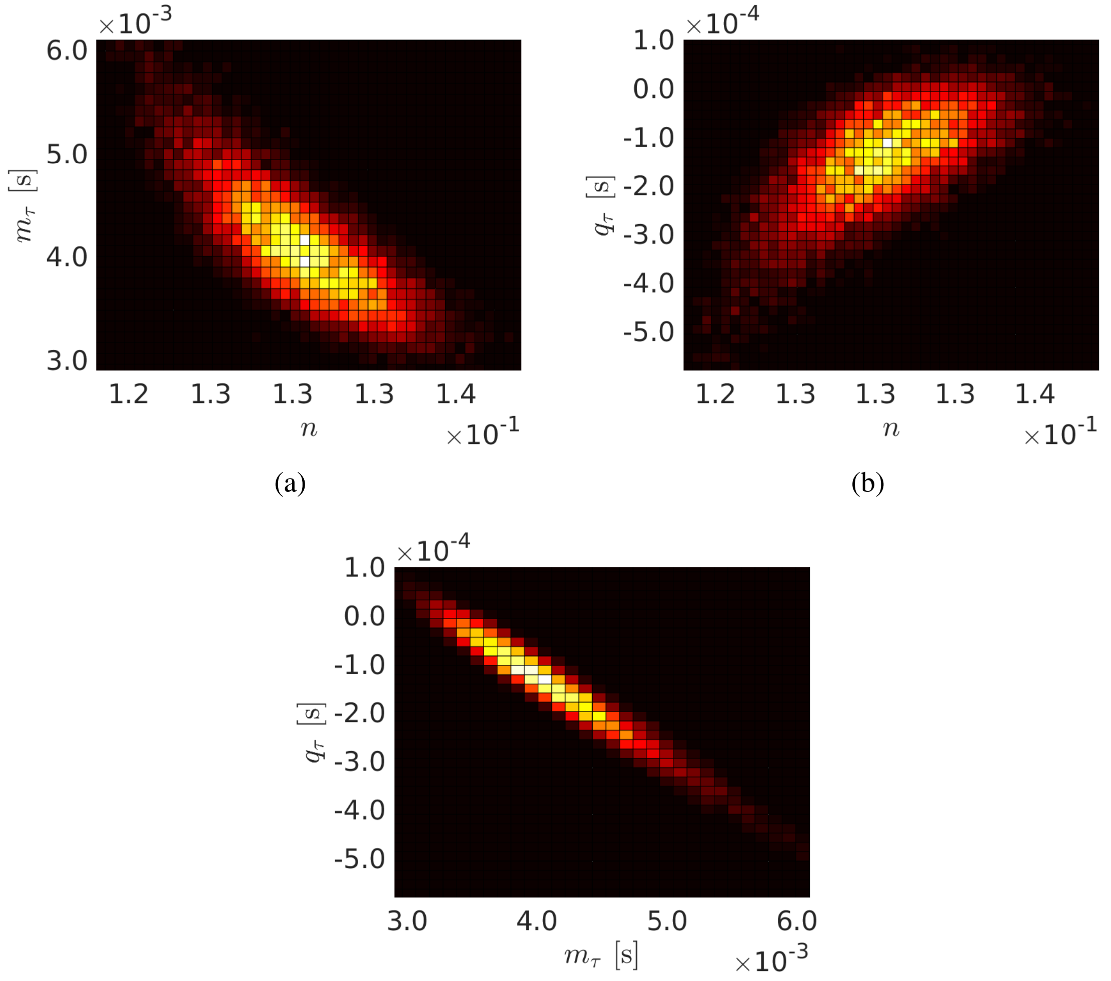

(a)

(b)

(c)

Fig. 5.3 Two-dimensional parameter distributions of **model 3** (best performing model).

Chapter 6

Conclusions

6.1 Summary

In this study, we assimilate $\mathcal{O}(10^6)$ experimental measurements into a physics-based model of a Rijke tube in order to turn a qualitatively-accurate model into a quantitatively-accurate model. The model has two components: (i) a 1D conjugate heat transfer model for the natural convection based flow, into which temperature measurements are assimilated with an ensemble Kalman filter, and (ii) a thermoacoustic network model for the acoustic oscillations, into which microphone pressure measurements are assimilated with the Markov Chain Monte Carlo method. The thermoacoustic experiments are designed so that parameters can be assimilated in sequence, using posterior values from one set of experiments as prior values for subsequent experiments. The cold flow reflection coefficients are inferred first, then the visco-thermal damping coefficients of the cold heater, then the visco-thermal damping coefficient of the thermocouples, and finally the heat release rate parameters, which describe the heat release rate fluctuations as a function of acoustic velocity at the heater. For the hot flow experiments, we use the multi-microphone method to compute the downstream reflection coefficient as it varies with exit temperature.

We show that a simple physics-based model of the cold system, trained on a small portion of the available experiments (27%), describes the experimental results accurately even when extrapolating well beyond the range of the training set (Fig. 4.5). We find that the largest systematic error comes from the heat release rate model. We therefore assimilate the data for four different $n-\tau$ hot heater models: (i) one in which n and τ are fixed; (ii) one in which n is fixed and τ is based on Lighthill's work [51]; (iii) one in which n is fixed and τ is an affine function of the heater position, x_h/L; (iv) one in which n is based on King's law [97] and τ is an affine function of x_h/L. Using the Markov Chain Monte Carlo method, we compute the posterior distribution over the parameter space for each model. With this distribution, using the Monte Carlo method, we marginalize the model parameters and compute the (marginal) log-likelihood of the testing data given each model, as well as the model RMSE on the testing data (Table 5.1). We also plot the model predictions against the experimental data (Figs. 5.1, C.1, 5.2 and D.1). This shows that the third model gives the best fit to the training set (Table 5.1) and can extrapolate well beyond the range of the training set (Fig. 5.2), despite its relatively small size (30%). This model is quantitatively accurate, within quantified error bounds, over all but the most extreme experimental conditions.

This study shows that a physics-based qualititatively-accurate model can be trained to be quantitatively accurate using many experimental measurements and tools from Bayesian statistical inference. Results from this model extrapolate well in the directions in which the physics has been well-described (e.g. changing heater position in the cold experiments). Results extrapolate less well in the directions in which the physics is less well-described (e.g. changing heater position in the hot experiments with model 1). This study reveals that many commonly-used models in thermoacoustics are only qualitatively accurate and need to be adapted to particular configurations in order to become quantitatively accurate. For example, the Levine-Schwinger acoustic reflection coefficient [92], which is derived for a sharp-edged semi-infinite tube in a uniform temperature flow, is not accurate enough for our experiment. Instead we had to measure the reflection coefficients precisely, and adjust the downstream coefficient using the multi-microphone method as the exit temperature increased.

6.2 Future work

This study lies at the boundary between physics and data science: we base our analysis on physical principles and let the data suggest a closure relationship if the identified physical mechanisms are too restrictive. The probabilistic approach used in this study can be applied to a wide variety of physical problems for which the main physical mechanisms are known, allowing modellers to develop quantitatively-accurate models, evaluate their adequacy, and quantify their uncertainty. These quantitatively-accurate models could be used for design, e.g. with adjoint-based optimization algorithms [99], in order to design out thermoacoustic instability. Further, when more elaborate physical models are required in order to characterize more realistic systems, the posteriors of the simpler models can be used as priors for the more elaborate models, as performed here between the cold and hot flow tests. This will allow sophisticated models to be built, with rigorous uncertainty quantification, from their component parts, mirroring the component tests, combustor tests, and full engine tests performed in the gas turbine industry.

In terms of future work strictly related to this thesis, it would be beneficial to perform additional experiments at values of the heater position $x_\mathrm{h}/L > 0.55$. Indeed, only a new experimental campaign can clarify whether the identified relationship between the time delay and the heater position still holds true or not when the switched-on heater is located in the top half of the tube. In addition to this, it would be ideal to test the performance of these models at higher electric powers. The rig under investigation can reach electric powers up to 300 W. At these powers, the system becomes unstable at certain heater positions (e.g. $x_\mathrm{h}/L = 0.25$). When this occurs, one can introduce a phase-shift amplifier in the automation in order to stabilize and unstabilize the system at will, so as to measure the growth rate during the exponentional growth of the instabilities that precedes the limit cycle. Another source of improvement of this work concerns the slow time-scale model and can be achieved by lumping the inner and outer Nusselt numbers into a unique Nusselt number, thus removing the solid temperature from the model. A dependence of the Nusselt number upon the axial coordinate may also be taken into account, if necessary. The improvement of the slow time-scale model may lead to a better interpretability of the model parameters but may not necessarily improve the results significantly, because these are already quite accurate (see Fig. 3.4). Finally, using the statistical learning methods developed throughout this thesi ne can replace the electric heater with a real flame, and perform a similar analysis to what was done in this work. The models used in this thesis can be used as starting point to study a flame Rijke tube. The interest in this is that a flame Rijke tube would reduce the gap with a real rocket engine and would allow modellers to draw interesting conclusions that can be directly applied to an even more realistic system from an industrial point of view, e.g. a lab engine with an annular combustion chamber.

References

[1] F. E. C. Culick. Combustion instabilities in liquid-fueled propulsion systems. Technical report, Advisory Group for Aerospace Research and Development, 1988.

[2] J. C. Oefelein and V. Yang. Comprehensive review of liquid-propellant combustion instabilities in F-1 engines. *Journal of Propulsion and Power*, 9(5):657–677, 1993.

[3] T. C. Lieuwen and V. Yang. *Combustion Instabilities In Gas Turbine Engines: Operational Experience, Fundamental Mechanisms, and Modeling*. Progress in Astronautics and Aeronautics. American Institute of Aeronautics and Astronautics, 2005.

[4] Y. Huang and V. Yang. Dynamics and stability of lean-premixed swirl-stabilized combustion. *Progress in Energy and Combustion Science*, 35(4):293 – 364, 2009.

[5] S. M. Candel. Combustion instabilities coupled by pressure waves and their active control. *Symposium (International) on Combustion*, 24(1), 1992.

[6] S. M. Candel. Combustion dynamics and control: progress and challenges. *Proceedings of the Combustion Institute*, 29(1):1–28, 2002.

[7] M. P. Juniper and R. I. Sujith. Sensitivity and nonlinearity of thermoacoustic oscillations. *Annual Review of Fluid Mechanics*, 50(1):661–689, 2018.

[8] B. Higgins. On the sound produced by a current of hydrogen gas passing through a tube. *Journal of Natural Philosophy, Chemistry and the Arts*, 1:129–131, 1802.

[9] J. W. Rayleigh. The explanation of certain acoustical phenomena. *Nature*, 18(455): 319–321, July 1878.

[10] A. A. Putnam and W. R. Dennis. Burner oscillations of the gauze-tone type. *The Journal of the Acoustical Society of America*, 26(5):716–725, September 1954.

[11] B. Chu. On the energy transfer to small disturbances in fluid flow (part i). *Acta Mechanica*, 1(3):215–234, September 1965.

[12] F. Nicoud and T. Poinsot. Thermoacoustic instabilities: Should the Rayleigh criterion be extended to include entropy changes? *Combustion and Flame*, 142:153–159, July 2005.

[13] L. Magri, M. P. Juniper, and J. P. Moeck. Sensitivity of the Rayleigh criterion in thermoacoustics. *Journal of Fluid Mechanics*, 882(R1), January 2020.

[14] L. Crocco. Research on combustion instability in liquid propellant rockets. *Symposium (International) on Combustion*, 12(1):85 – 99, 1969.

[15] F. E. C. Culick. Unsteady motions in combustion chambers for propulsion systems. Technical Report AG-AVT-039, NATO Research and Technology Organisation, December 2006.

[16] S. Bade, M. Wagner, C. Hirsch, T. Sattelmayer, and B. Schuermans. Design for thermoacoustic stability: Modeling of burner and flame dynamics. *J. Eng. Gas Turbines Power*, 135(11):111502, 2013.

[17] H. C. Mongia, T. J. Held, G. C. Hsiao, and R. P. Pandalai. Challenges and progress in controlling dynamics in gas turbine combustors. *Journal of Propulsion and Power*, 19 (5):822–829, 2003.

[18] L. Y. M. Gicquel, G. Staffelbach, and T. Poinsot. Large Eddy Simulations of gaseous flames in gas turbine combustion chambers. *Progress in Energy and Combustion Science*, 38(6):782–817, 2012.

[19] H. Pitsch. Large-Eddy Simulation of turbulent combustion. *Annual Review of Fluid Mechanics*, 38(1):453–482, 2006.

[20] P. Jordan and T. Colonius. Wave packets and turbulent jet noise. *Annual Review of Fluid Mechanics*, 45(1):173–195, 2013.

[21] M. S. Dodd and A. Ferrante. On the interaction of taylor length scale size droplets and isotropic turbulence. *Journal of Fluid Mechanics*, 806:356–412, 2016.

[22] G. A. Brès, F. E. Ham, J. W. Nichols, and S. K. Lele. Unstructured Large-Eddy Simulations of supersonic jets. *AIAA Journal*, 55(4):1164–1184, 2017.

[23] S. Elghobashi. Direct Numerical Simulation of turbulent flows laden with droplets or bubbles. *Annual Review of Fluid Mechanics*, 51(1):217–244, 2019.

[24] M. Ihme. Combustion and engine-core noise. *Annual Review of Fluid Mechanics*, 49 (1):277–310, 2017.

[25] C. A. Armitage, R. Balachandran, E. Mastorakos, and R. S. Cant. Investigation of the nonlinear response of turbulent premixed flames to imposed inlet velocity oscillations. *Combustion and Flame*, 146(3):419–436, 2006.

[26] X. Han and A. S. Morgans. Simulation of the flame describing function of a turbulent premixed flame using an open-source les solver. *Combustion and Flame*, 162(5): 1778–1792, 2015.

[27] L. Selle, G. Lartigue, T. Poinsot, R. Koch, K.-U. Schildmacher, W. Krebs, B. Prade, P. Kaufmann, and D. Veynante. Compressible large eddy simulation of turbulent combustion in complex geometry on unstructured meshes. *Combustion and Flame*, 137 (4):489 – 505, 2004.

[28] G. Staffelbach, L.Y.M. Gicquel, G. Boudier, and T. Poinsot. Large Eddy Simulation of self excited azimuthal modes in annular combustors. *Proceedings of the Combustion Institute*, 32(2):2909–2916, 2009.

[29] A. Giusti and E. Mastorakos. Turbulent combustion modelling and experiments: Recent trends and developments. *Flow, Turbulence and Combustion*, 103(4):847–869, 2019.

[30] S. R. Stow and A. P. Dowling. Thermoacoustic oscillations in an annular combustor. *Proceedings of the ASME Turbo Expo: Power for Land, Sea, and Air*, 2(V002T02A004), June 2001.

[31] J. G. Aguilar, L. Magri, and M. P. Juniper. Adjoint-based sensitivity analysis of low-order thermoacoustic networks using a wave-based approach. *Journal of Computational Physics*, 341:163 – 181, 2017.

[32] A. Witte. *Dynamics of Unsteady Heat Transfer and Skin Friction in Pulsating Flow Across a Cylinder*. PhD thesis, TU Munich, 2018.

[33] M. Summerfield. A theory of unstable combustion in liquid propellant rocket systems. *Journal of the American Rocket Society*, 21(5):108–114, September 1951.

[34] W. A. Sirignano. Driving mechanisms for combustion instability. *Combustion Science and Technology*, 187(1-2):162–205, 2015.

[35] F. Selimefendigil, S. Föller, and W. Polifke. Nonlinear identification of unsteady heat transfer of a cylinder in pulsating cross flow. *Computers & Fluids*, 53:1–14, 2012.

[36] P. R. Alemela, D. Fanaca, C. Hirsch, T. Sattelmayer, and B. Schuermans. Determination and scaling of thermo acoustic characteristics of premixed flames. *International Journal of Spray and Combustion Dynamics*, 2(2):169–198, 2010.

[37] M. A. Heckl. Active control of the noise from a rijke tube. *Journal of Sound and Vibration*, 124(1):117–133, 1988.

[38] T. Poinsot and D. Veynante. *Theoretical and Numerical Combustion*. 3rd edition, 2012.

[39] S. Ducruix, D. Durox, and S. Candel. Theoretical and experimental determinations of the transfer function of a laminar premixed flame. *Proceedings of the Combustion Institute*, 28(1):765–773, 2000. ISSN 1540-7489.

[40] T. Schuller, S. Ducruix, D. Durox, and S. Candel. Modeling tools for the prediction of premixed flame transfer functions. *Proceedings of the Combustion Institute*, 29(1): 107–113, 2002. ISSN 1540-7489. Proceedings of the Combustion Institute.

[41] T. Schuller, D. Durox, and S. Candel. A unified model for the prediction of laminar flame transfer functions: comparisons between conical and V-flame dynamics. *Combustion and Flame*, 134(1):21–34, 2003. ISSN 0010-2180.

[42] A. P. Dowling. Nonlinear self-excited oscillations of a ducted flame. *Journal of Fluid Mechanics*, 346:271–290, 1997.

[43] A. P. Dowling. A kinematic model of a ducted flame. *Journal of Fluid Mechanics*, 394: 51–72, 1999.

[44] A. S. Morgans and S. R. Stow. Model-based control of combustion instabilities in annular combustors. *Combustion and Flame*, 150(4):380–399, 2007. ISSN 0010-2180.

[45] N. Noiray, D. Durox, T. Schuller, and S. Candel. A unified framework for nonlinear combustion instability analysis based on the flame describing function. *Journal of Fluid Mechanics*, 615:139–167, 2008.

[46] D. Durox, T. Schuller, N. Noiray, and S. Candel. Experimental analysis of nonlinear flame transfer functions for different flame geometries. *Proceedings of the Combustion Institute*, 32(1):1391–1398, 2009. ISSN 1540-7489.

[47] N. P. Jamieson and M. P. Juniper. Experimental sensitivity analysis of a linearly stable thermoacoustic system via a pulsed forcing technique. *Experiments in Fluids*, 58(9): 123, August 2017.

[48] M. P. Juniper. Obtaining thermoacoustic eigenvalue sensitivities with adjoint methods. *Annual Review of Fluid Mechanics (supplementary materials)*, 50:661–689, 2018.

[49] P. L. Rijke. On the vibration of the air in a tube open at both ends. *Philosophical Magazine*, 17(116):419–422, 1859.

[50] S.W. Rienstra and A. Hirschberg. *An Introduction to Acoustics*. Eindhoven University of Technology, 2004.

[51] M. J. Lighthill. The response of laminar skin friction and heat transfer to fluctuations in the stream velocity. *Proceedings of the Royal Society of London A: Mathematical, Physical and Engineering Sciences*, 224(1156):1–23, 1954.

[52] T. Saito. Vibrations of air-columns excited by heat supply. *The Japan Society of Mechanical Engineers*, 8(32):651–659, 1965.

[53] P. G. Drazin. *Introduction to Hydrodynamic Stability*. Cambridge University Press, Cambridge, 2002.

[54] I. Gertsbakh. *Measurement Theory for Engineers*. Springer-Verlag Berlin Heidelberg, 2003.

[55] D. J. C. MacKay. *Information Theory, Inference, and Learning Algorithms*. Cambridge University Press, 2003.

[56] A. Tarantola. *Inverse Problem Theory and Methods for Model Parameter Estimation*. SIAM: Society for Industrial and Applied Mathematics, 1st edition, 2005.

[57] G. Evensen. *Data Assimilation - The Ensemble Kalman Filter*. Springer-Verlag Berlin Heidelberg, 2nd edition, 2009.

[58] A. Gelman, J. B. Carlin, H. S. Stern, D. B. Dunson, A. Vehtari, and D. B. Rubin. *Bayesian Data Analysis*. CRC Press, 3rd edition, 2013.

[59] A. F. Bennett. *Inverse Methods in Physical Oceanography*. Cambridge University Press, 1992.

[60] A. F. Bennett. *Inverse Modeling of the Ocean and Atmosphere*. Cambridge University Press, 2002.

[61] H. Kato, A. Yoshizawa, G. Ueno, and S. Obayashi. A data assimilation methodology for reconstructing turbulent flows around aircraft. *Journal of Computational Physics*, 283:559 – 581, 2015. ISSN 0021-9991.

[62] V. Mons, J. C. Chassaing, and P. Sagaut. Optimal sensor placement for variational data assimilation of unsteady flows past a rotationally oscillating cylinder. *Journal of Fluid Mechanics*, 823:230–277, 2017.

[63] D. P. G. Foures, N. Dovetta, D. Sipp, and P. J. Schmid. A data-assimilation method for Reynolds-averaged Navier-Stokes-driven mean flow reconstruction. *Journal of Fluid Mechanics*, 759:404–431, 2014.

[64] D. Darakananda, J. Eldredge, A. da Silva, T. Colonius, and D. R. Williams. EnKF-based dynamic estimation of separated flows with a low-order vortex model. *AIAA Paper No. 2018–0811*, 2018.

[65] H. Yu, T. Jaravel, M. Ihme, M. P. Juniper, and L. Magri. Data assimilation and optimal calibration in nonlinear models of flame dynamics. *Journal of Engineering for Gas Turbines and Power*, (GTP-19-1369), 2019.

[66] H. Yu, M. P. Juniper, and L. Magri. A data-driven kinematic model of a ducted premixed flame. *Proceedings of the Combustion Institute*, 2020. ISSN 1540-7489.

[67] J. W. Labahn, H. Wu, B. Coriton, J. H. Frank, and M. Ihme. Data assimilation using high-speed measurements and LES to examine local extinction events in turbulent flames. *Proceedings of the Combustion Institute*, 37(2):2259 – 2266, 2019.

[68] U. Sengupta, M. L. Croci, and M. P. Juniper. Real-time parameter inference in reduced-order flame models with heteroscedastic Bayesian neural network ensembles. *Machine Learning and the Physical Sciences Workshop at the 34th Conference on Neural Information Processing Systems (NeurIPS)*, 2020.

[69] S. Guo, C. F. Silva, K. J. Yong, and W. Polifke. A Gaussian-process-based framework for high-dimensional uncertainty quantification analysis in thermoacoustic instability predictions. *Proceedings of the Combustion Institute*, 2020. ISSN 1540-7489.

[70] C.F. Silva, P. Pettersson, G. Iaccarino, and M. Ihme. Uncertainty quantification of combustion noise by generalized polynomial chaos and state-space models. *Combustion and Flame*, 217:113 – 130, 2020.

[71] A. Avdonin, S. Jaensch, C. F. Silva, M. Češnovar, and W. Polifke. Uncertainty quantification and sensitivity analysis of thermoacoustic stability with non-intrusive polynomial chaos expansion. *Combustion and Flame*, 189:300 – 310, 2018.

[72] L. Magri, J. O'Brien, and M. Ihme. Compositional inhomogeneities as a source of indirect combustion noise. *Journal of Fluid Mechanics*, 799:R4, 2016.

[73] A. Ghani, I. Boxx, and C. Noren. Data-driven identification of nonlinear flame models. *J. Eng. Gas Turbines Power*, 142(12), December 2020. ISSN 0742-4795.

[74] K. I. Matveev. *Thermoacoustic instabilities in the Rijke tube: experiments and modeling*. PhD thesis, California Institute of Technology, 2003.

[75] T. Poinsot. Prediction and control of combustion instabilities in real engines. *Proceedings of the Combustion Institute*, 36(1):1 – 28, 2017. ISSN 1540-7489.

[76] H. Yu. *Inverse problems in thermoacoustics*. PhD thesis, University of Cambridge, August 2020.

[77] A. Gelman and D. B. Rubin. Inference from iterative simulation using multiple sequences. *Statistical Science*, 7(4):457–472, 1992.

[78] M. D. Hoffman and A. Gelman. The no-u-turn sampler: Adaptively setting path lengths in hamiltonian monte carlo. *Journal of Machine Learning Research*, 2014.

[79] N. P. Jamieson, G. Rigas, and M. P. Juniper. Experimental sensitivity analysis via a secondary heat source in an oscillating thermoacoustic system. *International Journal of Spray and Combustion Dynamics*, 9(4):230–240, 2017.

[80] N. P. Jamieson and M. P. Juniper. Experimental sensitivity analysis and the equivalence of pulsed forcing and feedback control in thermoacoustic systems. *Proceedings of ASME Turbo Expo*, June 2017.

[81] G. Rigas, N. P. Jamieson, L. K. B. Li, and M. P. Juniper. Experimental sensitivity analysis and control of thermoacoustic systems. *Journal of Fluid Mechanics*, 787:R1, 2016.

[82] F. Garita. Experimental Dataset for "Statistical Learning of Acoustic and Thermoacoustic Model Parameters of a Rijke Tube Using Bayesian Inference". *Apollo*, 2021.

[83] J. H. Ferziger and M. Peric. *Computational Methods for Fluid Dynamics*, chapter 3, pages 39–69. Springer-Verlag Berlin Heidelberg, 3rd edition, 2002.

[84] B. Fornberg. Generation of finite difference formulas on arbitrarily spaced grids. *Mathematics of Computation*, 51(184):699–706, October 1988.

[85] B. Fornberg. Calculation of weights in finite difference formulas. *SIAM Review*, 40(3): 685–691, September 1998.

[86] A. P. Dowling. The calculation of thermoacoustic oscillations. *Journal of Sound and Vibration*, 180(4):557 – 581, 1995.

[87] J. Li and A. S. Morgans. The one-dimensional acoustic field in a duct with arbitrary mean axial temperature gradient and mean flow. *Journal of Sound and Vibration*, 400: 248 – 269, 2017.

[88] F. Nicoud and K. Wieczorek. About the zero mach number assumption in the calculation of thermoacoustic instabilities. *International Journal of Spray and Combustion Dynamics*, 1(1):67–112, November 2009.

[89] F. E. Marble and S. M. Candel. Acoustic disturbance from gas non-uniformities convected through a nozzle. *Journal of Sound and Vibration*, 55(2):225–243, 1977.

[90] N. A. Cumpsty. Jet engine combustion noise: Pressure, entropy and vorticity perturbations produced by unsteady combustion or heat addition. *Journal of Sound and Vibration*, 66(4):527–544, 1979.

[91] M. P. Juniper. Sensitivity analysis of thermoacoustic instability with adjoint helmholtz solvers. *Phys. Rev. Fluids*, 3:110509, Nov 2018.

[92] H. Levine and J. Schwinger. On the radiation of sound from an unflanged circular pipe. *Physical Review*, 73(4):383 – 406, 1948.

[93] A. Cummings. High temperature effects on the radiation impedance of an unflanged duct exit. *Journal of Sound and Vibration*, 52(2):299 – 304, 1977.

[94] H. Rämmal and J. Lavrentjev. Sound reflection at an open end of a circular duct exhausting hot gas. *Noise Control Engineering Journal*, 56(2):107–114, 2008.

[95] A. F. Seybert and D. F. Ross. Experimental determination of acoustic properties using a two-microphone random-excitation technique. *The Journal of the Acoustical Society of America*, 61(5):1362–1370, May 1977.

[96] L. Crocco and S. I. Cheng. *Theory of Combustion Instability in Liquid Propellant Rocket Motors*. Butterworths, London, 1956.

[97] L. V. King. On the convection of heat from small cylinders in a stream of fluid: Determination of the convection constants of small platinum wires with applications to hot-wire anemometry. *Philosophical Transactions of the Royal Society of London*, 1914.

[98] M. A. Heckl. Non-linear acoustic effects in the rijke tube. *Acustica*, 72:63–71, April 1990.

[99] J. G. Aguilar and M. P. Juniper. Thermoacoustic stabilization of a longitudinal combustor using adjoint methods. *Phys. Rev. Fluids*, 5:083902, August 2020.

Appendix A

Complex frequency and pressures from experiments (Matlab script)

```
function [s_exp, p_exp] = ...
fun_DecayRate(f_exc, Fs, mic, V, lower_lim, upper_lim)

% Calibration coefficients: [frequency, decibels]
cc1 = load('calibrationData\263705.dat'); % x_m/L = 0.95
cc2 = load('calibrationData\263706.dat'); % x_m/L = 0.85
cc3 = load('calibrationData\263707.dat'); % x_m/L = 0.75
cc4 = load('calibrationData\263703.dat'); % x_m/L = 0.65
cc5 = load('calibrationData\263702.dat'); % x_m/L = 0.55

% Microphone sensitivities
V_to_Pa_1 = 2.99/1000; % x_m/L = 0.95
V_to_Pa_2 = 2.95/1000; % x_m/L = 0.85
V_to_Pa_3 = 2.85/1000; % x_m/L = 0.75
V_to_Pa_4 = 3.02/1000; % x_m/L = 0.65
V_to_Pa_5 = 2.80/1000; % x_m/L = 0.55

% Apply calibration coefficients and convert voltage
% fluctuations into pressure fluctuations
switch(mic)
    case{1} % x_m/L = 0.95
        V = V - mean(V);
        V = ...
        V/10^(0.05*interp1(cc1(:,1), cc1(:,2), f_exc));
        p_raw = V/V_to_Pa_1;
    case{2} % x_m/L = 0.85
        V = V - mean(V);
        V = ...
        V/10^(0.05*interp1(cc2(:,1), cc2(:,2), f_exc));
        p_raw = V/V_to_Pa_2;
    case{3} % x_m/L = 0.75
        V = V - mean(V);
        V = ...
        V/10^(0.05*interp1(cc3(:,1), cc3(:,2), f_exc));
        p_raw = V/V_to_Pa_3;
    case{4} % x_m/L = 0.65
        V = V - mean(V);
        V = ...
        V/10^(0.05*interp1(cc4(:,1), cc4(:,2), f_exc));
        p_raw = V/V_to_Pa_4;
    case{5} % x_m/L = 0.55
        V = V - mean(V);
        V = ...
        V/10^(0.05*interp1(cc5(:,1), cc5(:,2), f_exc));
        p_raw = V/V_to_Pa_5;
end

% Apply a Butterworth filter to remove too high/low
% frequencies
Fc  = f_exc; % center frequency
dFc = 25;    % delta F
[B,A] = butter(3,[Fc-dFc Fc+dFc]/(Fs/2),'bandpass');
p_raw = filtfilt(B, A, p_raw);

% Compute Fast Fourier Transform
ndata = length(p_raw);
NFFT = 2^nextpow2(ndata);

% Compute frequency domain. The highest captured frequency
% is Fs/2. Above this, frequencies are aliased
f = Fs/2*linspace(0,1,NFFT/2+1);
dt = 1/Fs;

% Compute the Fourier transform in the two-sided spectrum
p_FFT = fft(p_raw, NFFT)*dt;
p_FFT = p_FFT(1:NFFT/2+1);
p_FFT(2:end-1) = 2*p_FFT(2:end-1);
freq = f(find(abs(p_FFT) == max(abs(p_FFT))));

% Calculate Hilbert Transform (Fs = 1/dt)
Philb = hilbert(p_raw);
Hampl = abs(Philb);
Hphase = unwrap(angle(Philb));
Hfreq = diff(unwrap([Hphase; Hphase(end)]))*Fs/(2*pi);

% Fit a straight line to the decaying part
N = length(p_raw);
t = [0:N-1]./Fs; t = t';
coeff = polyfit(...
            t(t>lower_lim & t<upper_lim), ...
            log(Hampl(t>lower_lim & t<upper_lim)),1 ...
              );

% Compute experimental complex frequency
% s_exp = decay_rate + i*frequency
s_exp = coeff(1) + 1i*freq;

% Compute experimental complex pressure
p_exp = p_FFT(abs(p_FFT) == max(abs(p_FFT)));

end
```

Appendix B

Slow time-scale model (Matlab script)

```matlab
function [T, U] = fun_conj_heat(D1, D2, T_opt, ...
parameters, T_amb, time_interval, total_time, heat_pos)

% T: Temperature vector [K] (solid and gas) after
%    time_interval seconds.
% U: Inlet gas velocity [m/s] at timestep n+1.

% D1: 4th-order accurate differentiation matrix of
%     1st-order spatial derivatives using FDM with
%     centered approximations everywhere, except near
%     the boundaries.
% D2: 4th-order accurate differentiation matrix of
%     2nd-order spatial derivatives using FDM with
%     centered approximations everywhere, except near
%     the boundaries.
% T_opt: Temperature vector [K] (solid and gas) at
%        initial time. This comes from the EnKF.
% parameters: model parameters (Nu_i, Nu_o and k_i).
%             These come from the EnKF.
% T_amb: ambient temperature [K] after
%        time_interval seconds.
% time_interval: physical time [s] to run the model for.
% total_time: physical total time [s] to keep track of
%             the heat input to the system so as to
%             reproduce the experiment.
% heat_pos: normalized heater position, x_h/L.

% Solve 1D Advection Diffusion equation with conjugate
% heat transfer and using FD matrices
%
% Heat equation for the solid:
% d(T_s)/dt = eta_1 * d2(T_s)/dx^2
%           - eta_2 * Nuo * T_s
%           + eta_3 * Nui * (T_g - T_s)
%
% Heat equation for the gas:
% d(T_g)/dt = (1+T_g) * (
%                        - U*d(T_g)/dx
%                        + eta_4 * d2(T_g)/dx^2
%                        - eta_5 * Nui * (T_g - T_s)
%                        + qdh
%                       )
%
% Boundary conditions for both solid and gas:
% Homogenous Neumann at x = 0 and +1.

% Input dimensional variables
L_t   = 1.0;     % m          tube length
d_t   = 0.0474;  % m          inner diameter of tube
t_t   = 0.0017;  % m          thickness of tube
g     = 9.81;    % m/s^2      gravitational acceleration
lam_s = 50;      % W/m/K      thermal conductivity of solid
lam_a = 0.026;   % W/m/K      thermal conductivity of
%                             ambient air
c_s   = 500;     % J/kg/K     specific heat capacity of
%                             solid
c_g   = 1000;    % J/kg/K     specific heat capacity of
%                             gas
rho_s = 8000;    % kg/m^3     density of solid
rho_a = 1.2;     % kg/m^3     density of ambient gas
mu    = 1.8e-5;  % kg/m/s     dynamic viscosity of gas

% Set the heat release rate as a function of time to
% reproduce the experiment dynamics, i.e. a
% step-function with jumps every 70 min. Enter total
% heat release rate as the envelope integrates to 1
qhd   = 10 + 10*floor(total_time/60/70);    % Watts

% Assign ambient temperature to T_a
T_a = T_amb;     % K

% Derive more dimensional parameters
pi_i   = pi*d_t;                % m  inner perimeter of solid
pi_o   = pi*(d_t + 2*t_t);      % m  outer perimeter of solid
A_s    = pi*(t_t*d_t + t_t^2); % m^2  cross-section of solid
A_g    = pi*d_t^2/4;            % m^2  cross-section of gas

% Compute dimensionless parameters
eta_1 = lam_s/rho_s/c_s/L_t^1.5/g^0.5;
eta_2 = lam_a/rho_s/c_s*pi_o/A_s/g^0.5/L_t^0.5;
eta_3 = lam_a/rho_s/c_s*pi_i/A_s/g^0.5/L_t^0.5*L_t/d_t;
eta_4 = lam_a/rho_a/c_g/L_t^1.5/g^0.5;
eta_5 = lam_a/rho_a/c_g*pi_i/A_g/g^0.5/L_t^0.5*L_t/d_t;
qdh   = L_t^0.5/g^0.5/T_a/rho_a/A_g/c_g*qhd;

% Set dimensionless parameters
didt = 1.0;      % d_iris/d_tube
Nuo_opt = parameters(1); % Outer Nusselt number
Nui_opt = parameters(2); % Inner Nusselt number
ki_opt = parameters(3);  % Inviscid pressure loss coeff

% Set length, time, and temperature reference scales
L_ref = L_t;
t_ref = (L_t/g)^0.5;
T_ref = T_a;

% Set number of points (minus one) in the domain and
% compute grid parameters
```

```
x = linspace(0,+1,N+1)';
dx = 1/N;
m = dx*ones(N+1,1);

% Boundary correction to correctly compute the
% numerical values of the integrals
m(1) = dx/2; m(N+1) = dx/2;

% Create identity and null matrices
I  = eye(N+1);
Z  = zeros(N+1);

% Set timestep and number of timesteps to march for
dt = 0.05;
NT = round(time_interval/t_ref/dt);

% Set the heat release rate envelope v(x)
% and normalize it so that it integrates to 1
x_h_over_L = heat_pos;
v = exp(-1000*(x - x_h_over_L).^2);
v = v/(m'*v);

% Write the governing equations in matrix form:
% dT/dt = ( A + (T_g+1) * B ) * T

% Create submatrices of A:
% A_ss contains terms affecting d(T_s)/dt
% that depend on T_s
A_ss = eta_1*D2 - eta_2*Nuo_opt*I - eta_3*Nui_opt*I;
% A_gs contains terms affecting d(T_s)/dt
% that depend on T_g
A_gs = eta_3*Nui_opt*I;
% Assemble the A matrix
A = [A_ss , A_gs ; Z , Z];

% Create submatrices of B:
% B_sg contains terms affecting d(T_g)/dt
% that depend on T_s
B_sg = eta_5*Nui_opt*I;
% B_gg0 contains terms affecting d(T_g)/dt
% that depend on T_g, but not on the velocity.
% (Thus, B will be assembled in the loop)
B_gg0 = eta_4*D2  - eta_5*Nui_opt*I;

% Assemble the source term vector
S = [zeros(N+1,1); qdh*v];

% Create the initial state vector in non-dimensional form
T = T_opt/T_ref - 1;


% Define variable to compute U in the first timestep
Told = T;

% March forward in time for NT timesteps using RK4
for nn = 1:NT

    % Work out U from T
    U = sqrt((m'*(T(N+2:2*N+2)./(1+T(N+2:2*N+2))))  ./  ...
             ((1+T(end))*didt.^-4 - 1 + ...
               ki_opt/2*(max(T(N+2:end))+1)));

    % Update the B matrix
    B_gg = B_gg0 - U*D1;
    % Assemble the B matrix
    B = [Z , Z ; B_sg , B_gg];

    % March forward in time with RK4
    Told = T;
    rhsSum = 0;
    RHS = (A + diag(T+1)*B)*T + diag(T+1)*S;
    T = Told + 0.5*dt*RHS;
    rhsSum = RHS;
    RHS = (A + diag(T+1)*B)*T + diag(T+1)*S;
    T = Told + 0.5*dt*RHS;
    rhsSum = rhsSum + 2*RHS;
    RHS = (A + diag(T+1)*B)*T + diag(T+1)*S;
    T = Told + dt*RHS;
    rhsSum = rhsSum + 2*RHS;
    RHS = (A + diag(T+1)*B)*T + diag(T+1)*S;
    rhsSum = rhsSum + RHS;
    T = Told + dt*rhsSum/6;

    % Set the solid boundary condition at x = 0
    T(1) = T(1) - D1(1,:)*T(1:N+1) / D1(1,1);
    % Set the solid boundary condition at x = +1
    T(N+1) = T(N+1) - D1(N+1,:)*T(1:N+1) / D1(N+1,N+1);
    % Set the gas boundary condition at x = 0
    T(N+2) = T(N+2) - D1(1,:)*T(N+2:2*N+2) / D1(1,1);
    % Set the gas boundary condition at x = +1
    T(2*N+2) = T(2*N+2) - D1(N+1,:)*T(N+2:2*N+2) / ...
               D1(N+1,N+1);

end

% Switch to dimensional values
T = T_ref*(1+T);
U = U*sqrt(g*L_t);

end
```

Appendix C

Performance of model 2

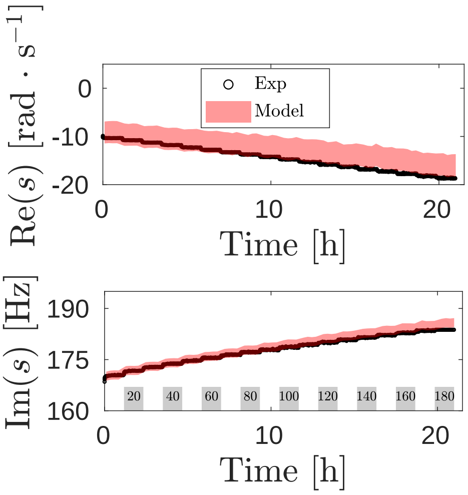

(a) $x_h/L = 0.55$

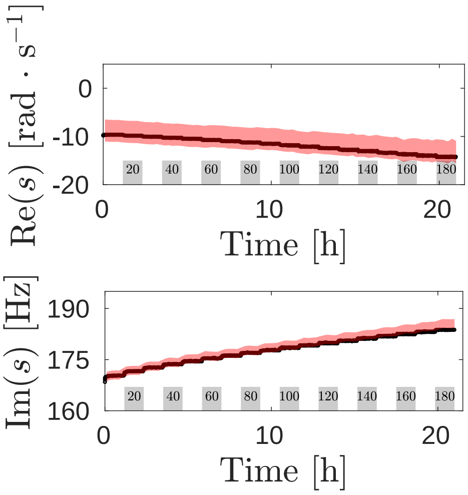

(b) $x_h/L = 0.50$

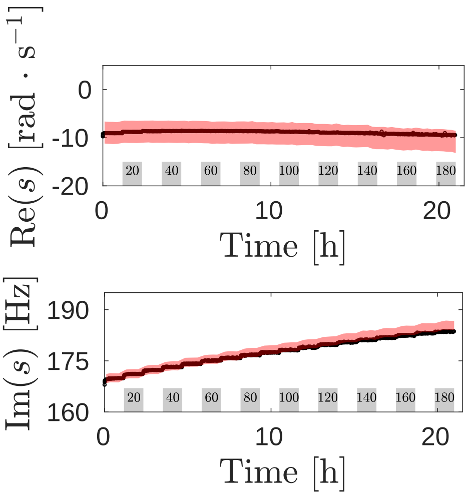

(c) $x_h/L = 0.45$

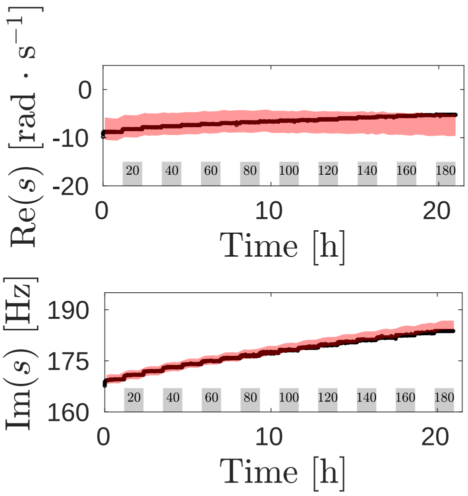

(d) $x_h/L = 0.40$

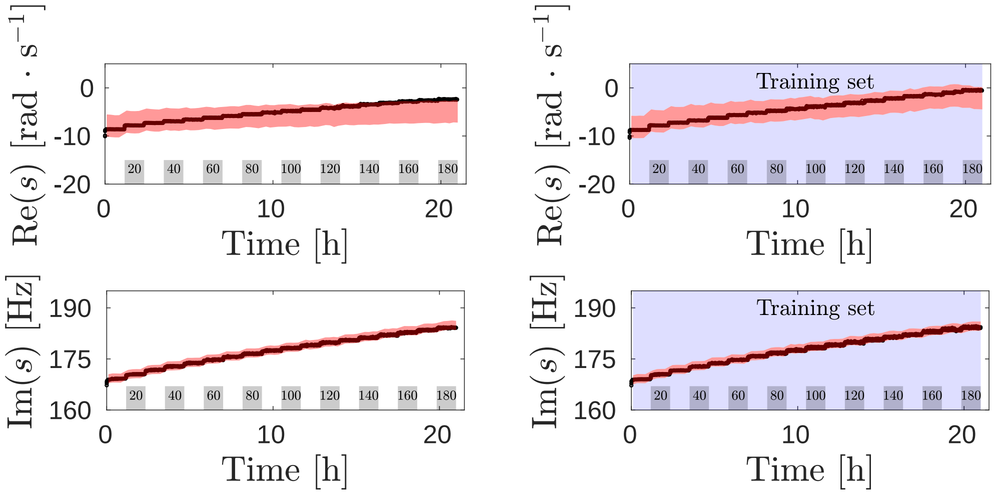

(e) $x_\mathrm{h}/L = 0.35$ (f) $x_\mathrm{h}/L = 0.30$

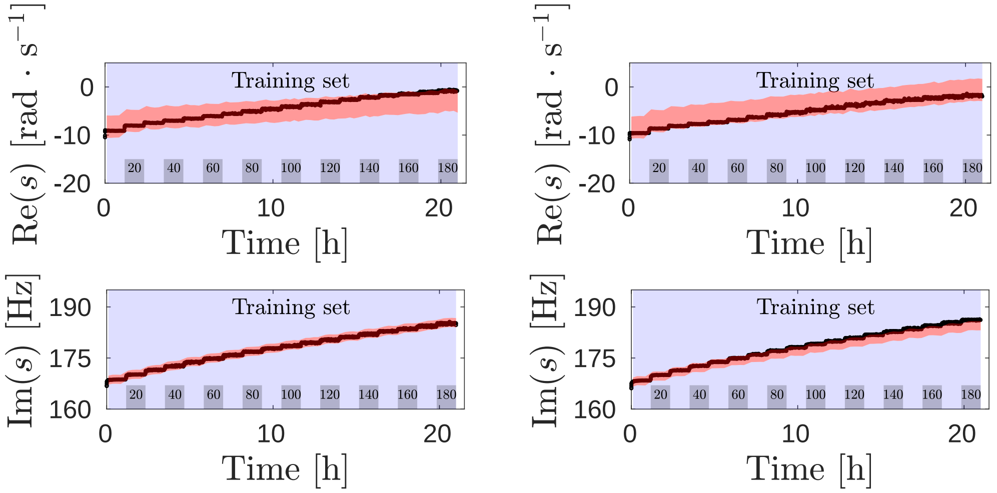

(g) $x_\mathrm{h}/L = 0.25$ (h) $x_\mathrm{h}/L = 0.20$

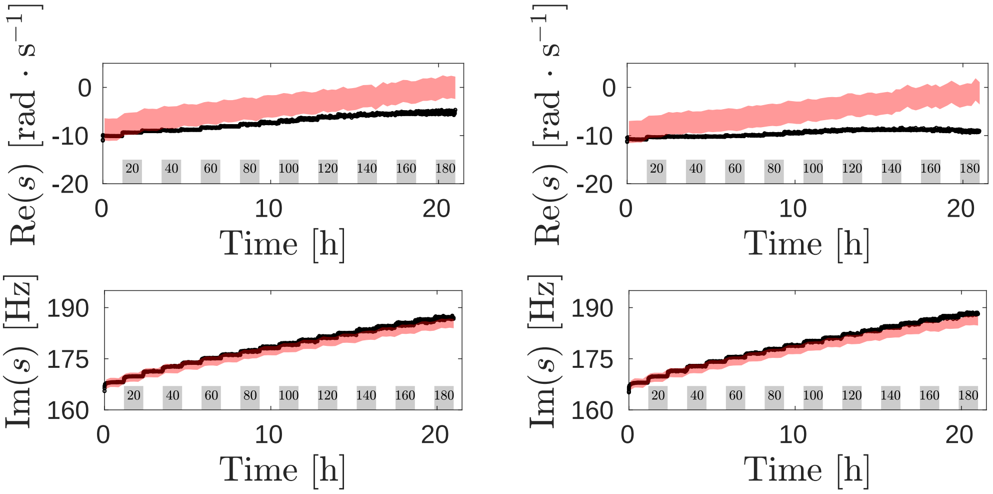

(i) $x_\mathrm{h}/L = 0.15$

(j) $x_\mathrm{h}/L = 0.10$

Fig. C.1 Comparison between experimental data and predictions of **model 2** with 95% confidence intervals, when the training set comprises experimental data at $x_\mathrm{h}/L = [0.20, 0.25, 0.30]$. The heater power is increased every 70 minutes in steps of 10 W (shown by bars at the bottom).

Appendix D

Performance of model 4

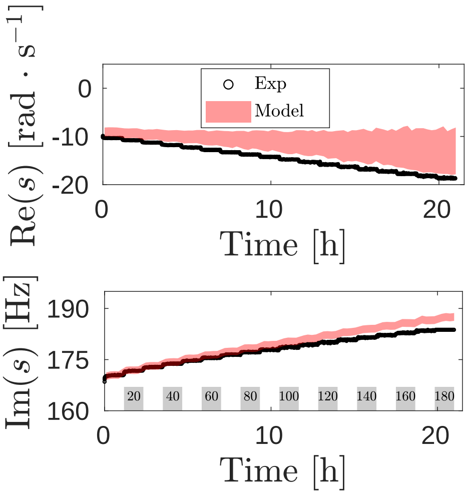

(a) $x_\mathrm{h}/L = 0.55$

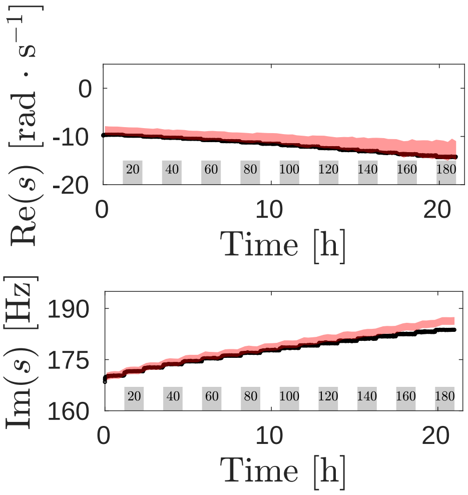

(b) $x_\mathrm{h}/L = 0.50$

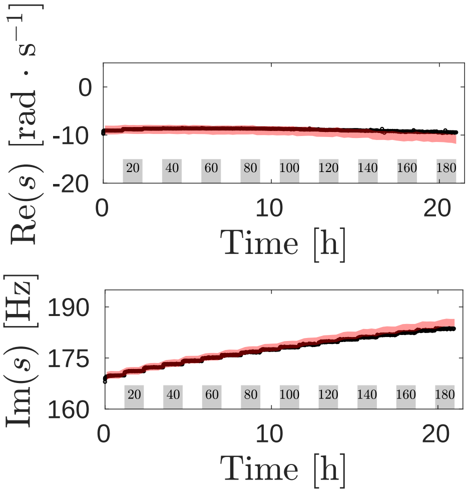

(c) $x_\mathrm{h}/L = 0.45$

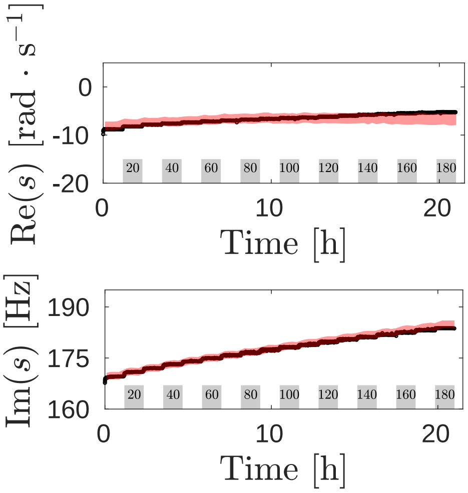

(d) $x_\mathrm{h}/L = 0.40$

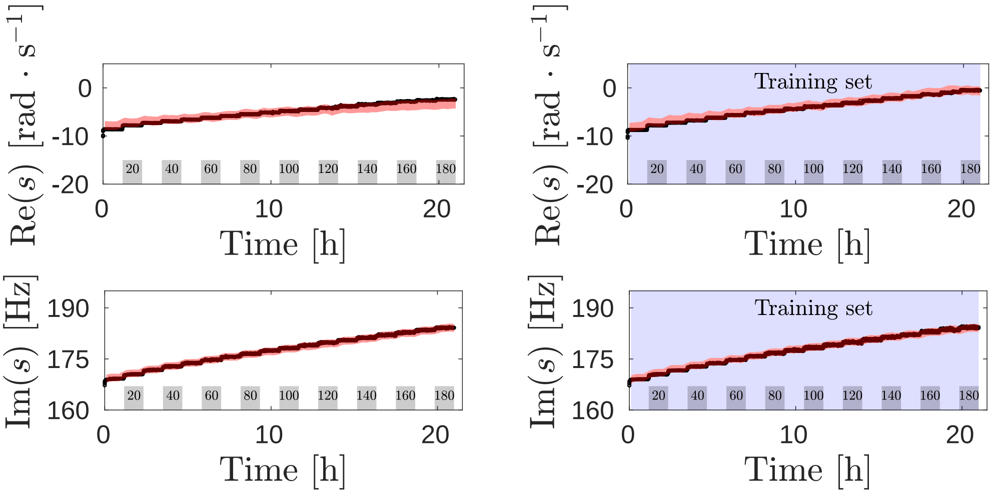

(e) $x_\mathrm{h}/L = 0.35$

(f) $x_\mathrm{h}/L = 0.30$

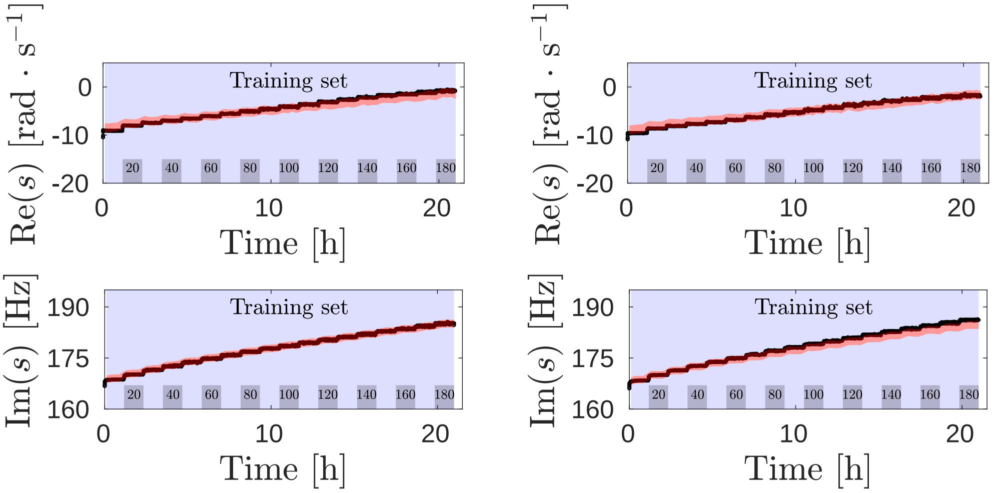

(g) $x_\mathrm{h}/L = 0.25$

(h) $x_\mathrm{h}/L = 0.20$

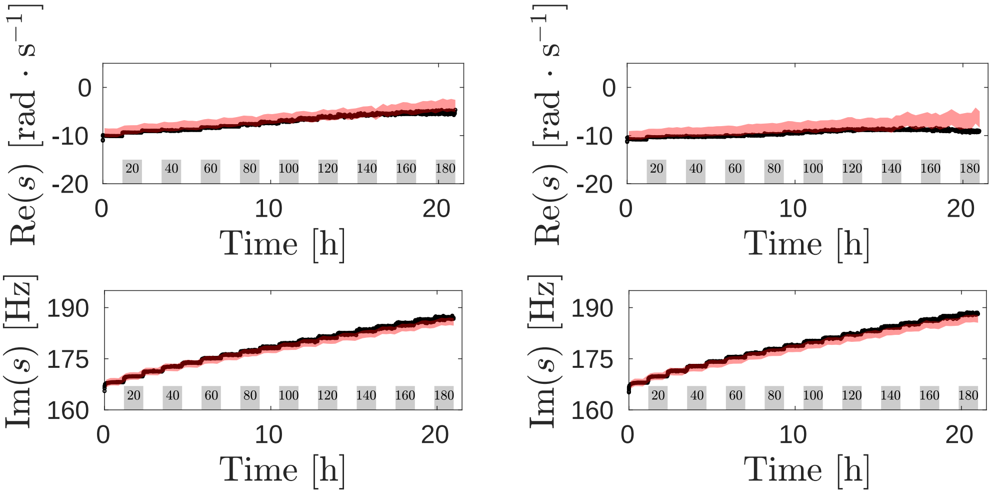

(i) $x_{\mathrm{h}}/L = 0.15$

(j) $x_{\mathrm{h}}/L = 0.10$

Fig. D.1 Comparison between experimental data and predictions of **model 4** with 95% confidence intervals, when the training set comprises experimental data at $x_{\mathrm{h}}/L = [0.20, 0.25, 0.30]$. The heater power is increased every 70 minutes in steps of 10 W (shown by bars at the bottom).